1-1-2011

Single-molecule imaging studies of protein dynamics

Shannon Kian Zareh
Washington University in St. Louis

WASHINGTON UNIVERSITY

Department of Physics

Dissertation Examination Committee:
Yan Mei Wang , Chair
Robert Blankenship
Anders Carlsson
John Clark
Petra Levin
Ralf Wessel

SINGLE-MOLECULE IMAGING STUDIES OF PROTEIN DYNAMICS

by

Shannon Kian G. Zareh

A dissertation presented to the
Graduate School of Arts and Sciences
of Washington University in
partial fulfillment of the
requirements for the degree
of Doctor of Philosophy

December 2011

Saint Louis, Missouri

Abstract

Single-molecule fluorescence imaging is a powerful method for studying biological events. The work of this thesis primarily focuses on single molecule studies of the dynamics of Green Fluorescent Protein (GFP) and other fluorescent-labeled proteins by utilizing Total Internal Reflection Fluorescence (TIRF) microscopy and imaging. The single molecule experiments of this thesis covered three broad topics. First, the adsorption mechanisms of proteins onto hydrophobic and hydrophilic fused silica surfaces were imaged and reversible and irreversible adsorption mechanisms were observed. The second topic covered a new technique for measuring the diffusion coefficient of Brownian diffusing proteins, in particular GFP, in solution via a single image. The corresponding experiments showed a relationship between the intensity profile width and the diffusion coefficient of the diffusing molecules. The third topic covered an *in vivo* experiment involving imaging and quantifying prokaryotic cell metabolism protein dynamics inside the *Bacillus subtilis* bacteria, in which a helical diffusion pattern for the protein was observed. These topics are presented in the chronological order of the experiments conducted.

Acknowledgements

I would like to start with thanking the Physics Department Admissions Committee, specially Prof. Schilling, for believing in my ability and giving me the opportunity to be a part of the Physics Department of Washington University in St. Louis. The academic environment in this department opened a door to an infinite horizon to me. My education in the intellectual and friendly environment of Wash. U. has made me a different and better person.

Also, I would like to acknowledge Professor Yan Mei Wang for her leadership of my research. Being the first student of Yan Mei, I got the opportunity to set up an experimental research lab next to her. During the four years that I spent in our lab, through all the ups and downs, hardships and easy times I learned how to be a stronger person, how to work harder and harder every day, and how to approach life with a positive mentality. Also hereby, I would like to acknowledge my dissertation committee members Prof. Clark, Prof. Carlsson, Prof. Wessel, Prof. Levin and Prof. Blankenship for providing feedback and encouragement on the work of my dissertation.

Furthermore, I am pleased to acknowledge my research group member and col-

league Michael DeSantis for always being willing to be a part of an engaging and meaningful discussion about our research, specially regarding the work that is presented in Chapter 4 of this thesis. I certainly learned a lot from our conversations. Also, I would to acknowledge current and former group members jonathan Kessler, Anthony Kovacs and Shawn DeCenzo.

This is a great opportunity to express my respect to Professor Mark Alford for his mentoring, guidance and support throughout both difficult and easy times of my time in grad school, specially during the last couple years. Also, The lunch time conversations with Professor Alford, Professor Buckley, and Professor Leopold will always remain in the top of the list of my memorable things of grad school.

It is necessary to acknowledge the helpful conversations done with Professor Petra Levin and her senior graduate student Jenny Chien regarding the work described in Chapter 5 of this dissertation. Especially, I would like to acknowledge Jenny for patiently teaching me all the basics of growing a bacteria cell culture.

I would like to take the opportunity to thank Julia Hamilton and Sarah Hedley in the Physics Department office, as well as Tony and Todd Hardt in the Physics Department machine shop for providing the necessary guidance assistance. Working around such helpful, joyous, caring and valuable personnel made the quality of my grad school life so much better and more enjoyable. I would also like to thank Mary and Rita in the Services department for their lovely smiles and providing help.

It is very important for me to mention that I owe most of my academic endeavors and achievements to every individual teacher and professor that I have ever had

throughout my life at any stage of my education. I would like to thank all of them for leading me towards where I am heading now. Also, I would like to thank my wonderful friends who were always there for me and made this journey in grad school and St. Louis such an enjoyable one. Each, in their own special way, has showed love, care and support whenever I needed it.

Last but not least, I would like to thank my family members. A sincere thanks goes to my supportive and caring sisters; to Maryam, who has shown me a new color of life every time I have been lost, and to Niki for being so supportive, helpful and caring. Also, I would like to thank my brother Eric and his wife Susan for their support, guidance, generosity and love throughout all these years. I would also like to thank my sister Rebecca and her husband Eric, as well as my brother Christian for their love and support.

My Aunt Farahnaz has always played a special and unique role in my life, and here I would like to thanks her and say that I love her.

This dissertation is dedicated to my parents, Akram and Massoud. They are the true meaning of love, support and inspiration for me and I would like to thank them for all the love and encouragement they have shed on my life and say that I love them. In addition, I would like to dedicate this to the memory of my grandparents Aghabeigom Moosavi Hamedani, Ali Izadyar, Azemat Zarghami and Seifollah Zareh.

Contents

List of Figures

List of Tables

Chapter 1

Preface

The chapters in this thesis present the work that I have done in my PhD from Spring 2007 until Summer 2011. During my PhD research I worked on multiple projects, three of which were completed and are presented in a chronological order of their completion here in chapters 3, 4 and 5. It is worthy to mention that I spent most of my time on the project presented in Chapter 4 (single-image diffusion coefficient measurement), and spent the entire last year of graduate school working on the research topic of Chapter 5 (protein dynamics inside a cell).

Due to being the first student to join Prof. Wang's research group, I spend a lot of time next to Prof. Wang helping with setting up the lab, all of which is described and documented in the Appendices chapter of this thesis.

Chapter 2

Introduction and Background

2.1 Preface

This chapter is written primarily for explaining the fundamentals of single molecule studies and the physics of our TIRF imaging technique, image analysis method, fitting functions and Brownian diffusion. The concepts explained in here are used in the future chapters.

2.2 Introduction to Single Molecule Method

Single molecule fluorescence detection is a powerful tool in probing biological events without time and population averaging. Since its emergence 20 years ago, single molecule fluorescence imaging has revolutionized our knowledge of biological processes, and previously unobtainable elementary molecular processes have become experimentally observable and quantifiable.

Most physical, chemical and biophysical experiments measure the average behavior of a huge number of molecules, from millions to Avogadro's number (6.02×10^{23}). To explore what happens when ensemble averaging is removed, single molecule experiments are performed. These single molecule experiments allow scientists to detect and probe the properties of individual molecules ($N = 1$). In this way scientists can truly explore the local behavior of the molecule in its immediate surrounding such as the dynamics of a single protein inside a living bacterial cell. Two broad categories of single molecule experimental methods are (1) fluorescence imaging and spectroscopy, including total internal reflection fluorescence (TIRF) microscopy [1] and fluorescence correlation spectroscopy (FCS)[2, 3, 4] and (2) force-based manipulation and detection, such as optical tweezers, magnetic tweezers, and atomic force microscopy (AFM) [5].

Single molecule nanoscience is an interesting field because it allows for exploring the hidden heterogeneity of complex systems. The heterogeneity of complex systems can be produced by different local environmental conditions or different conforma-

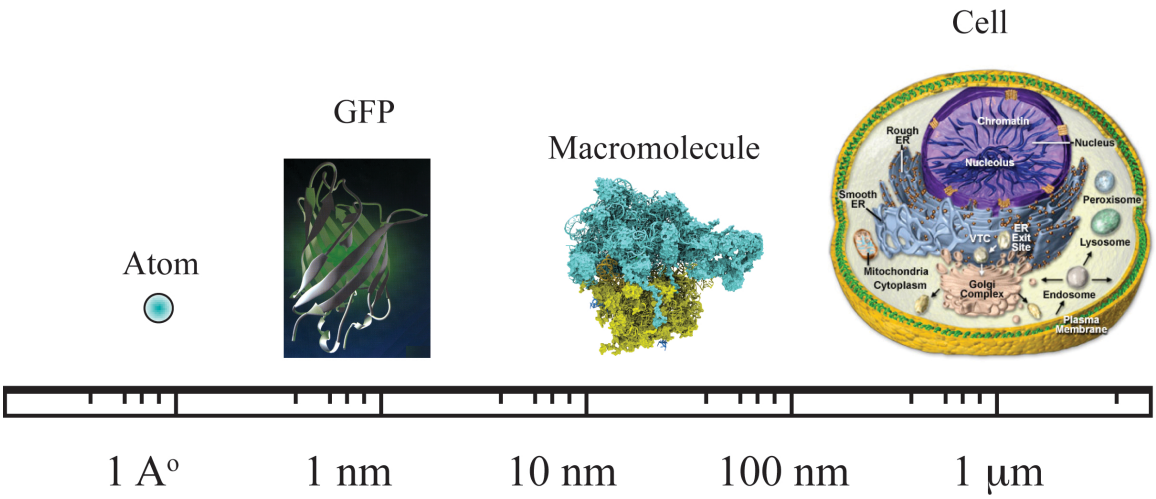

Figure 2.1: A logarithmic scale of the dimensions of atoms, proteins and cells. Cellular processes occur on a broad range of scales, and there is a hierarchy of complexity from simple molecules to the complex cellular environment. A simple protein like GFP is about 5 nm and a cell is in the micrometer range as shown in the figure. Single molecule techniques allow exploring biological events in the nm scale range via *in vitro* experiments or inside the cells via *in vivo* experiments.

tional states. Single molecule studies allow scientists to explore these hidden heterogeneities because they can measure the distribution of behavior by recording the properties of each individual member of the ensemble, one by one.

Valuable information about the behavior of a fluorescent emitter can be gained from studying the time-dependent and time-independent changes of the intensity profile of such emitter. The intensity profile is the pattern of the collected photons on the pixelated chip of the microscope's CCD camera. This information includes but is not limited to the following: localization of the molecule beyond the diffraction limit [6], the distance measurement between two molecules in the 5-9 nm scale by Förster Resonance Energy Transfer (FRET) technique [7], diffusion coefficient, molecular weight, polarization [8], and kinetic parameters.

2.3 Brief History of Single Molecule Studies

Single molecule study of biological processes is a relatively new field, less than 20 years old, and has been growing very rapidly ever since its emergence. The very first single molecule was detected in a solid at liquid helium temperatures by Moerner and Kador in 1989 [9], and followed up by the detection of a single fluorescent molecule by Orrit and Bernard in 1990 [10]. Single molecule detection was later extended to detecting single fluorescent molecules at room temperature by Betzig and Chichester in 1993 [11] who basically extended these studies to biological applications. In 1995 the first detection of single fluorescent molecule in aquatic conditions was achieved by applying total internal reflection fluorescence (TIRF) microscopy by Funatasu and Harada [1]. In 2000 the first single molecule was imaged inside a living cell [12]. According to the statistics reported by Moerner in a publication in 2007 the field of single molecule study has been growing exponentially with a doubling time of 2.2 years, and if the trend continues in 25 years every paper in biomedical sciences will include single-molecule data [13].

2.4 Background

2.4.1 Fluorescence Microscopy and Imaging

The fluorescence microscopy technique [14] has become an important tool in biology and biomedical sciences. Fluorescence microscopy utilizes an optical microscope

and uses fluorescent molecules like dyes or autofluorescent molecules for probing the events in a biological environment. Optical fluorescent microcopy and imaging is an important probe for cell biology since light can noninvasively probe the cell with minimal perturbation to the specimen, thus enabling the observation of the dynamics inside the cell.

The application of different fluorophores has made it possible to study molecules with a high degree of specificity among non-fluorescing molecules and environment. By using multiple fluorescence labeling, different probes can identify several target molecules simultaneously, and reveal the dynamics and kinetics of the interactions between them. Although the fluorescence microscope cannot provide spatial resolution below the diffraction limit, the localization of fluorescing molecules below the diffraction limits is readily achieved [6] and will be discussed in the later sections.

A few of the popular advanced fluorescence microscopy and spectroscopy methods include total internal reflection fluorescence (TIRF) microscopy [15], epifluorescence microscopy (or wide-field microscopy), and confocal microscopy [16]. The experiments in this thesis have been mostly done by TIRF microscopy, and in some cases epifluorescence microscopy. A few of the common experimental fluorescence microscopy techniques include fluorescence correlation spectroscopy (FCS), fluorescence recovery after photobleaching (FRAP), and fluorescence resonance energy transfer (FRET) [7, 17].

2.4.2 TIRF Microscopy

Total Internal Reflection Fluorescent (TIRF) microscopy [15] is a method that enables the minimization of the illumination area by selectively exciting fluorophores that are very near the imaging surface. When applied to biological systems, TIRF microscopy allows selective visualization of molecules and cells closest to the interface. TIRF microscopy can be used qualitatively to observe the motion of these molecules or cells, or can be used quantitatively to measure the position of the point spread function of the single molecules, concentration of the molecules, photon emission intensity, fluorescence time trace, and dynamics of these molecules or cells. TIRF microscopy was first developed by Dr. Axelrod in the early 1980's at University of Michigan, and has been widely used in the field of fluorescent microscopy ever since.

The physics of the refraction of an incident beam at an interface is described as follows. A beam of light that is incident at the interface of two media with indices of refraction n_1 and n_2 at an incident angle of θ_1 and refracted angle of θ_2 (both measured from the normal to the surface) follows Snell's law as follows:

$$n_1 sin(\theta_1) = n_2 sin(\theta_2), \tag{2.1}$$

Total internal reflection occurs when a beam of light is incident at the interface of two media with different indices of refraction, traveling from the medium with higher index of refraction n_1 to the medium with lower index of refraction n_2 ($n_1 > n_2$) over a certain range of angles. This range of angles is any angle equal or greater than the

critical angle θ_c. The critical angle θ_c is the angle at which the refracted light travels completely parallel to the interface, and above the critical angle all of the light is totally internally reflected. The critical angle θ_c is different for different interfaces, and can be determined by

$$\theta_c = arcsin(n_2/n_1) \tag{2.2}$$

When total internal reflection happens an exponentially decaying wave, called the *evanescent wave*, gets created in the medium with the lower index of refraction. The evanescent wave is an electromagnetic field with an exponentially decaying intensity, $I(z)$, as shown in Figure 2.3. The intensity of the evanescent wave, $I(z)$, can be represented as

$$I(z) = I(0)e^{-z/d}, \tag{2.3}$$

The evanescent wave penetrates a couple of hundred nanometers into the medium with n_2. This penetration depth of the evanescent wave, d, is dependent on the incident angle θ, where $\theta > \theta_c$. The penetration depth d of the evanescent wave is dependent upon the wavelength of the incident light, the incidence angle, and the refractive indices of the media at the interface

$$d = \frac{\lambda_0}{4\pi\sqrt{{n_2}^2 sin^2(\theta) - {n_1}^2}}, \tag{2.4}$$

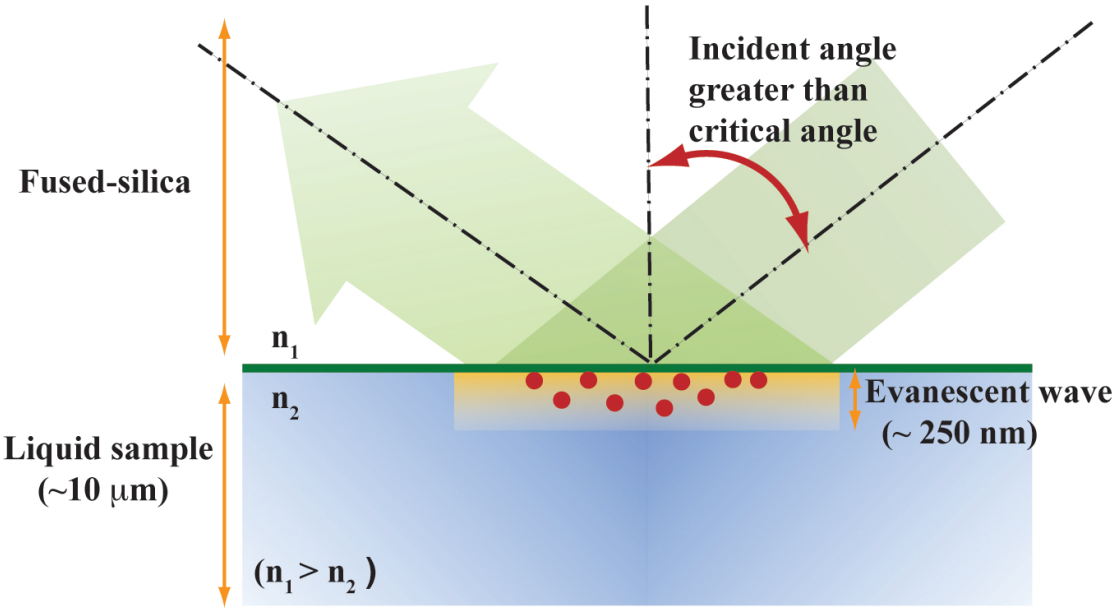

Figure 2.2: The schematics of the creation of evanescent wave at the interface of fused silica and water. When the illumination beam is incident on the interface at an angle above the critical angle all of the light is reflected and an exponentially decaying wave gets created and penetrates into the medium with lower refractive index. The penetration depth of the evanescent wave is in the order of a couple hundred nanometers, which enables minimization of the illumination depth resulting in single molecule imaging. The depth of a typical liquid sample containing the molecules of interest is about 10 micrometers.

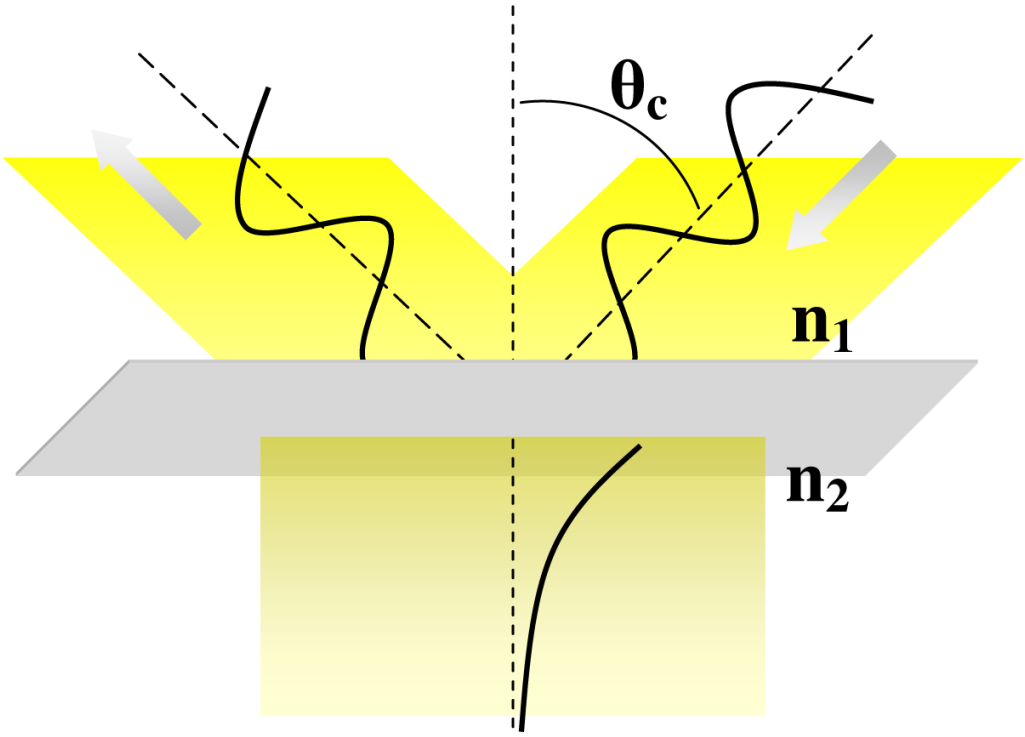

Figure 2.3: Schematics of the incident sinusoidal wave, and the exponentially decaying evanescent wave at the interface

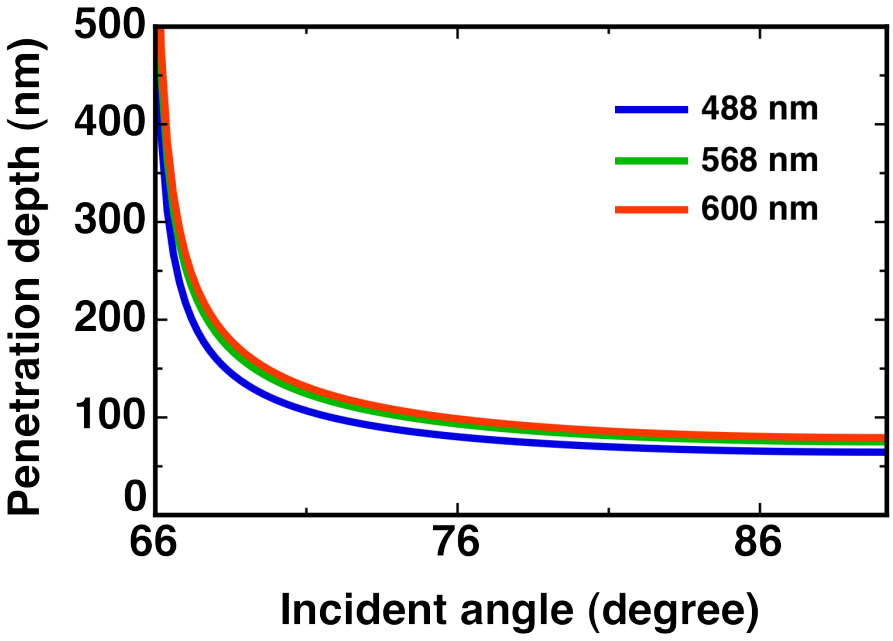

Figure 2.4: Penetration depth of the evanescent wave is a function of the incident angle. The critical angle is close to 66 degrees for the three wavelengths shown here. The penetration depth decreases dramatically from 500 nm to close to 100 nm.

where λ_0 is the wavelength of the incident light in vacuum. Figure 2.4 shows the dependence of penetration depth to the incident light angle for the 488 nm, 562 nm and 600 nm wavelengths.

In our lab's TIRF microscopy practice, the total internal reflection interface consists of fused silica and water (buffer) with $n = 1.46$ and $n = 1.33$ respectively. In the preparation of our lab samples, the deposition of a droplet of the size of 5 μL buffer ($n_2 = 1.33$) containing the protein or cell of interest on the surface of fused silica slide ($n_1 = 1.46$) which gets sealed with a glass slide ($n_3 = 1.53$) results in the creation of a volume with the height of 10μL (check the Methods and Protocols chapter in the Appendices section for the details). However, by utilizing TIRF microscopy we only illuminate $\sim 200\ nm$ of the 10 μL depth. A 5 μL droplet of $1nM$ concentration

contains 3×10^9 molecules. With TIRF microscopy we illuminate only 250 of these molecules. The total internal reflection phenomenon helps minimize the illumination depth from a few microns (in our case 10 μm) to a few hundred nanometers, which in return enables single molecule studies with lower background fluorescence and noise.

2.4.3 Diffraction Limited Image, Point Spread Function (PSF) and Rayleigh Criterion

In optical microscopy, when the light emitted from an object passes through the back aperture of the microscope objective, it creates a diffraction limited image and the object is treated as a point-like source. The diffraction limited image is mathematically represented by the Airy function as following

$$PSF(r) = (2\frac{J_1(ar)}{r})^2 \tag{2.5}$$

where

$$a = \frac{2\pi NA}{\lambda} \tag{2.6}$$

$J_1(r)$ is the Bessel function of the first kind [18], and r is the distance from the origin of the PSF. The Airy function is the Fraunhofer diffraction pattern of a circular aperture, and is a point spread function (PSF). The PSF describes the response of an imaging system to a point-like source. In fluorescence microscopy a fluorescent protein like green fluorescent protein (GFP) [19] or a quantum dot acts like a point-like

source whose image is a diffraction limited PSF as shown in Figure 2.5. The degree of the spread of the point spread function is related to factors like the wavelength of excitation light λ and the numerical aperture of the microscope, NA.

The resolving power of an optical system can be limited by its imaging elements, such as its lens. In the case of microscopy this limit would be imposed by the microscope objective in which the lens is situated. The resolution limit of a microscope comes from the Abbe diffraction limit, and is defined as the shortest distance between two points on a specimen that can still be distinguished by the microscope system as two separate objects. This distance d is where the first diffraction minimum of the image of one point source coincides with the maximum of another point source. This limitation is called the Abbe diffraction limit, and the microscopy is called diffraction limited microscopy. The resolution is described by the Rayleigh criterion as

$$d = \frac{0.61\lambda}{nsin\theta}, \tag{2.7}$$

where d is the resolvable feature size, λ is the wavelength of light, n is the refractive index of the media in the object space (between the coverslip glass and the objective front lens) and θ is one-half the angular aperture. Figure 2.7 attempts to illustrate the Rayleigh criterion. The angular aperture, which varies with the objective focal length, is the maximum angle of image-forming light rays emanating from the specimen that the objective front lens can capture when the specimen is in focus. As the objective focal length decreases, the maximum angle between the specimen and the outside

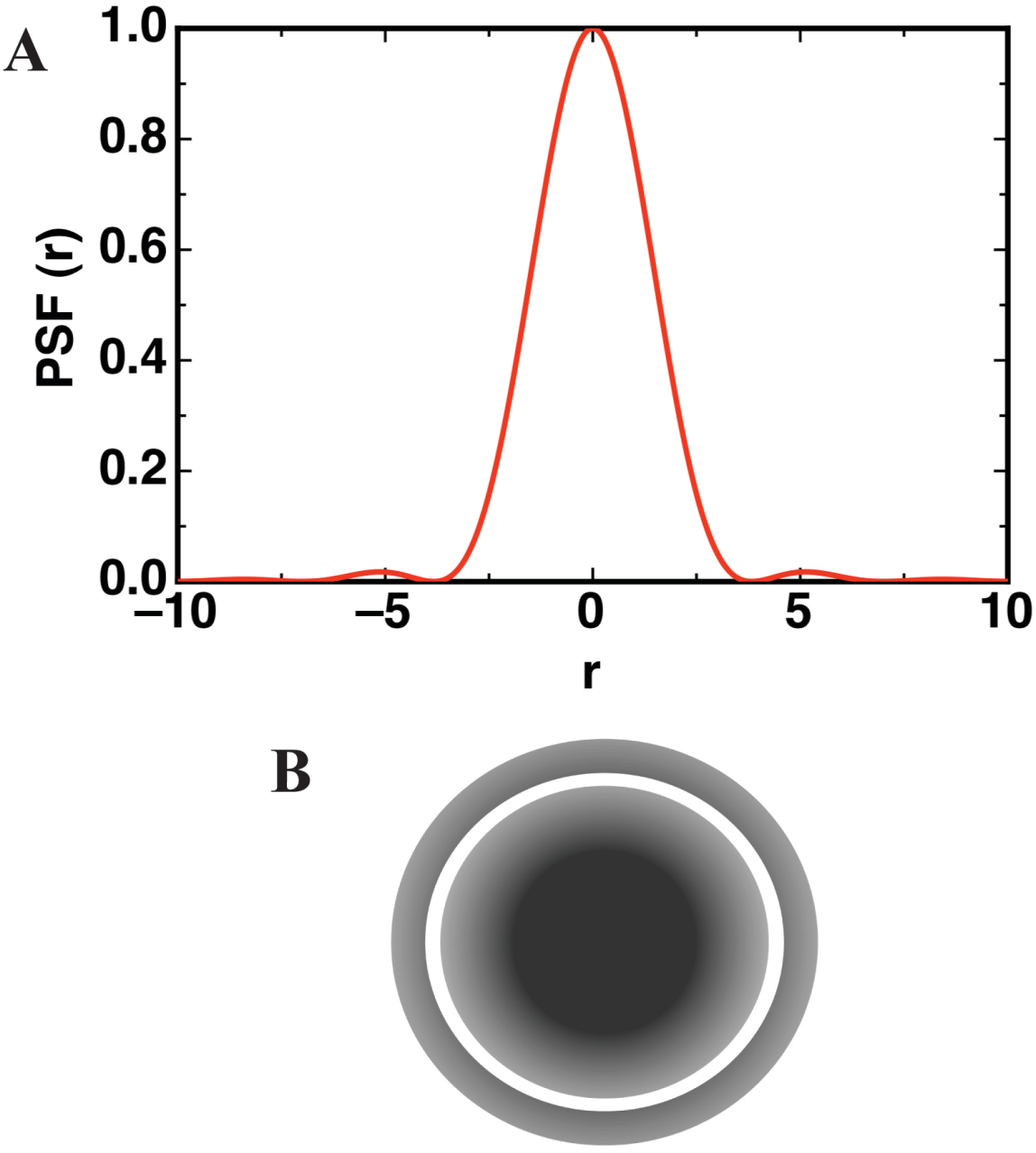

Figure 2.5: The 2 dimensional intensity profile of an Airy pattern is shown in a vertical cross section in (A), and the horizontal cross section is shown in (B). Both figures show an Airy pattern consists of a bright middle disk and dimmer outer rings. The middle disk can be approximated by a Gaussian.

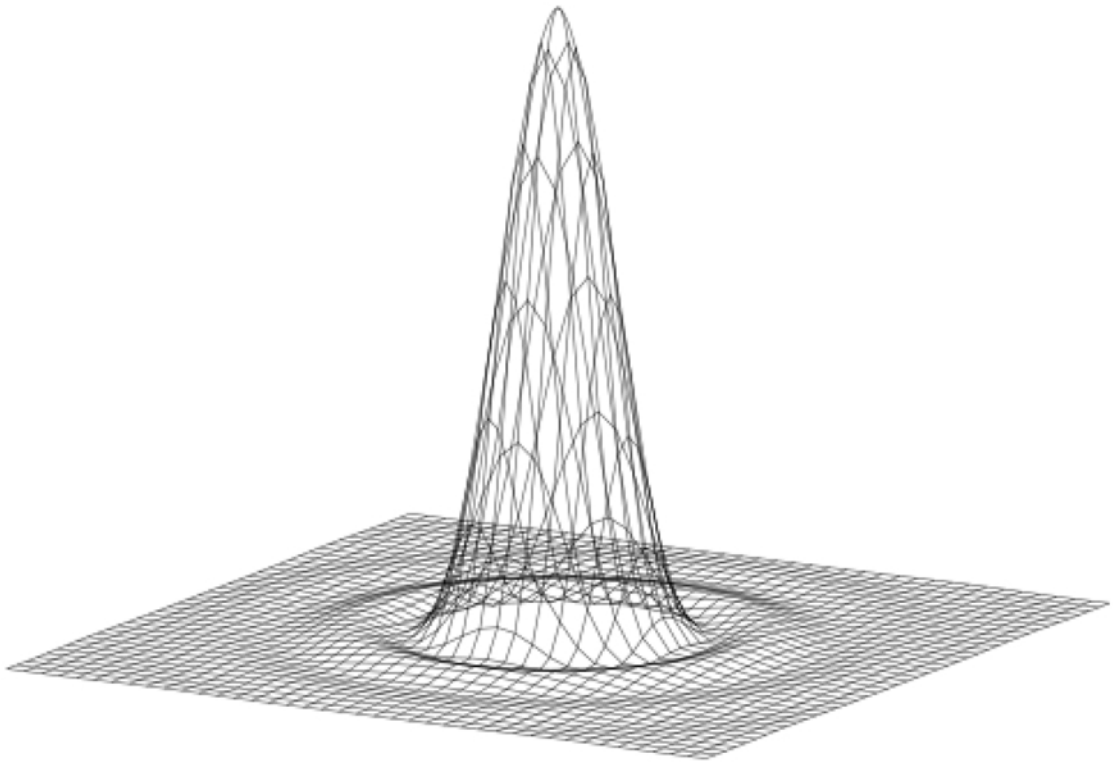

Figure 2.6: The 3D intensity profile of an Airy disk. The intensity profile of a molecule on an EMCCD camera is a point spread function (PSF) since the molecule acts like a point like source as viewed by the back aperture of the camera. A point spread function has an Airy pattern (Image reference: Wikipedia).

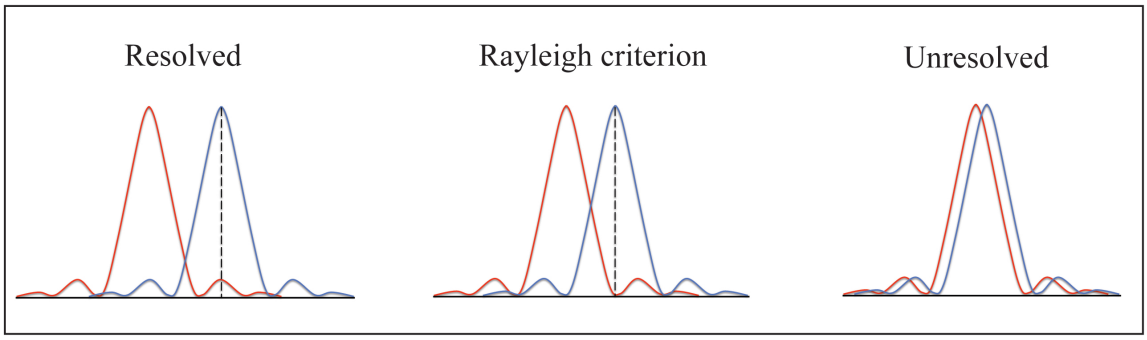

Figure 2.7: This figure shows the Rayleigh criterion for two wave patterns in three different situations. Two adjacent points are just resolved when the centers of thir Airy patterns are separated by a minimum distance equal to the radius of the central disk in the Airy pattern. This distance d is where the first diffraction minimum of the image of one point source coincides with the maximum of another point source. Anything less than this distance is unresolved.

diameter of the objective front lens increases. The value of index of refraction n varies between 1.0 for air and 1.52 for a majority of immersion oils utilized in optical microscopy. The Rayleigh criterion formula can also be expressed in terms of the objective numerical aperture NA. The NA of the lens measures its ability to collect light, and is given by

$$NA = nsin\theta \tag{2.8}$$

which gives

$$d = \frac{0.61\lambda}{NA}, \tag{2.9}$$

In our lab, with $NA = 1.49$ and for the excitation wavelength of 488 nm the resolution limit is ~ 200 nm.

2.4.4 Gaussian Approximation to the PSF

The image of the fluorescent molecule as viewed by the microscope's camera is a PSF and has an Airy disk pattern. The intensity profile of an Airy disk is composed of a very bright center and a few outer rings. Since the outer rings are much dimmer compared to the central disk and the central disk has the same profile as a Gaussian function, the intensity profile of an Airy disk can be very well approximated by a Gaussian profile. In other words, the peak of the PSF and therefore the intensity distribution of a point-like source can be fit to a 2D-Gaussian function [20, 18]. This is desirable because it enables a simple mathematical approach to addressing and quantifying the intensity pattern of a PSF. Thus, directly fitting the Gaussian equation to images of particles has become a common method of particle tracking [21]. The following represents a Gaussian function that could be fit to the intensity profile of a molecule on the CCD camera of a fluorescence imaging system

$$f(x,y) = f_0 \exp\left[-\frac{(x-x_0)^2}{2s_x^2} - \frac{(y-y_0)^2}{2s_y^2}\right] + \langle b \rangle, \tag{2.10}$$

In the above equation, f_0 is the prefactor, s_x and s_y are standard deviation values in the x and y directions respectively, x_0 and y_0 are the centroid location of the molecule, and $\langle b \rangle$ is the mean background offset. The goal is to determine the center or mean value of this Gaussian distribution, precision to the mean, standard deviation of the distribution, and the precision of the standard deviation. The mean measurement enables the lateral location determination of the molecule in x and y directions,

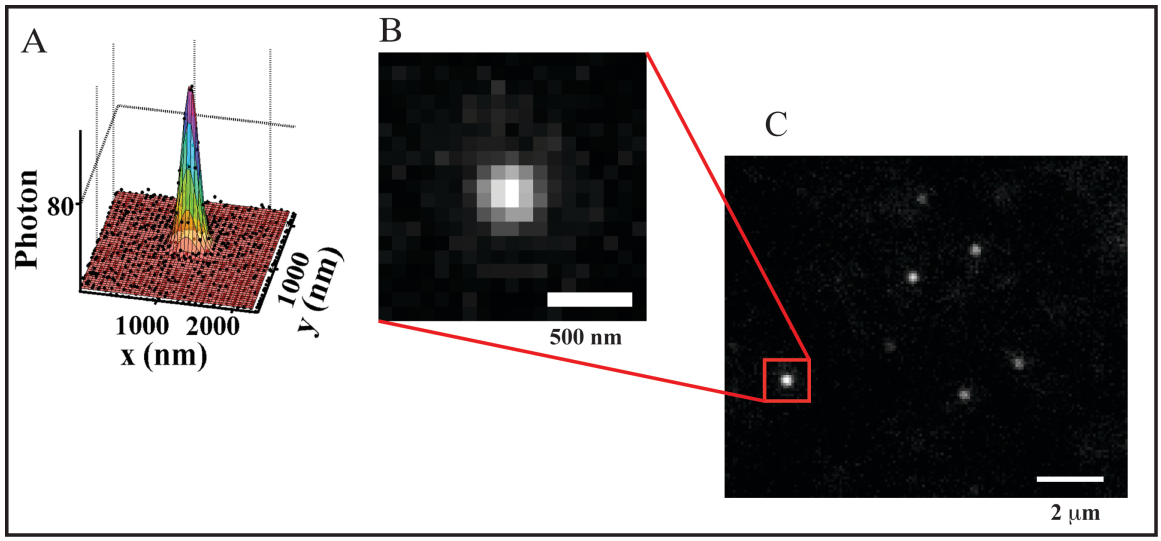

Figure 2.8: (C) Shows the EMCCD camera image of 7 immobile GFPs on the fused-silica surface. The zoomed-in image of one of the molecules is shown in (B). The molecule's image on the EMCCD camera is a PSF. The Gaussian fit to its intensity profile is shown in (A)

and the standard deviation measurements gives information about the axial position of an immobile molecule. Also, for the case of a diffusing molecule the standard deviation value enables diffusion coefficient calculations of the molecule. The diffusion coefficient measurement of a single 3d diffusing molecule from the standard deviation of its intensity profile is described thoroughly in chapter 3.

2.4.5 The Precision of Single Molecule Localization Measurements

A single molecule can be viewed as a probe of its immediate local nano-environment on the scale on the order of the molecular size. Calculation of the centroid of the 2D-Gaussian intensity profile of an individual fluorescent molecule allows for the

localization and tracking of the molecule to a precision about an order of magnitude greater than the microscope resolution. Thompson *et al.* have derived a localization precision equation that scales as inverse square root of the number of photons ($\frac{1}{N}$) in the spot for the shot noise limited case, and as the inverse of the number of photons for the background noise limited case [22].

Any object smaller than the resolution dimension of an optical microscope appears to be a diffraction limited spot. An example is shown in Figure 2.8. Although the details of this diffraction limited spot are not resolvable and the resolution is limited to the Rayleigh criterion of $d = \frac{0.61\lambda}{NA}$, the location center of this diffraction limited spot can be determined by the equation developed by Thompson *et al* in 2002 [22]. This means that the location of the molecule can be determined to a much greater precision than the diffraction limit, enabling going beyond the diffraction limit. The relation between the precision in the localization measurement and the number of collected photons N, the pixel size of the imaging detector a, the standard deviation of the background b (which includes background fluorescence noise and detector noise), and the width of the distribution (standard deviation, s_i, in direction i) is

$$< (\Delta x)^2 >= \frac{s_i^2 + a^2/12}{N} + \frac{8\pi s_i^4 b^2}{a^2 N^2} \tag{2.11}$$

As stated above, this precision is highly dependent on the total number of photons detected from the spot. Given that it is possible to detect many more than 10^4 photons from a single fluorophore before it bleaches, single molecule localization to

nearly 1 nm precision has already been demonstrated. Having utilized this formula for a PSF generated from $N = 14,200$ photons, $a = 86\ nm$, $b = 11$, $s_y = 122\ nm$, $s_x = 125\ nm$, Yildiz *et al.* showed 1.5 nm precision in localization measurements of Myosin V walking on actin [6]. The Gaussian fit to a molecule with photon $N = 100$ is shown in Figure 2.9.

Furthermore, our group has recently improved this equation to the following [23]

$$< (\Delta x)^2 >= \frac{2(s_{0x}^2 + a^2/12)}{N} + \frac{8\pi(s_{0x}^2 + a^2/12)^{3/2}(s_{0y}^2 + a^2/12)^{1/2}(\sigma_b^2 + < b >^2)}{a^2 N^2} \tag{2.12}$$

2.4.6 Signal to Noise Ratio in Single Molecule Imaging

The two important categories of noise are the shot noise of the photons in the spot, and the background noise. The signal-to-noise ratio (SNR) depends on both of these sources following the formula

$$SNR = \frac{I_0}{\sqrt{I_0 + \sigma_b^2}} \tag{2.13}$$

where I_0 represents the shot noise, and σ_b represents the background variance. The shot noise is a Poisson process where the noise variance increases as $\sqrt{N}$ [18]. The shot noise is generated from the intensifiers in the CCD cameras. Some contributors to the background noise are the CCD readout noise and the dark noise. For a dominating

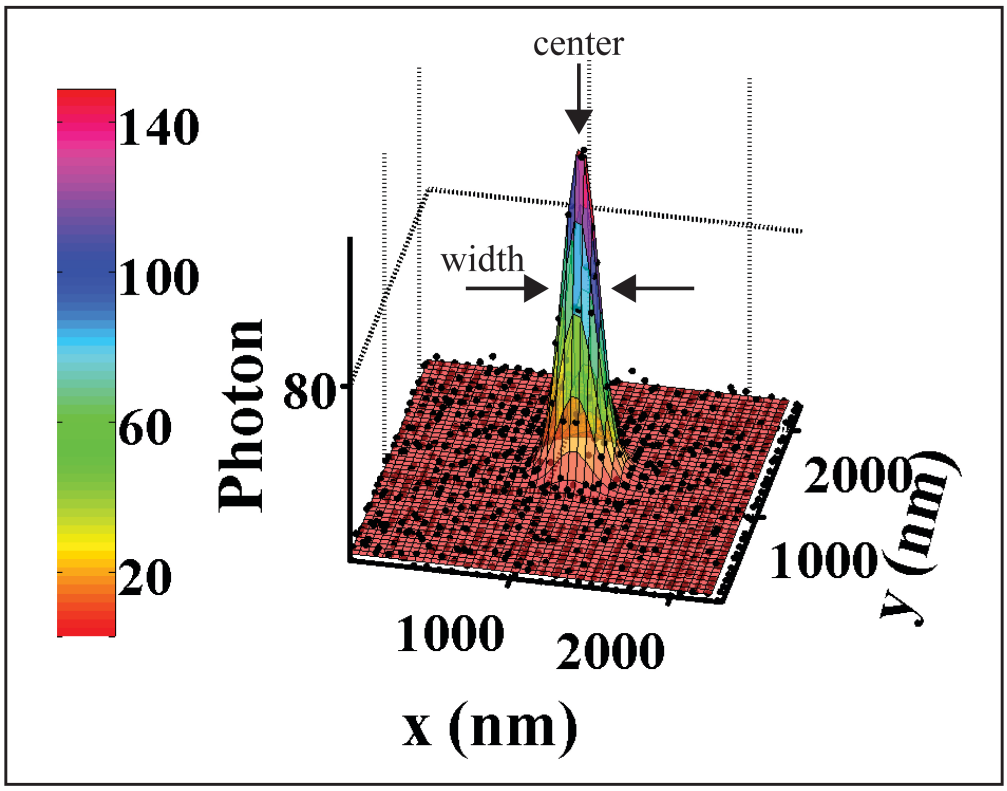

Figure 2.9: A molecule's intensity profile can be fit to a Gaussian function. The mean of the Gaussian gives information about the lateral location of the molecule in a 2D plane. The precision to the mean is dependent on the number o the collected photons from the molecule by $\frac{1}{\sqrt{N}}$. The standard deviation of the Gaussian gives information about the axial location of the molecule.

background noise the precision of localization measurement scales as *1/N*. This means that at low excitation light intensities it becomes more important to minimize the background noise.

The most important technical advances in the detection of single molecules has been regarding enhancing the SNR. There have been major technical advances in enabling the single molecule detection. As described in the previous sections, the field has progressed from the detection of single fluorophores in cryogenic temperatures to identifying multiple fluorophores attached to a biological system in a solution at room temperature [24].

Some advances in lowering the SNR include: (a) the background noise has been effectively reduced by constraining the illumination to a shallow depth (by TIRF microscopy) or small volume (e.g. by confocal microscopy), (b) the shot noise has become stronger by using brighter and more photostable fluorophores by carefully choosing solution conditions like PH, (c) cooled charge-coupled devices (CCDs) have achieved high quantum yield and zero-dead time together with sub-millisecond time resolution, (d) advances in objective lenses (high NA, high magnification, low aberration) and laser technologies (high-stability, high-mode lasers with various wavelengths) have been achieved.

Fluorophores

In single molecule fluorescence spectroscopy and microscopy all the information is gained from the fluorescence quality of the fluorophore. This means that the flu-

orescent molecule is the storyteller. When attached to a biological molecule, the fluorescent molecule gives information about the biological molecule in a stream of emitted photons.

Fluorescence happens when an excited molecule emits photons. This happens as a process when an orbital electron of the molecule gets excited to a higher quantum state and then falls into the ground state and emits a photon. Photobleaching is the irreversible decomposition of the fluorescent molecules into the excited state because of their interaction with molecular oxygen before emission. Photobleaching is a stochastic process; each molecule will last for a different amount of time before photobleaching.

Photobleaching is utilized in a technique known as fluorescence recovery after photobleaching (FRAP), which is useful mechanism for investigating the diffusion and motion of biological macromolecules. The method is based upon photobleaching a sharply defined region of the specimen by an intense burst of laser light, accompanied by the subsequent observation of the rates and pattern of fluorescence recovery in the photobleached area.

To quantify the efficiency of a fluorophore a value called *quantum efficiency* is assigned to every fluorophore. Quantum efficiency is the ratio of the number of photons emitted to the number of photons absorbed. For example, the quantum efficiency of GFP has been reported as ~ 0.76.

An ideal fluorophore has multiple properties: (1) it has high absorption and fluorescence quantum yield, (2) shows steady emission intensity, (3) does not perturb

the host molecule, (4) stays photoactive over a long time under intense illumination.

The fluorophores that have been used in the work of this thesis are cy3, Alexa488, rhodamine 6G, GFP, and YFP (yellow fluorescent protein). in general, some of the commonly used fluorophores in *in vitro* studies are cyanine family (e.g. cy3, cy5, cy7), the Alexa family (e.g. Alexa 488, Alexa 532) or the rhodamine family (e.g. rhodamine 6G). Also, autofluorescent proteins such as GFP or YFP have a huge advantage since they do not need labeling which makes them suitable for live cell imaging. GFP [19] which is 27 kDa and emits bright green fluorescence when excited by blue light at excitation peak of 498 nm. This protein was first isolated from jellyfish, and now is widely used in biophysics imaging.

Fluorescence photons contain valuable information. Different dimensions of information can be gained from the photon emission of the fluorophore molecules in solution [25]. These include: polarization direction from the fluorescence anisotropy[8], photon emission time from the fluorescence lifetime, fluorescence intensity, fluorescence quantum yield, fluorescence excitation and emission spectrum, and distance between fluorophores (e.g. FRET). Also, the number of emitters within a single diffraction limited region can be counted by temporal means exploiting the photobleaching of the emitters [26]. All of this means that by combining different detection schemes, useful information can be harvested from a fluorophore.

2.4.7 Instrumental Approach to TIRF Microscopy

There are two basic approaches to setting up a TIRF microscopy system: prism-type TIRF and objective-type TIRF [15]. This can be achieved with an upright or inverted optical microscope. The explanations in below are for TIRF achieved with inverted microscope.

In prism-type TIRF a prism is used as the medium with higher index of refraction (in comparison to the liquid sample that has lower index of refraction) for achieving the correct critical angle. In this case a kinetic beam director mirror is needed for adjusting the angle of the collimated incident light and maneuvering across the sample for finding the area of interest for imaging. The kinetic mirror is the last mirror before the prism, as show in Figure 2.10. Fine tuning of the incident angle can be achieved by manipulating the knobs on the kinetic mirror. Every time that the microscope stage is moved for imaging a new location the angle of the excitation light has to get fine tuned as mentioned. Also, in prism-type TIRF a focusing lens is mounted in a xyz translator with one of the axes along the direction of the collimated excitation beam. This lens is right before the prism or the kinetic mirror as shown in Figure 2.10 for enabling the achievement of the smallest surface area of the incident beam on the imaging spot, which in return maximizes the incident light's intensity on the imaging area, which in return results in increasing the photon emission of the excited fluorophores. In our setup the focusing lens ($f = 20\ cm$) helps to focus the beam to an area of 40 μm by 20 μm. This results in an excitation intensity of 0.1 KW/m^2 for

our lowest laser power, and an intensity of 18 KW/m^2 for the highest laser power.

In the beam path from the laser to the microscope there are usually multiple elements: (1) a wavelength selector is put right after the laser if a multicolor laser is used, (2) a beam expander, which can be a combination of a pair of lenses or mirrors, is used (the wider the beam at the focusing lens, the thinner the width of the TIRF-illuminated area), (3) a kinetic mirror, which as explained above is used for directing the beam to the prism at the angles above the critical angle, and (4) a focusing lens, for creating the smallest illumination spot for higher intensity. In the objective-type TIRF the total internal reflection is achieved via the objective itself.

The limitations of prism-type TIRF setup are (1) the identification of the sample surface excitation area is difficult, (2) the prism covers or blocks the top side of the slide, which is the fused silica side and is the imaging surface where the evanescent wave is created and is therefore very inconvenient for manipulation, and (3) it requires expensive fused silica slides. Moreover, the limitations of objective-type TIRF are that it requires an oil immersion TIRF objective with numerical apertures (NA) of 1.4 and above. Objective-type TIRF gives slightly higher background than prism-type TIRF. Also, the TIRF objectives with 1.45 NA are known to introduce problems like spherical and chromatic aberration (spherical aberration occurs when light rays strike the lens near its edge, and chromatic aberration is caused by the differences in the refractive index for different wavelengths of light) and the 1.65 NA requires toxic immersion oil.

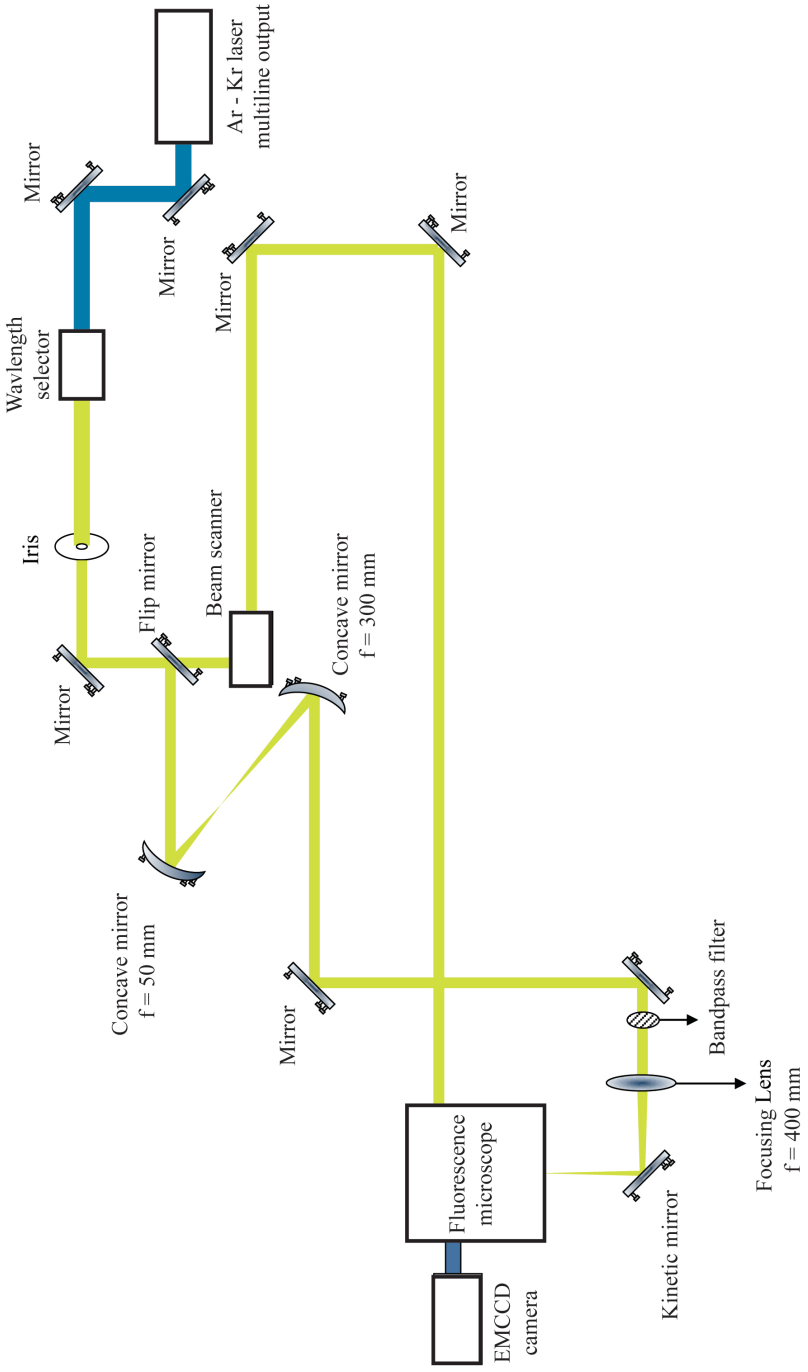

Figure 2.10: The schematics of the TIRF and epifluorescene microscopy in our lab.

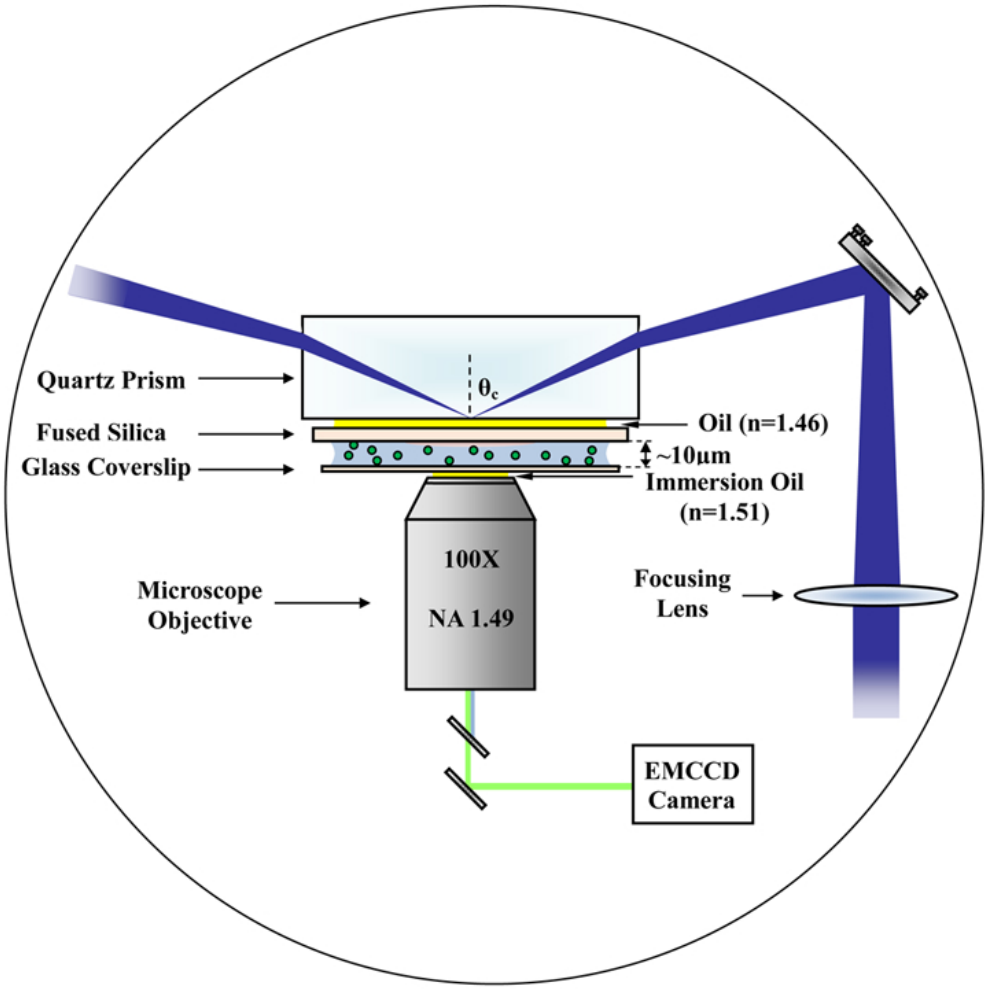

Figure 2.11: Close-up view at a TIRF setup. Notice the focusing lens for creating the smallest cross section for creating the maximum intensity, and the kinetic mirror for fine tuning the TIRF angle.

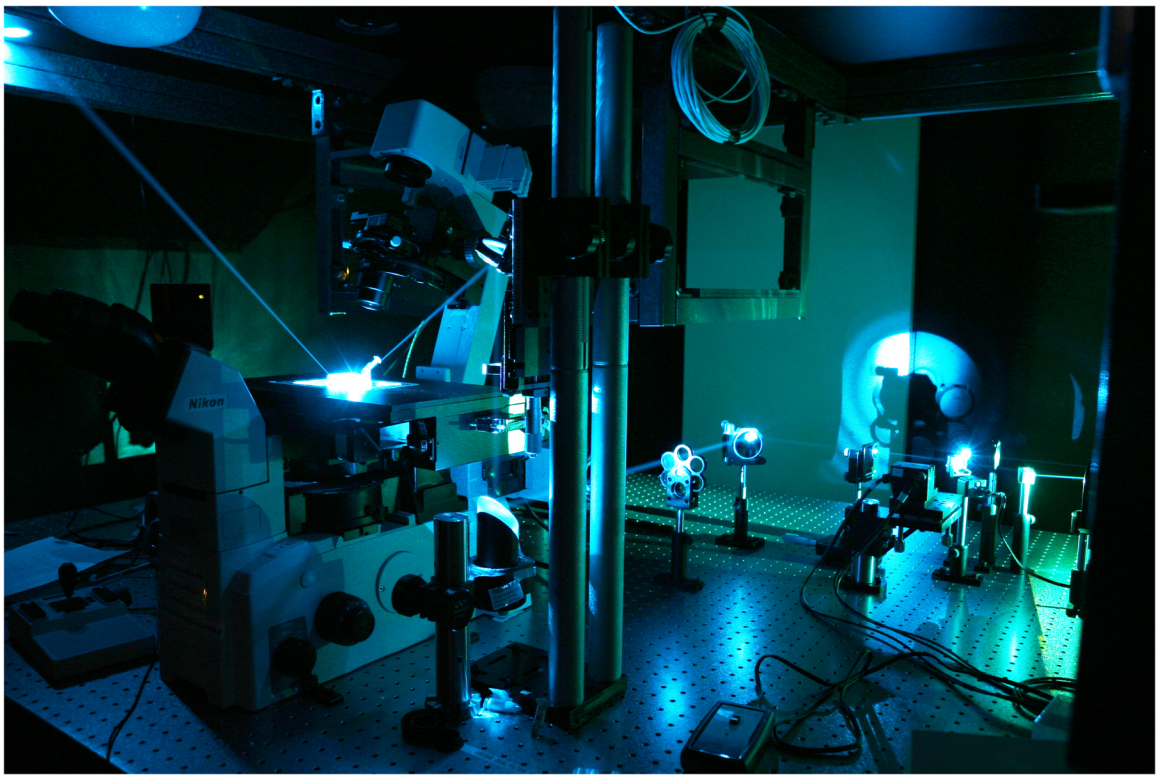

Figure 2.12: This figure shows a picture of our single molecule TIRF microscopy setup. In the picture you can see a blue laser light that is illuminating the prism at the TIRF angle.

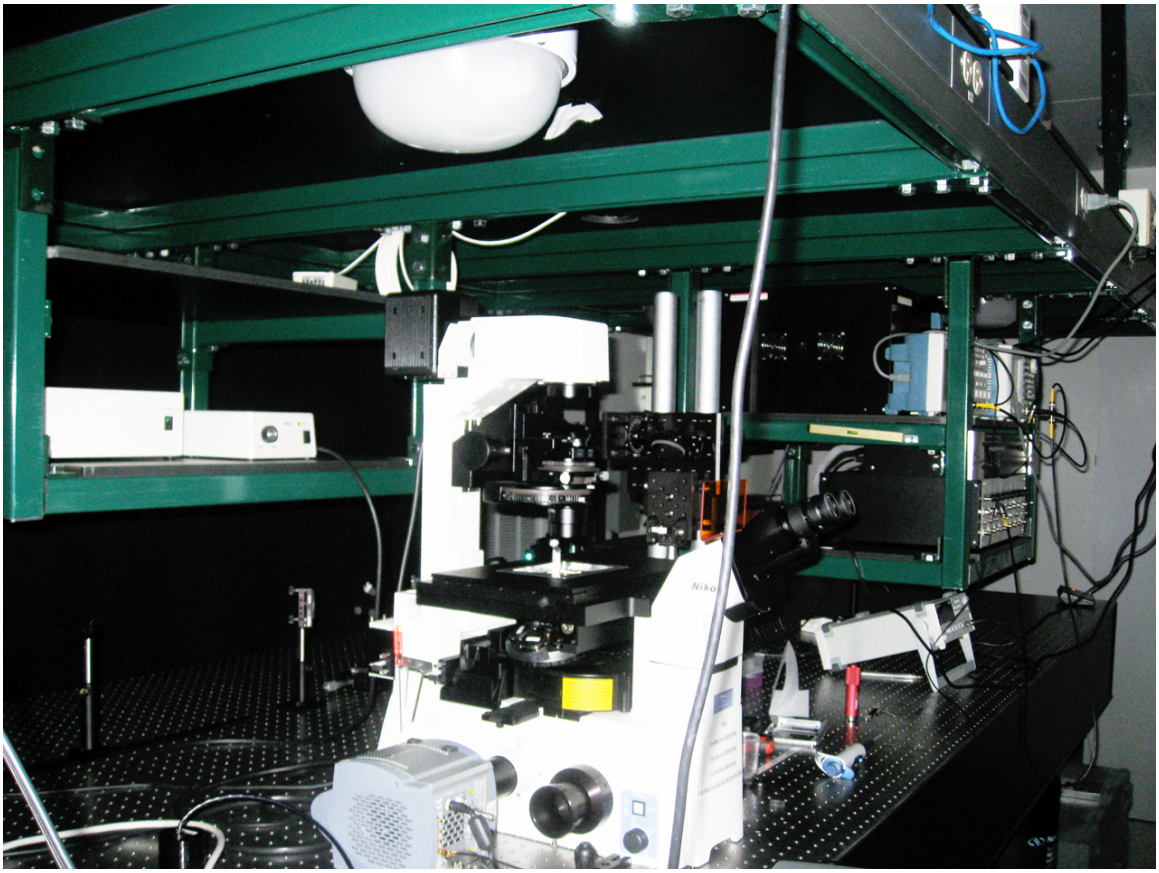

Figure 2.13: This figure shows a picture of our single molecule TIRF microscopy setup. IN this picture the Nikon microsope and Andor EMCCD camera that have been used in the work of this thesis are shown

2.5 Brownian Motion

Brownian motion is the random walk of particles in a fluid like gas or a liquid. A random walk is a stochastic process, and describes a trajectory that consists of successive random steps. When a molecule undergoes Brownian diffusion in a liquid like water it randomly gets pushed around by the water molecules, therefore it takes random steps that are statistically independent of each other. Figure 2.14 shows the simulation results for 20 particles that undergo 100 steps of Brownian diffusion that starts from x= 0 with a step size between -1 and +1 in one dimension. Figure 2.14B shows that the mean displacement of these particles after 100 steps is centered around zero; the particles started at x = 0 and still after 100 steps their mean position $< x >$ remains zero. A feature of Brownian motion is that even though the particles go nowhere on average, the spreading of the particles in one dimension increases with time by the following equation

$$< x^2 >= 2Dt \tag{2.14}$$

where D is the diffusion coefficient and the root mean displacement $\sqrt{< x^2 >}$ is a measure of the spreading of the particles or how far they go. Since the diffusive motion for each dimension of x, y and z are independent of each other, this relation is as following in 3D

$$< R^2 >= 6Dt \tag{2.15}$$

This relation shows that for example in order for a particle to diffuse 10 times as far it takes 100 times as long. The diffusion coefficient D characterizes the migration of particles of a given kind in a given medium at a given temperature, and was first formulated by Einstein and Smoluchowski as follows:

$$D = \frac{kT}{f} \tag{2.16}$$

where f is the frictional drag coefficient, and k is the Boltzmann constant. For a spherical particle

$$f_{sphere} = 6\pi\eta a; \tag{2.17}$$

η represents the fluid viscosity and a is the particle's radius. The Einstein-Smoluchowski equation was a historical equation because it was one of the first ways by which the Boltzman constant k was determined, and the exact number of atoms in a mole which is the Avogadro number N_0 was calculated.

Figure 2.14C shows the linear relationship between root mean square $\sqrt{< x^2 >}$ and time t for the simulation data shown in Figure 2.14.A. The slope of such a curve could give the diffusion coefficient D for any measurement.

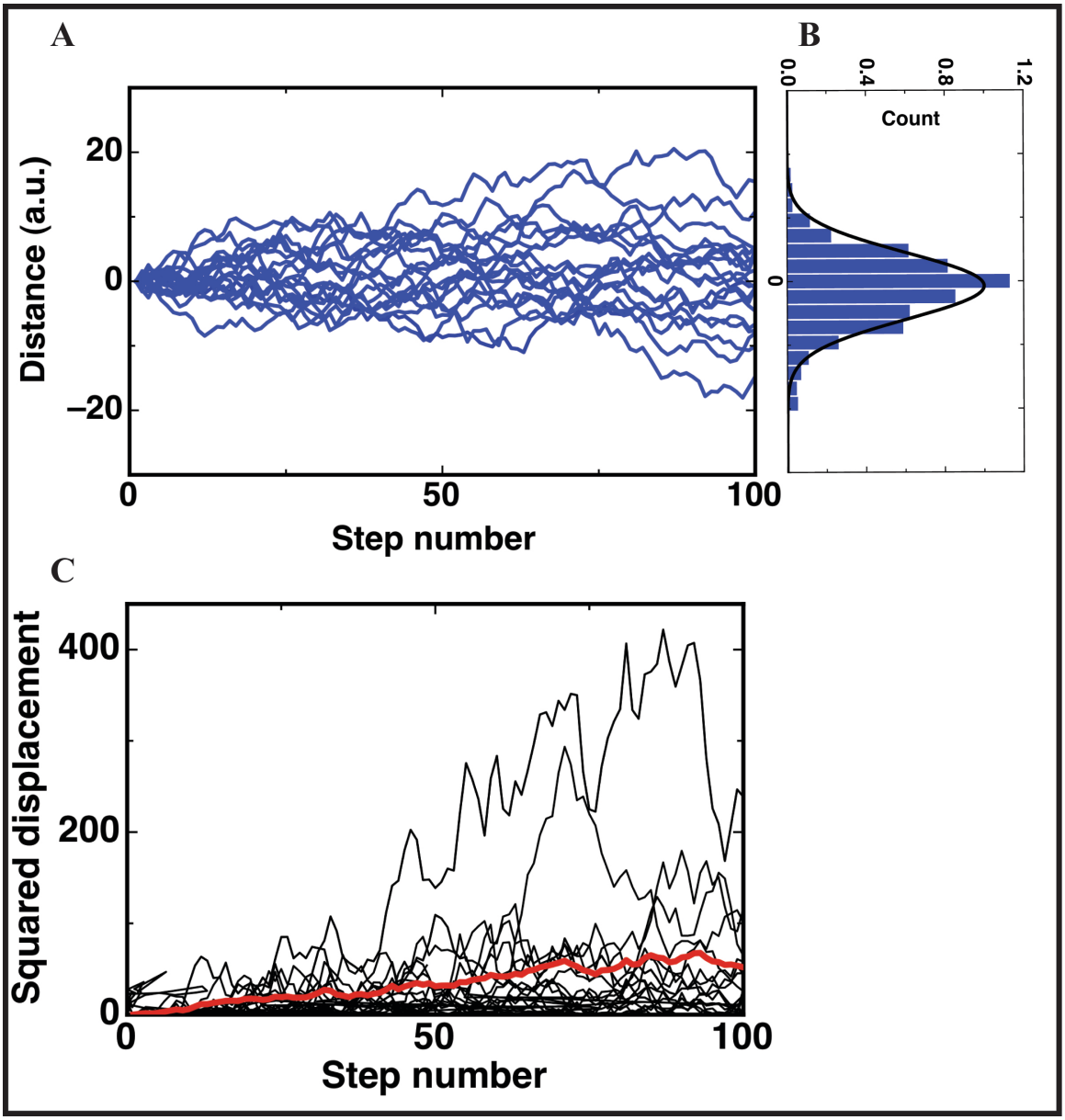

Figure 2.14: (A) Simulation of 20 random walks starting from x = 0 with step size between +1 and -1 lasting 100 steps. (B) The location distribution of the 20 particles after 100 steps has $< x >= 0$, and (C) shows that the mean square displacement (MSD) of these random walks has a linear dependence with time. The MSD curve is shown in red color, and the square displacements are black curves.

Chapter 3

Single-molecule imaging of protein adsorption mechanisms onto surfaces

3.1 Preface

This project began as a small project and the results were published in the *Microscopy Research and Technique* in Summer 2011. This project came along as I was attempting to perform other experiments (e.g. stretching the Lambda DNA via protein interaction with the fused silica surface). The proteins that we were using for stretching the DNA were streptavidin and biotin. We decided to focus on the results of protein interaction with the surface and postpone the DNA stretching project to future.

3.2 Abstract

Protein-surface interactions cause the desirable effect of controlled protein adsorption onto biodevices as well as the undesirable effect of protein fouling. The key to controlling protein-surface adsorptions is to identify and quantify the main adsorption mechanisms: adsorptions that occur (1) while depositing a protein solution onto dry surfaces and (2) after the deposition onto wet surfaces. Bulk measurements cannot reveal the dynamic protein adsorption pathways and thus cannot differentiate between the two adsorption mechanisms. We imaged the interactions of single streptavidin molecules with hydrophobic fused-silica surfaces in real-time. We observed both adsorbed proteins on surfaces and diffusing proteins near surfaces and analyzed their adsorption kinetics. Our analysis shows that the protein solution deposition process is the primary mechanism of streptavidin adsorption onto surfaces at the sub-nanomolar to nanomolar protein concentrations. Furthermore, we found that hydrophilic fused-silica surfaces can prevent the adsorption of streptavidin molecules.

3.3 Introduction

Controlled surface adsorption of proteins is important for devices such as protein-based biosensors and protein microarrays, but on the other hand, uncontrolled accumulation of proteins onto surfaces causes undesirable protein fouling[27, 28, 29]. In addition, when protein-surface contact is involved in a physical process, controlling

protein-surface adsorption is necessary to ensure minimal perturbation to protein concentration and characteristics in solution. For these reasons, it is necessary to identify and quantify mechanisms responsible for protein adsorption to surfaces.

The first step in most protein-based biological studies and applications involves introducing a protein solution to a device (e.g., a pipette tip, a transfer tube, a glass slide, etc.). It is known that proteins can dissolve in water as well as accumulate at the air-water interface [30, 31, 32, 33]. When these proteins encounter a device surface, some adsorb during the protein-solution deposition process while others adsorb after the surface is wet. These adsorptions are the result of electrostatic, van der Waals, and hydration interactions between proteins and surfaces [34]. While most studies focused on surface adsorptions of the dissolved proteins after deposition [35] the effects of the deposition process on protein-surface adsorption are not clear.

In order to precisely identify and quantify mechanisms responsible for protein-surface adsorptions, we investigate the adsorption process of individual proteins by single molecule fluorescence imaging. Prior studies of protein-surface interactions mainly used bulk ensemble measurements, in which the concentrations of all adsorbed proteins were measured and thus adsorptions due to different mechanisms could not be differentiated [36, 37].

In our study, we used Total Internal Reflection Fluorescence (TIRF) microscopy imaging method to record the interplay of a single molecule, streptavidin-Cy3 and streptavidin-Alexa555, with hydrophobic and hydrophilic fused-silica surfaces in real time. Images of both adsorbed proteins at the surface and free 3D-diffusing proteins

near the surface were captured to reveal the adsorption pathways and kinetics for both irreversible and reversible adsorptions.

3.4 Materials and Methods

3.4.1 Protein Deposition

Figure 3.1 A - C schematically illustrates the method of depositing a protein solution onto a surface. Five microliters of streptavidin-Cy3 (SA1010, Invitrogen, Carlsbad, CA) or streptavidin-Alexa555 powder (S21381, Invitrogen, Eugene, OR) dissolved in 0.5X TBE buffer (pH = 8) to 0.3 nM concentration were deposited onto a fused-silica surface (6W675-575 20C, Hoya Corporation USA, San Jose, CA) by pipette. Streptavidin is a 52.8-kDa tetrameric protein measuring 4.5 × 4.5 × 5 nm in size (Scouten and Knecny, 1992). It has an isoelectric point of 6.3 (Sivasankar et al., 1998) and is negatively charged in solutions with a pH 8. Protein concentrations of less than nanomolars were used such that images of individual adsorbed proteins on surface and 3D-diffusing proteins in solution could be resolved without overlapping. The droplet is flattened by a coverslip, whose edges were sealed with nail polish. Because hydrophobic surfaces are known to yield higher protein-surface adsorption affinity than hydrophilic surfaces [38], the surfaces in Figs.3.2, 3.3 and 3.3 A were treated to be hydrophobic with a $\approx 90^{\circ}$ water contact angle by dipping oxygen-plasma-cleaned fused-silica chips into a 5% dichlorodimethylsilane in chloroform solution for 10 sec. The glass coverslip was cleaned using oxygen plasma and was hydrophilic.

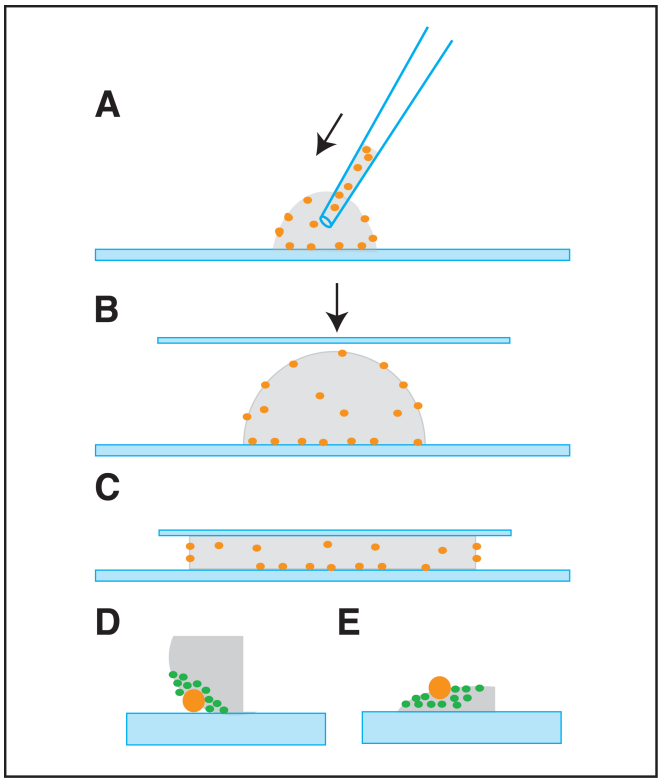

Figure 3.1: (A) – (C) Schematic of the protein (orange) deposition process. (D) and (E), protein and water (blue) compete for binding to hydrophobic and hydrophilic surfaces, respectively.

In the schematics, we showed proteins that are adsorbed on the surface, accumulated at the air-water interface, and dissolved in the solution. Using the aforementioned protein-solution deposition method, two interfaces are made: the initial air-water interface during the deposition process (for irreversible adsorptions), and the water-surface interface at the later stage (for reversible adsorption).

3.4.2 Imaging Setup

Single-molecule imaging was performed using a Nikon Eclipse TE2000-S inverted microscope (Nikon, Melville, NY) in combination with a Nikon 100X objective (Nikon,

1.49 *N.A.*, oil immersion). Samples were excited by a prism-type TIRF setup with a linearly polarized 532 nm laser line focused to a 40 μm $\times$ 20 μm region (568 nm line was used for streptavidin-Cy3). The laser excitation (I70C-SPECTRUM Argon/Krypton laser, Coherent Inc., Santa Clara, CA) was pulsed with exposure times of submilliseconds and 28 ms, and the durations between images were 4 min for Figure 3.2, 38 min for Figure 3.3, and 30 ms for Figure 3.4. The excitation intensities were 0.3 kW/cm^2 to 8 kW/cm^2. Images were captured by an iXon back-illuminated electron multiplying charge coupled device (EMCCD) camera (DV897ECS-BV, Andor Technology, Belfast, Northern Ireland). An additional 2X expansion lens was placed before the EMCCD, producing a pixel size of 79 nm. For streptavidin-Alexa555 molecules, the excitation filter was 530 nm/10 nm and the emission filter was 580 nm/60 nm; for streptavidin-Cy3 molecules, the excitation filter was 568 nm/10 nm and the emission filter was 605 nm/50 nm.

3.5 Data Analysis

Movies were made by synchronizing the onset of camera exposure with laser illumination. The gain levels of the camera were adjusted such that none of the pixels of a single molecule's point spread function (PSF) reached the saturation level of the camera. For a selected image, the intensity values of 20 $\times$ 20 pixels centered at the molecule were recorded. A one dimensional intensity profile of the molecule was obtained by averaging the 20 transverse pixel values at each of the 20 horizontal

pixels. The profile was then fitted to a 1D Gaussian function using the least squares curve-fitting algorithm (lsqcurvefit) provided by MATLAB (The Mathworks, Natick, MA):

$$f(x) = f_0 \exp\left[-\frac{(x - x_0)^2}{2s^2}\right] + \langle b \rangle, \tag{3.1}$$

where f_0 is the amplitude, x_0 is the center, $\langle b \rangle$ is the mean background value, and s is the standard deviation (SD) of the molecule's intensity profile. Using the SD value of a single molecule intensity profile, we determined whether the molecule was adsorbed on the surface or diffusing in the solution (see Results below).

3.6 Results

We observed three types of behavior associated with streptavidin molecules on or near fused-silica surfaces, categorized according to their different surface adsorption characteristics: (1) irreversible adsorption induced by the protein deposition process, (2) reversible adsorption caused by protein interactions with wet surfaces, and (3) non-adsorbing proteins that freely diffuse near the surface.

Figure 3.2 shows a time series of streptavidin-Alexa555 images on or near a hydrophobic fused-silica surface, starting immediately after the deposition with time interval of 4 minutes. The diffraction-limited dots and the larger "blurs" are adsorbed proteins on the surface and diffusing proteins in the solution, respectively. The long interval of 4 minutes between the images was chosen to minimize fluo-

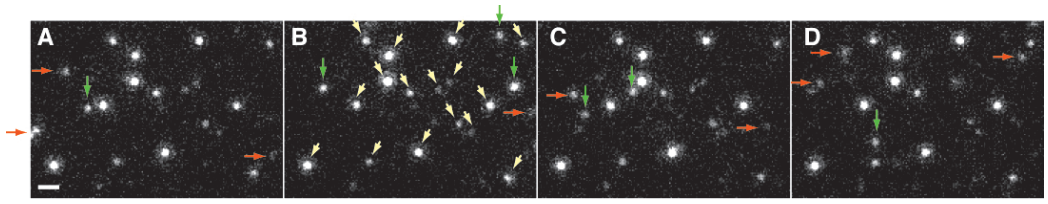

Figure 3.2: (A) – (D), time series of streptavidin-Alexa555 adsorbed on and diffusing near a hydrophobic fused-silica surface. The first image was acquired right after the deposition, and other images were 4 minutes apart. Yellow slanted arrows indicate irreversibly bound proteins due to the deposition process (denoted in B); green vertical arrows indicate reversibly bound proteins after the deposition (A – D); and red horizontal arrows indicate 3D-diffusing proteins (A – D). The scale bar is 1 μm.

rophore bleaching from long illumination [39, 40]. In order to determine whether a fluorescent image is an adsorbed protein or a freely diffusing protein, we measured the SD of the molecule's fluorescence intensity profile.

If the SD value was within the diffraction limit of the apparatus ($\approx 120 \pm 20$ nm), the molecule was an adsorbed protein on the surface [23, 41]; if it was larger than 140 nm, the molecule was a diffusing protein.

The small dots whose SD values were below 140 nm that didn't change location in all subsequent four images are denoted by yellow slanted arrows. Because they do not change positions after the deposition, these are identified as irreversibly adsorbed proteins. And since no additional irreversibly adsorbed proteins that were observed after the deposition, these proteins must have been adsorbed during the protein-solution deposition process. The small dots whose SD values were below 140 nm and were observed only in one image are denoted by green vertical arrows. Due to their momentary stay on the surface, these are reversibly bound proteins whose adsorption occurred after the deposition. The blurred dots with SD larger than 140 nm and

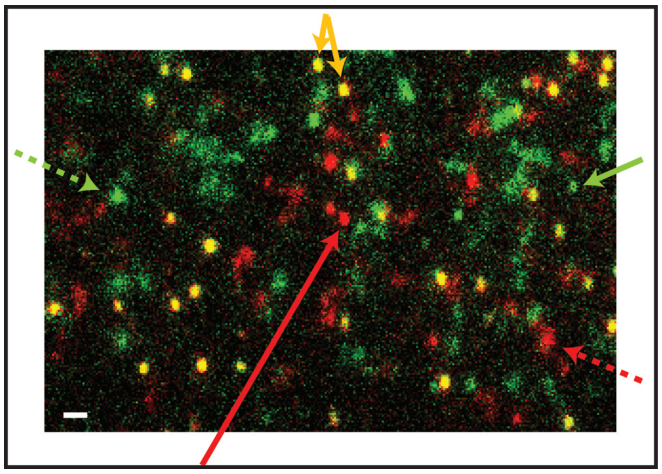

Figure 3.3: Superposed TIRF images of the streptavidin-Cy3 molecules immediately after deposition (false-colored red) and 38 minutes after the deposition (false-colored green). When the images overlap, the red and green dots yield orange dots (denoted by orange solid arrows). The single-colored red and green molecules with SD less than 140 nm (solid green and red arrows) are reversibly adsorbed proteins after the deposition. The large green and red blurs are 3D-diffusing molecules near the surface (dashed red and green arrows). The scale bar is 1 μm.

were only observed in one image are denoted by red horizontal arrows; these are 3D diffusing proteins near the surface.

In order to better illustrate the bahavior of the three types of proteins on and near the fused-silica surfaces – (1) the irreversibly adsorbed proteins that were bound at the same locations for a long time after the sample deposition, (2) the reversibly adsorbed proteins and (3) the 3D-diffusing proteins that change locations from one image to another, we superpossed two images taken at different times in Figure 3.3. The first one was taken immediately after the deposition, and the second image at 38 minutes after the deposition. The protein dots and "blurs" in the first image were false-colored red, and in the second image, they were false-colored green. When the two images were superposed, the overlapped protein dots were represented by orange,

and the proteins that do not overlap retain their original color. By using this method, the orange irreversibly adsorbed proteins can be clearly differentiated from the red and green reversibly adsorbed proteins and diffusing proteins.

Streptavidin adsorption mechanisms are elucidated by analyzing Figure 3.3, in which 32 molecules were irreversibly adsorbed, 2 were reversibly adsorbed, and 30 were 3D-diffusing near the surface. These results indicate that at the molecular concentration of 0.3 nM, the main contribution to streptavidin-surface adsorption is the protein-deposition process, which accounts for $\sim 94\%$ of the total surface-adsorbed proteins. The protein-surface interactions after the deposition are responsible for only $2/34 \approx 6\%$ of the total adsorption. The majority of the 3D-diffusing proteins near surfaces do not bind to the surfaces: only $\approx 2/(30/\text{frame} \times 6 \text{ frames}=180) \approx 1\%$ proteins that encountered the surface reversibly bound to it. We also measured various increasing streptavidin concentrations up to 5 nM (at which concentration individual protein images began to overlap, rendering adsorption studies difficult), and observed similar results as in Figure 3.2 and 3.3. These results indicate that the deposition process is the dominant mechanism for streptavidin adsorption to hydrophobic fused-silica surfaces for up to nM concentrations.

In order to obtain the reversible adsorption kinetics, we used a faster frame imaging rate of 33 Hz and exposure time of 28 ms. Figure 4A shows montage of a molecule diffusing towards, binding to, and dissociating from a surface. Going from top to bottom of the montage, the large blurs in images 2 and 8 are the incoming molecule moving towards the surface, and the outgoing molecule leaving the surface, respectively.

The dissociation time of this molecule is ≈ 140 ms (5 frames). About 200 reversibly bound streptavidin molecules were studied and the mean reversible binding time of streptavidin to dichlorodimethylsilane hydrophobic surfaces was ≈ 200 ms.

To verify that the blurred dots in Figure 3.2, 3.3, and 3.4 with SD larger than 140 nm are 3D-diffusing molecules, we studied how the SDs of these molecules change with exposure time. If they are 3D-diffusing molecules, SD should increase with exposure time since SD is a reflection of how far a molecule diffuses during exposure. The penetration depth of our TIRF evanescent light is ≈ 150 nm, so for this study we chose short exposure times such that proteins would not diffuse beyond twice of the penetration depth to ensure complete capture of the 3D-diffusing processes. With the Brownian dynamics calculation of $\langle x^2 \rangle = 2D_3 t$, where $\langle x^2 \rangle$ is the mean square displacement of 3D-diffusing molecules in one direction, and $D_3 \approx 5 \times 10^7$ nm^2/s is the 3D-diffusion coefficient for streptavidin with ≈ 5 nm diameter, we determined the appropriate exposure time t in the sub-millisecond range so that $\sqrt{\langle x^2 \rangle}$ is less than 300 nm.

Figures 3.5A, B, and C show representative 3D-diffusing streptavidin-Cy3 molecules' intensity profiles near a hydrophilic fused-silica surface with increasing exposure times of 0.3, 0.7, and 1 ms, respectively. It is readily seen that the width of the molecules' intensity profiles increases with exposure time. Figure 3.5D shows the SD distributions for the three exposure times: the mean SD values are larger than 140 nm and increasing with exposure time. This confirms that the observed molecules with SD larger than 140 nm are indeed 3D-diffusing streptavidin-Cy3 molecules near the

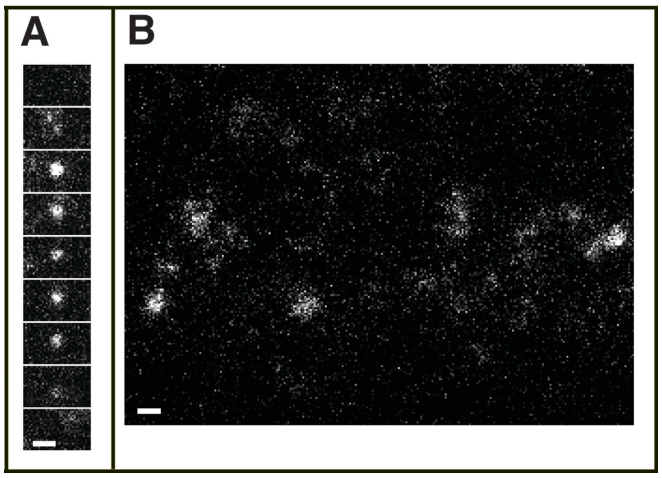

Figure 3.4: (A) Montage of a reversibly bound molecule diffusing towards, binding to, and dissociating from the surface, respectively from top to bottom. (B) 3D-diffusing proteins near a fused-silica hydrophilic surface. Note that there are no adsorbed proteins on the surface. Scale bars are 1 μm.

surface.

So far we showed that for a "sticky" hydrophobic surface, the dominating mechanism responsible for streptavidin fused-silica surface adsorption at sub-nanomolar and nanomolar concentrations is the deposition process. For hydrophilic surfaces that are believed to be less "sticky" to the same proteins, how does the protein-surface adsorption change? Fused-silica chips were made hydrophilic by performing oxygen plasma cleaning for 2 minutes. We found complete elimination of irreversible and reversible streptavidin-surface adsorptions for several hours of observation time. Figure 3.4B shows that there were only 3D-diffusion proteins near the hydrophilic surface and no adsorbed proteins. This result indicates that the surface treatment by oxygen plasma cleaning can prevent streptavidin fouling on fused-silica surfaces.

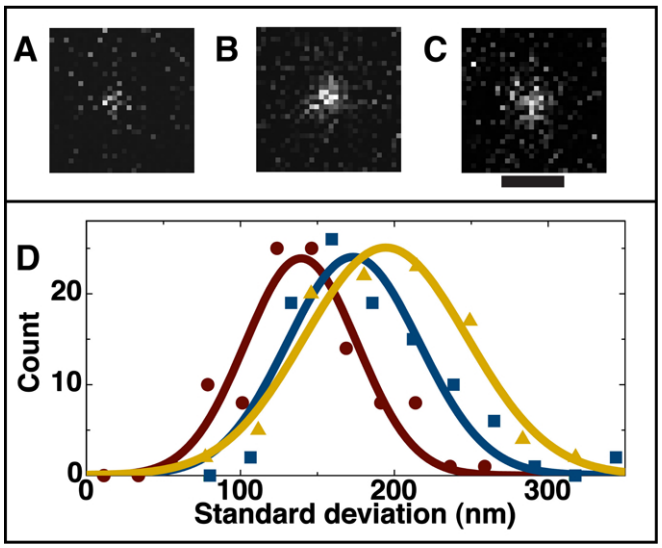

Figure 3.5: Images of representative single 3D-diffusing molecules with exposure times of (A) 0.3 ms, (B) 0.7 ms, and (C) 1 ms. The width of the molecules increases with exposure time and the 1D fit SD values are 135 nm (A), 180 nm (B), and 204 nm (C), respectively. (D) SD distribution of the diffusing molecules' intensity profiles for exposure times of 0.3 ms (red), 0.7 ms (blue), and 1 ms (yellow). The SD values are 139.5 ± 3.6 nm (mean ± standard error of the mean), 173.3 nm ± 4.2 nm, and 194.5 ± 5.2 nm, respectively. The scale bar is 1 μm.

3.7 Discussion

3.7.1 Deposition-process-associated irreversible Adsorptions

What is the possible mechanism that causes the irreversible protein adsorption during deposition? Assuming that the surface is chemically stable from the moment water touches the surface, during the deposition, a dissolved protein should have the same binding affinity to the surface as after the deposition. However, during the deposition process, air is an additional component in the protein-surface interface and this may result in a different protein-surface binding affinity and consequently, irreversible adsorption for proteins at the air-water interface.

To test this hypothesis, we transferred protein solutions to a wet surface and imaged in real time. Since there was no air-water interface in this setup, only dissolved protein in the solution can be imaged, therefore no irreversibly adsorbed proteins should be observed. We indeed observed only reversibly adsorbed proteins on surfaces and diffusing proteins in solution. No irreversibly adsorbed proteins were seen. The result indicates that the proteins at the air-water-interface are the irreversibly adsorbed proteins, and this adsorption occurred only during the deposition process.

We further investigated the ratio of protein concentrations at the air-water interface and in bulk by imaging air-water-interface proteins in a droplet on glass, using the method described by Deng et al., 2006. We found the concentrations were comparable. This observation is consistent with our results in Figure 3.3 that half of the proteins imaged in one snapshot were irreversibly adsorbed on the surface, and thus

supports the notion that the air-water interface proteins are the irreversibly adsorbed ones during the deposition process.

3.7.2 Reversible Adsorptions

The reversible adsorptions that occurred after the deposition are due to genuine interaction of dissolved streptavidin with surface chemical groups. These interactions include hydrophobic, ionic, and van der Waals interactions [37]. Streptavidin is negatively charged and hydrophilic in a buffer at pH 8 [42]. The fused-silica surface groups can be dimethylsilane or silanol, depending on whether the surface is hydrophobic or hydrophilic. Our observation of reversibly adsorbed proteins on hydrophobic surfaces but not on hydrophilic ones indicates that the net binding affinity between streptavidin and the surface groups is strong enough for binding to occur for the hydrophobic surfaces, but not for the hydrophilic surfaces.

3.7.3 Other Hydrophobic Surfaces and Proteins

To determine the role hydrophobicity plays in streptavidin-surface adsorptions, we investigated streptavidin interaction with three differently treated hydrophobic surfaces: RainX (SOPUS Products, Houston, TX), lab detergent (Versa-Clean, 04-342, Fisher Scientific, Pittsburgh, PA), and 0.1 wt% solution of dodecyltrichlorosilane in hexane. The contact angles for these surfaces were $\approx 90^{\circ}$. The adsorption results were the same as for the dichlorodimethysilane treated surfaces: we observed both irreversible and reversible adsorptions, with the irreversible adsorptions outnumbering

the reversible adsorptions. We also changed the degree of hydrophobicity by tuning the ratio of dichlorodimethylsilane to chloroform, and hence the contact angles from approximately 30° to 90°. With decreasing hydrophobicity, we observed less irreversible and reversible adsorptions . These observations indicate that hydrophobicity of a fused-silica surface can effectively dictate adsorption of streptavidin (or proteins). Further supports come from our studies of fused-silica surface adsorptions of green fluorescent proteins and Lactose repressor proteins; similar results to streptavidin were obtained.

3.7.4 Competition for Surface Binding Between Protein and Water Molecules

In addition to proteins, water molecules also have binding affinity to surfaces, and they compete with streptavidin for surface binding. This competition may also contribute to the observed streptavidin adsorptions.

In Figures 3.1D and E we sketch possible competitions between a protein molecule and water molecules for binding to hydrophobic and hydrophilic surfaces, respectively. Since streptavidin is hydrophilic at pH 8, when both streptavidin and water approach a hydrophobic surface, water tends to avoid the surface more than streptavidin, leading to an effectively increased protein exposure to the surface and consequently increased adsorption (Figure 3.1D). For the hydrophilic surface, water molecules are more tightly bound to the surface, leading to an effectively decreased streptavidin

adsorption (Figure 3.1E).

3.7.5 Deposition Variations

Variations to procedures in transferring proteins to devices include changing the fluid flow speed. We varied the pipetting speed when depositing proteins onto dry hydrophobic and hydrophilic surfaces, varying the fluid flow speed by at least 10-fold. No difference in irreversible and reversible adsorption characteristics was observed.

3.8 Conclusion

In summary, single-molecule real-time imaging of protein-surface interactions provides an invaluable tool for elucidating adsorption mechanisms and obtaining adsorption kinetics. We have shown that irreversible and reversible adsorptions are highly process dependent at the sub-nanomolar to nanomolar concentrations. Our results indicate that in addition to regulating post-deposition protein-surface interactions, the deposition process must be taken into consideration in the design and interpretation of protein-surface adsorption studies. The observation that the surface adsorption of streptavidin can be eliminated or reduced with hydrophilic surface treatment may have important implications for prevention of protein fouling in biomedical devices.

Chapter 4

Single-Image Diffusion Coefficient Measurements of Proteins in Free Solution

4.1 Preface

This project was the primary project of my thesis. This project consisted of experiment, theory and simulation. All of the experimental work and the data analysis was performed by me as the main author, and the theory and simulations were done mostly by Michael DeSantis and Prof. Wang. This work was submitted in July 2011 for publication. The main text of the publication manuscript is presented in this chapter, and the simulation and theory are presented in the Supporting Materials section of the Appendices chapter of this thesis (SOM of our submitted manuscript).

4.2 Abstract

Diffusion coefficient measurements are important for many biological and material investigations, such as particle dynamics, kinetics, and size determinations. Amongst current measurement methods, single particle tracking (SPT) offers the unique capability of providing location and diffusion information of a molecule simultaneously while using only femptomoles of sample. However, the temporal resolution of SPT is limited to seconds for single-color labeled samples. By directly imaging three dimensional (3D) diffusing fluorescent proteins and studying the widths of their intensity profiles, we determine the proteins' diffusion coefficients using single protein images of sub-millisecond exposure times. This simple method improves the temporal resolution of diffusion coefficient measurements to sub-millisecond, and can be readily applied to a range of particle sizes in SPT investigations and applications where diffusion coefficient measurements are needed, such as reaction kinetics and particle size determinations.

4.3 Introduction and Motivation

Determination of particles' diffusion coefficients is important for many biological and material applications, such as single-molecule dynamics studies [40, 43, 44], biolochemical and pharmaceutical reaction kinetics studies [45, 46], and particle size and shape determinations [47]. Amongst current methods for measuring diffusion coefficients, which include nuclear magnetic resonance imaging (NMR) [48], dynamic light scattering (DLS) [49], fluorescence correlation spectroscopy (FCS) [2, 3, 4], and fluorescence recovery after photobleaching (FRAP) [50], single particle tracking (SPT) offers the unique capability of simultaneous location and diffusion coefficient determination. This is essential for molecular mechanism investigations in heterogeneous environments, such as inside a cell's cytoplasm [51], flagella [52], and membrane [53] *in vivo*, and on DNA molecules [40] *in vitro*. Due to this capability, and the additional advantage that SPT experiments require less than femtomoles of sample, SPT can be a powerful tool in diffusion coefficient measurements applicable to a large range of biological investigations *in vitro* and *in vivo* where supplies are scarce.

However, the drawback of using SPT for diffusion coefficient measurements is the low temporal resolution. In single-molecule fluorescence imaging studies, stationary or slowly moving (relative to the data-acquisition timescales) single molecule intensity profiles are called point spread functions (PSF), and are fit to Gaussian functions to determine the molecules' localization information. The centroid of the Gaussian function determines the lateral location of the molecule at the time of imaging, and

the standard deviation (SD) determines the axial location. In SPT diffusion coefficient measurements, consecutive locations of a single fluorophore are measured and from mean square displacement analysis of the particle's single trajectories, diffusion coefficients are obtained [40, 51, 54]. This method requires at least 20 consecutive location measurements for each single trajectory. With the current single-photon camera imaging rate of approximately 100 frames/sec for a finite-sized imaging area, 0.2 sec is required and 3D diffusion coefficient D_3 measurements up to order 10^5 nm^2/s have been reported [55]. This requirement of 0.2 sec is, however, too long for diffusion coefficient measurements of fast-moving molecules, such as nanometer-sized proteins that diffuse beyond the typical imaging depth of $\sim$ 400 nm of single-molecule imaging microscope setups in less than 1 ms (a typical 5 nm protein has $D_3 \approx 10^8$ nm^2/s and diffuses $\sqrt{2D_3t} \approx 447$ nm in 1 ms). A recent SPT method measures D_3 up to 1.7 $\times 10^7$ nm^2/s by labeling the particles with two colors [56]; however, multi-color-labeling may not be feasible for many biological particles of interest and thus restricts the applicability of the method.

A SPT method that can determine 3D diffusion coefficients of single-colored nanometer-sized biological entities in their native environment is highly desirable for *in vivo* and *in vitro* studies. In order to capture the molecule within the microscope's imaging depth, the imaging time needs to be less than 1 ms. Here we report a novel method that determines the diffusion coefficient of nanometer-sized Brownian molecules from the SD values of the molecules' intensity profiles using sub-millisecond exposure times. This is a single-image molecular analysis (SIMA) study

of dynamic molecules and is an extension of our previous stationary molecule investigations [41]. In this study we used eGFP as the nanometer-sized fluorescent molecule for measurements and analyses.

Since the imaging times in our method are less than 1 ms, the temporal resolution of diffusion coefficient measurements is improved by at least 1000-fold over the minutes-long FCS method (multiple measurements each of order 20-second long), 200-fold over the 0.2-sec long centroid SPT method, 50-fold over the typically 50-ms long FRAP method, and 10-fold over the two-color SPT method. Furthermore, the improvement in temporal resolution is achieved without compromising the precision of the D_3 measurements, and the single-image nature of the method avoids the photobleaching and limited lifetime photon problems associated with single-molecule fluorescence imaging studies. Below we show our measurement method that relates the SD of a 3D freely diffusing protein's intensity profile to its diffusion coefficient D_3. A prior study has used a similar concept to relate slow 2D diffusion coefficients (up to 1.1×10^6 nm^2/s) to a fluorophore's spot sizes [57]; here we extend the study to fast 3D diffusion.

4.4 Results

Figures 4.1 and 4.2 illustrate the principle of this method. In a finite exposure time, the intensity profile of a moving molecule is wider (or more blurry) compared to that of an immobile molecule. Figure 4.1A shows a 30 ms frame image of stationary eGFP

molecules adsorbed on a fused-silica surface, and Fig. 4.1D shows a 1 ms frame image of diffusing eGFP molecules near a hydrophilic fused-silica surface [58]. These figures clearly show that diffusing molecules images are blurry compared to that of immobile molecules. In Figs. 4.1B and 4.1E the intensity profiles of the stationary and diffusing eGFP molecules are plotted, and in Figs. 4.1C and 4.1F, the respectively selected intensity profiles are fitted to Gaussian functions. While both intensity profiles fit well to a Gaussian function, the width (or SD) of the diffusing protein's intensity profile is larger than that of the stationary protein.

In general, the final image of a diffusing molecule, like those in Fig. 4.1, is the sum of the emitted photons along its diffusion trajectory projected onto a 2D imaging screen during the exposure time. Figure 4.2A shows a simulated eGFP diffusion trajectory at 0.6 ms exposure time using 0.005 ms steps for clarity. The data are gray-scaled to correspond to the particle's axial locations (SOM text). The emitted photons, after photon-to-camera count conversion, were projected onto a 2D imaging screen and binned into our camera pixels each of 79×79 nm^2 in size (Fig.4.2B; gray image) and the corresponding diffusing eGFP PSF intensity profile was formed in the colored image above. The total photon count of this image was 414. The 2D Gaussian fit to the diffusing eGFP intensity profile is shown in Fig. 4.2C, yielding SD values in the x- and y-directions, s_x and s_y, respectively. $s_{x,y}$ values presented in this article are results from fitting to these experimental and simulated PSF data, and they were used to quantify the blur of diffusing eGFP molecules, and consequently, the diffusion coefficient D_3.

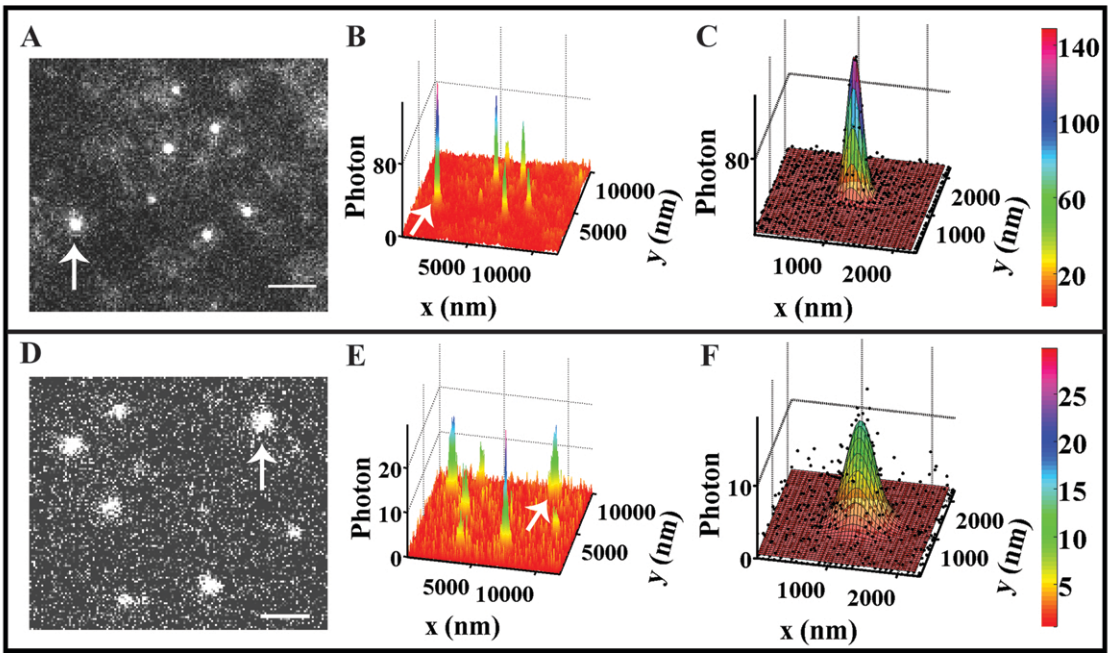

Figure 4.1: Comparing stationary to diffusing eGFP molecules. (A) An image of stationary eGFP molecules adsorbed on a fused-silica surface. Five of the seven molecules have signal-to-noise ratio (SNR) > 2.5. (B) Intensity profiles of the stationary eGFP molecules in (A) in photon counts. (C) Intensity profile (dots) and Gaussian fit (mesh) to the stationary eGFP molecule denoted by arrow in (A) and (B). For this molecule, the SNR is 9.8, $s_x = 107.2$ nm, and $s_y = 107.9$ nm. (D) Diffusing eGFP molecules near a reflective hydrophilic fused-silica surface at 1 ms exposure time. Six of the eight molecules have a SNR > 2.5. The scale bars for (A) and (D) are 2 μm. (E) Intensity profiles of the diffusing eGFP molecules in (D). (F) Intensity profile (dots) and Gaussian fit (mesh) to the diffusing eGFP molecule denoted by arrow in (D) and (E). For this molecule, the SNR is 3.5, $s_x = 202.2$ nm, and $s_y = 192.4$ nm. It is clear that the intensity profiles of diffusing molecules are wider (or have larger SDs) than that of stationary molecules.

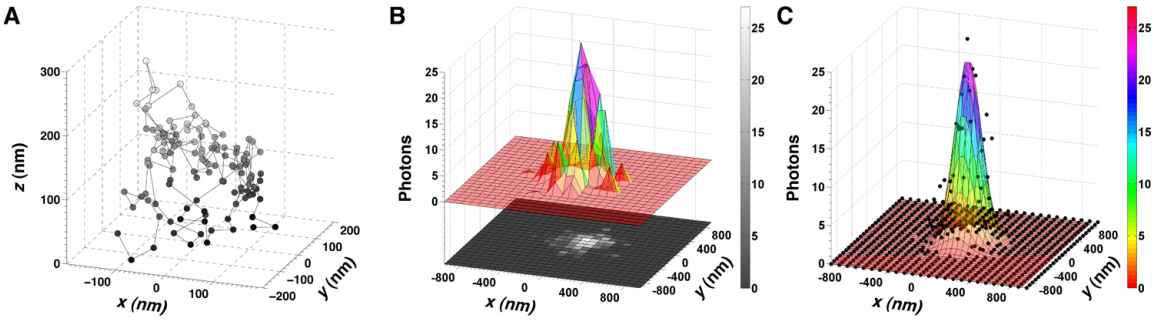

Figure 4.2: Simulated image formation and analysis process of a diffusing eGFP molecule. (A) Trajectory of a diffusing eGFP molecule in free solution under TIRF (total internal reflection fluorescence) evanescent excitation at the exposure time of 0.6 ms. The data is gray-scaled to correspond to the particle's axial locations (SOM Text). (B) The emitted photons from the trajectory form an intensity profile (colored plot), which is then projected onto a 2D camera screen (black and white image). (C) Gaussian fit (mesh) to the intensity profile of the diffusing eGFP (dots), where s_x = 119.4 nm, and s_y = 142.2 nm.

In order to determine D_3 from diffusing fluorophore images, we performed (i) experimental measurements, (ii) analytical calculations, and (iii) simulations and obtained SDs of diffusing eGFP intensity profiles at 0.3 to 1 ms exposure times. Below we show that when the experimental results were checked against theoretical calculation and numerical simulation results in Fig. 4.3A, the good agreement validates our method of measuring nanometer-sized fluorophore diffusion coefficients.

In experimental measurements, Fig. 4.4A shows representative eGFP images (chosen such that the molecule's respective s_x values were within ± 5 nm of the means to the respective diffusing eGFP intensity profile SD distributions in Fig. 4.4B) at 0.3, 0.7, and 1 ms exposure times. As expected, SD values of these respective single diffusing eGFP molecules increase from 136.4 to 160.9 and 175.5 nm, validating that SD provides a quantitive measure for the motion-induced blurriness of single fluorophore

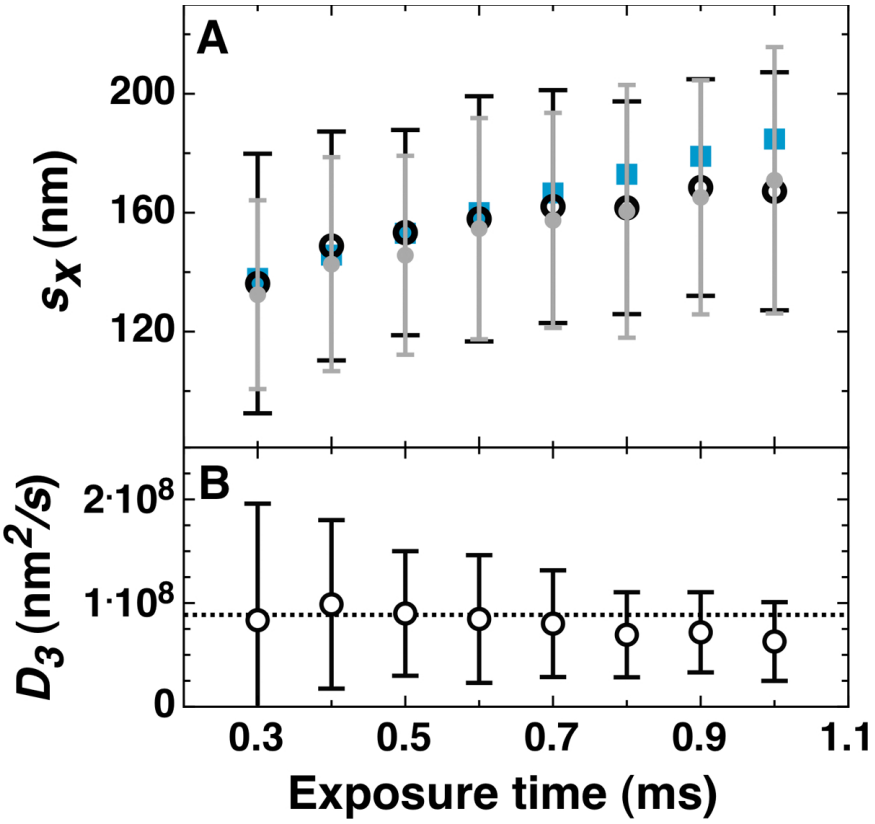

Figure 4.3: Comparing s_x and D_3 results. (A) Experimental (circles), simulation (disks), and theoretical calculation (squares) measurements of diffusing eGFP intensity profiles' mean s_x vs t. In the experimental and simulation results, the error bars are the SDs of the s_x distributions. (B) Experimental D_3 calculated from Eq. 4.3. The error bars are ΔD_3 calculated using Eq. 4.4; the dashed line is the FCS-determined eGFP D_3 of 8.86 $\times 10^7$ nm^2/s for comparison.

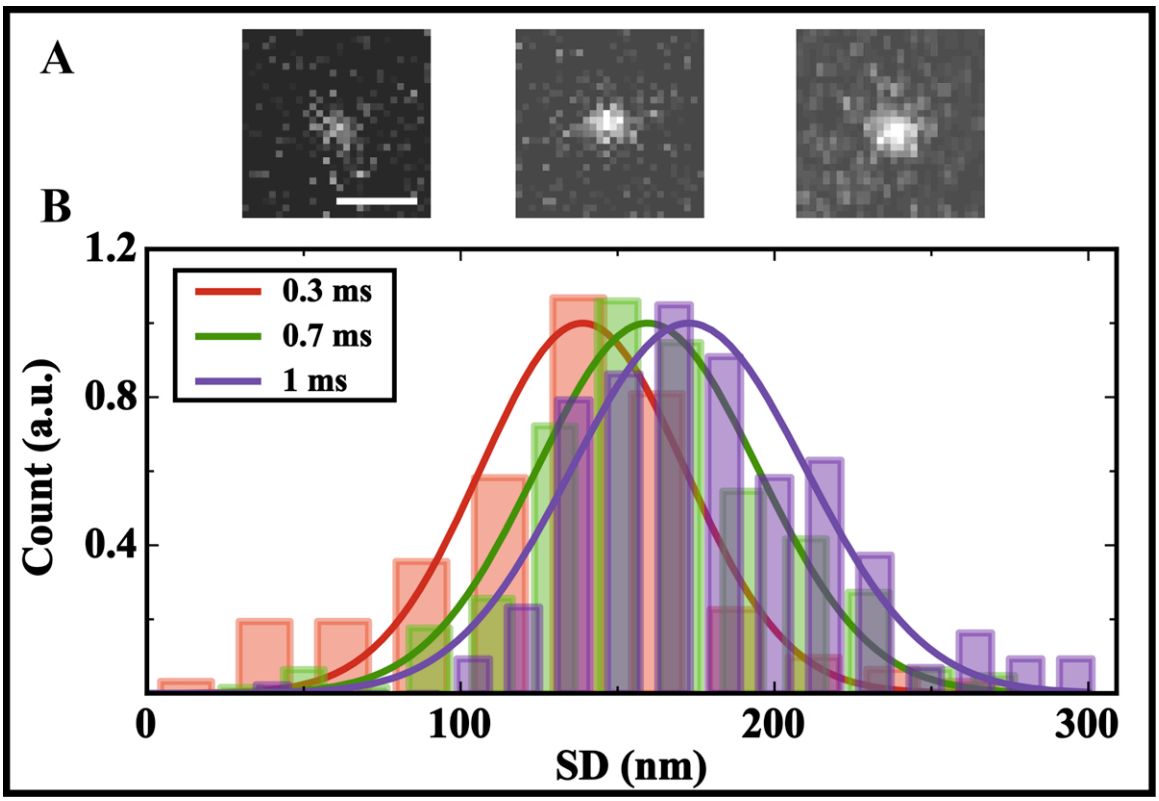

Figure 4.4: Diffusing eGFP images and intensity profile SD distributions at different exposure times. (A) Three representative images showing diffusing eGFP molecules at exposure times of 0.3, 0.7, and 1 ms. The intensity profile SD values increase with the exposure time. The scale bar is 1 μm. (B) EGFP intensity profile SD distributions (normalized by counts for comparison) at the three aforementioned exposure times, showing increasing values of 136.8 $\pm$ 27.7 (mean $\pm$ SD), 159.0 $\pm$ 32.24, and 172.1 $\pm$ 34.8 nm, respectively.

images. The increasing mean eGFP SD values with exposure time are plotted in Fig. 4.3A, where the error bars are the SDs of the eGFP intensity profile SD distributions in Fig. 4.4B.

In analytical calculations, we deduce an expression relating a diffusing eGFP's SD to D_3. The study involves first projecting the eGFP PSFs at all focal depth onto a 2D imaging screen, forming an axial-direction-projected PSF $f(x, y)$, and then convolving this projected PSF with the lateral location distribution of the molecule in a trajectory, which we define as a pathway distribution function (PWDF$_{x,y}$ for the lateral directions) $g(x, y)$:

$$I(x, y) \propto f(x, y) * g(x, y). \tag{4.1}$$

In SOM we show that both $f(x, y)$ and $g(x, y)$ can be approximated well by Gaussian function for sufficiently low exposure times, and their convolution is another Gaussian function with a variance equal to the sum of the two variances. Therefore, the final projected intensity profile of a 3D diffusing molecule is a Gaussian function with SD being

$$s_{x,y} = \sqrt{s_0'^2 + A_{x,y} \cdot 2D_3 t}, \tag{4.2}$$

where $s_0'(t) = \sqrt{111^2 + 0.0634 D_3 t} \approx \sqrt{s_0^2 + 0.0634 D_3 t}$ nm is the SD of the axial-direction-projected PSFs for our experimental parameters, and $A_{x,y} \cdot 2D_3 t$ is the variance of PWDF$_{x,y}$s with $A_{x,y} = 0.0926$. This relation enables the determination

of D_3 from the SD of a single-molecule's intensity profile and the exposure time as

$$D_3 = \frac{{s_{x,y}}^2 - s_0^2}{(2A_{x,y} + 0.0634)t}. \tag{4.3}$$

Using FCS-determined eGFP $D_3 = 8.86 \times 10^7$ nm^2/s in equation A.4, the analytical eGFP s_x results are plotted in Fig. 4.3A, showing excellent agreement with the experimental s_x results within 0.7 ms. Note that s_x starts to deviate from the experimental results at $t > 0.8$ ms; this is because the exposure time begins to approach the diffraction-limit-determined value for eGFP for this study (SOM text).

We have also performed simulations of diffusing eGFP intensity profiles (as shown in Fig. 4.2) using the FCS-determined D_3. Figure 4.3A juxtaposes the simulated diffusing eGFP SD results with the experimental results; the two mean values and error bars agree at all exposure times (A.6 compares the results at $t = 0.6$ ms).

To determine the precision of the measured D_3 from single eGFP images, we performed error propagation analysis of $D_3(s_{x,y})$ using Eq. 4.3:

$$\Delta D_3 = \frac{s_{x,y}}{(A_{x,y} + 0.032)t} \Delta s_{x,y}, \tag{4.4}$$

where $\Delta s_{x,y}$ is the SD measurement precision of the single fluorophore's intensity profile (the experimental error bars in Fig. 4.3A, also Ref. [23]). Figure 4.3B compares the experimentally determined D_3 and ΔD_3 from single diffusing eGFP image SD measurements to the FCS-determined eGFP $D_3 = 8.86$ nm^2/s, showing agreement.

At 0.7 ms, $\Delta D_3 = 5.2 \times 10^7$ nm^2/s for a single eGFP image using both the statistically independent mean s_x and s_y values of $\langle s_{x,y} \rangle = 162.1$ nm and $\Delta s_{x,y} = 39.2$ nm. It is 57% of the eGFP D_3 value of 8.86×10^7 nm^2/s. Since there are order 30 molecules in a typical frame image of less than 1 ms exposure time, the precision to D_3 measurement further improves by $\sqrt{30}$ times to 10%, comparable to the precision of FCS D_3 measurements [4]. In spatially restrictive situations, such as *in vivo* imaging in typically micron-sized cells, where only one image can be obtained at a time, repeated single-image measurements will enable precise D_3 determination.

4.5 Discussion

Although this study focuses on fast diffusion of nanometer-sized proteins in free solution with $D_3 > 5 \times 10^7$ nm^2/s, the methodology applies to 3D diffusion of all rates. When diffusion coefficients are low for large particles, in a crowded environment, or in viscous solvents (such as in cells [59] or glycerol), the molecule's intensity profile will be more localized. Consequently, longer exposure times should be used to observe noticeable changes to the SD from the stationary values. SOM text explains the procedure in determining the appropriate exposure times for a particle of unknown D_3.

Molecules' movement can deviate from a 3D unbiased Brownian motion, examples include directional motion and diffusion with drift. For these alternative motions, s_0' and PWDF$_{x,y,z}$ should be determined before convolving the axial-direction-projected

PSF with $\text{PWDF}_{x,y}$ for the final intensity profile. As long as the mean numerical SD of locations in the molecule's trajectory is less than half of the diffraction limit at the exposure time, the projected convolved image of the molecule will be a unimodal intensity profile that can be fitted to a Gaussian function, and the resulting $s_{x,y}$ will provide information on the molecule's dynamics.

4.6 Summary

In summary, we present a new single-molecule fluorescence image analysis method that measures fast diffusion coefficients with high precision. The experimental setup and data analysis are simple while using standard microscopy imaging systems, and the method is applicable to a wide range of diffusion coefficient measurements with greatly improved temporal resolution. Applications in basic research and pharmaceutical investigations such as fast drug screening can be envisioned.

Chapter 5

Single-Molecule Dynamic Studies of the Membrane Synthesis Protein UgtP on the *Bacillus subtilis* Bacteria Cell Membrane

5.1 Preface

This project was performed as a collaboration between the Levin Lab in the biology department of Washington University in St. Louis and our lab. In September 2010 Levin Lab (Jenny Chien) showed an interest in acquiring some single molecule data and analysis to verify a parameter in their 2007 Cell magazine publication. After having verified the parameters, our lab was still interested in going further by look-

ing into the dynamics of the proteins inside the cells. In doing so we discovered an intriguing characteristic of the proteins, namely a *helical* pathway for the diffusion of these particular proteins inside the cells. For analysis of the data I wrote a Matlab program from which preliminary results were extracted. Perhaps further data acquisition and fine tuning of the Matlab program is needed. This work is intended for eventual publication.

5.2 Abstract

Using novel single molecule fluorescence image analysis methods, i.e. single image molecular analysis (SIMA) [23] and integrated photon molecular counting (IPMC) [39], we studied the behavior of UgtP protein in live *Bacillus subtilis* bacteria cells, in which a diffusing population and a stationary population were detected. UgtP is the protein that coordinates cell division with carbon (nutrient) availability [60]. We observed randomly distributed specific binding sites where the stationary UgtP oligomerize with a mean of 8 UgtP per oligomer, and nonspecific membrane binding events in which the diffusing UgtP population exhibits diffusion along a helical pathway on the cell membrane with a diffusion coefficient of 5.5×10^4 nm^2/s. To our knowledge, most of the previously published work about a helical diffusion pathway has involved the cytoskeletal protein class. Also, this study established a link between the *in vivo* and *in vitro* studies of the UgtP oligomerization in carbon poor conditions.

5.3 Introduction

The *in vivo* diffusive properties of proteins are of general interest for understanding a variety of processes in the bacterial cell. The rate of protein diffusion in bacteria may constrain a variety of cellular functions and limit the rates of many reactions *in vivo*. The membranes of bacteria contain proteins that are important in cellular processes and functions like signaling, cell division, etc. For this reason the value

of their diffusion coefficient becomes important due to its effect on interaction with each other and other proteins. In our study, we used quantitative imaging of single molecule fluorescence to assess the dynamics of UgtP fused to yellow fluorescent protein (YFP).

UgtP is an enzyme inside the bacteria cell *B. subtilis* that coordinates cell division with carbon availability. It is also a membrane synthesis protein. Our single molecule fluorescence technique allowed us to observe the stationary YFP-UgtP population and track the diffusing population. In our study we extracted the diffusion coefficient of diffusing YFP-UgtP and detected a helical diffusion pathway for these molecules. So far there have been several studies of the diffusion coefficient of cytoplasmic proteins [61] and membrane proteins [62]. Our observation of the helical diffusion pathway of UgtP, a membrane-associated protein [63], was a particularly interesting observation since it was a membrane synthesis enzyme for which such helical diffusion pathway was detected. A helical diffusion pathway has been observed for proteins inside the bacteria cells in other studies; however, all of those proteins belong to the class of cytoskeletal proteins [64]. Discovery of the helical diffusion pathway inside the bacteria cell began with the work of Jones et al. in 2001 who found bacterial actin homologs in *B. subtilis* cells are organized into extended helical structures that play key roles in cell shape regulation [65]. The bacteria cytoskeletal proteins that have been found to exhibit helical diffusion pathways include MreB (an actin homolog that contributes to cell shape) [66, 67], ParM (an actin homolog that partitions plasmid DNA) [68], FtsZ (a tubulin homolog that locates the mid-cell and division site) [69,

70, 71], Crescentin (intermediate filament protein homolog) [64], and the MinD and ParA class of bacterial cytoskeletal proteins [72]. However, we have observed that membrane-bound protein UgtP possesses a helical diffusion pathway. As emphasized, UgtP has an important role in coordinating the *B. subtilis* size with carbon availability [60]. Weart et al. have shown that in high carbon availability UgtP inhibits the cell division assembly FtsZ. In poor carbon availability, UgtP forms oligomers and localizes in numerous puncta inside the cell. Background review of this role of UgtP is presented in below, and additional information is presented in an appendix section.

5.4 Background Review: Role of UgtP inside *B. subtilis* Bacteria

Assembly of the highly conserved cytoskeletal protein FtsZ into a ring structure at the nascent division site is the first step in bacterial cell division. Weart et al. [60] have shown that in the soil bacterium *B. subtilis*, the UDP-glucose binding protein UgtP plays a central role in coordinating the cell size with the growth rate, by inhibiting FtsZ and increasing cell size during growth in a carbon rich medium. Previous studies indicate that UgtP activity is controlled via UDP-glucose dependent changes in localization. Under carbon rich/high UDP-glucose conditions, UgtP is distributed throughout the cell and concentrates at the FtsZ ring where it delays division until cells reach the appropriate size. Conversely, under carbon poor/low UDP glucose conditions, UgtP is sequestered away from FtsZ in small, punctate foci. This is shown

as a cartoon in Figure 5.1.

5.5 *In Vivo* Imaging Materials and Methods

5.5.1 YFP as the Label for *in vivo* Single Molecule Imaging

For studying the dynamics of UgtP, in our experiments UgtP was fused to yellow fluorescent protein (YFP) inside the cells. Yellow fluorescent protein YFP, which is a GFP variant, is usually used for labeling in *in vivo* cell imaging studies. YFP has a high quantum yield, is relatively photostable when compared with other fluorescent proteins. It is monomeric, and its optimal excitation is at a longer wavelength than enhanced GFP, thus reducing fluorescence [73]. Limitations of YFP as a label in single molecule experiments include blinking, a higher quantum yield of photobleaching, and a lower overall brightness than many organic dye fluorophores. Overall, YFP has proved sufficiently robust for single molecule diffusion measurements.

5.5.2 Imaging Method of YFP-UgtP *In Vivo*

We acquired the fluorescence images of YFP-UgtP (N-terminally tagged) inside the cells at fixed time intervals of 30 ms while the *B. subtilis* cells were still in the exponential growth phase between 0.3 - 0.8 optical density at 600 nm wavelength (OD_{600}). To be consistent with the previous study of UgtP inside the B. Subtili cell [60], the samples were imaged at $OD_{600} \sim 0.6$. The images showed the expected bright spots that would correspond to YFP-UgtP proteins inside the cells. These bright spots rep-

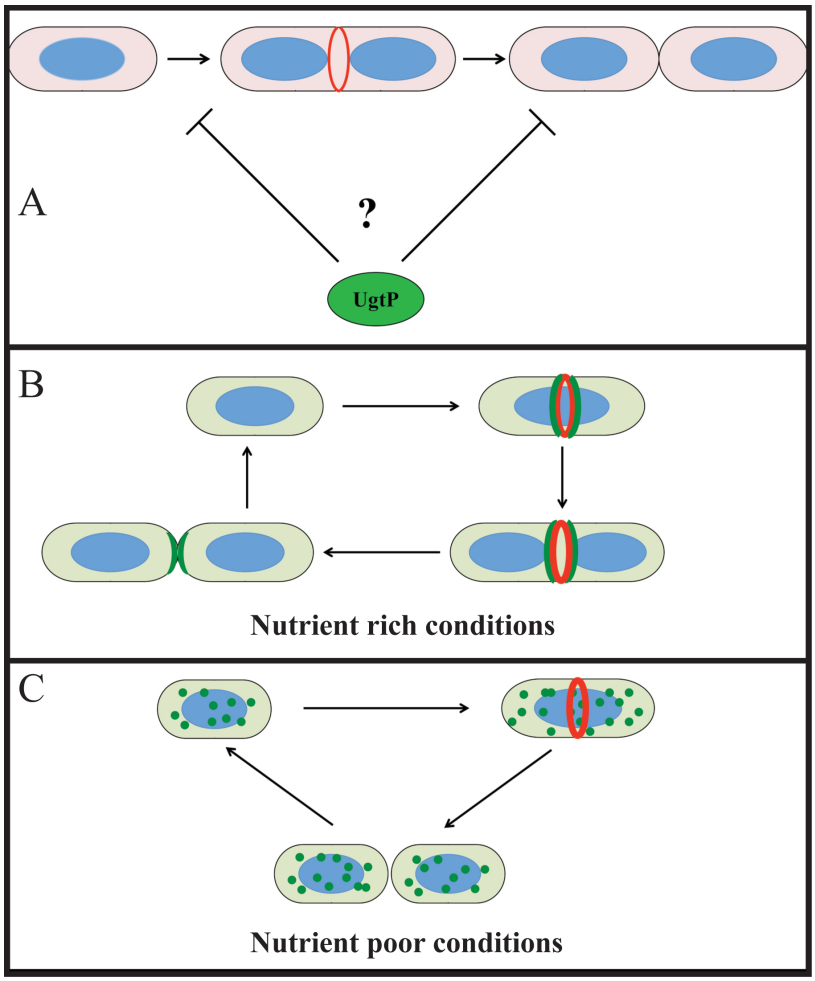

Figure 5.1: This cartoon has been adapted from Weart et al. publication. (A) the red ring in the middle of the cell is the FtsZ assembly. This assembly is also known as the Z-ring. The Z-ring forms in the middle of the cell and locates the cell division septum. A cell divides into two daughter cells from this site. the role of UgtP is that it binds to the Z-ring in a proper UgtP:FtsZ ratio. By inhibiting the Z-ring, UgtP delays the cell division until it grows from a short cell to an appropriate length before it divides. Therefore, this cartoon shows show UgtP controls cell division. (B) The role of UgtP in controlling the cell division at carbon rich conditions is shown in here. During growing in high carbon, a number of UgtP (green ring) bind to the Z-ring (red ring) to delay the division until the cell reaches a certain length. (C) The role of UgtP in controlling the cell division at carbon poor conditions is shown in here. In the lack of enough nutrition, UgtP does not bind to the Z-ring, and forms oligomers that randomly localize in the cell in the form of puncta or foci. These puncta are shown as green dots in the cartoon.

resented the diffusing and stationary YFP-UgtP inside the cells in carbon poor and carbon rich conditions. We also acquired a DIC (differential interference contrast) image of each cell (Figure 5.2) to determine the cell's shape and position in comparison to its fluorescence image. By using a combination of optimized filters and EMCCD camera along with the correct laser excitation intensity we were able to detect the fluorescence from the single and oligomeric UgtP proteins in the cells. In general, single molecule fluorescence experiments inside live bacteria are limited by cellular autofluorescence that can obscure the desired signal. For this reason, a control experiment for gaining the optimum laser excitation power was conducted with the goal of achieving minimum cellular autofluorescence and no induction of autofluorescent protein inside the null cells. Figure 5.2B shows cellular autofluorescence. We found out that for our imaging parameters, the 0.1 kW/cm^2 laser excitation intensity would yield the lowest cell background autofluorescent at 488 nm illumination. Illuminations with total photon energies similar to those used in our experiments have been shown to be nontoxic to bacteria cells containing GFP [61]. Therefore we believe the cells we imaged remained viable throughout the experiment.

5.5.3 Experimental Procedures

The *B. subtilis* strains used in these experiments were provided by the Levin Lab in the Biology Department of Washington University in St. Louis. The cell growth procedure is described in the Appendices section of this thesis. All the cells were cultured in the LB media. The single molecule fluorescence microscopy was performed

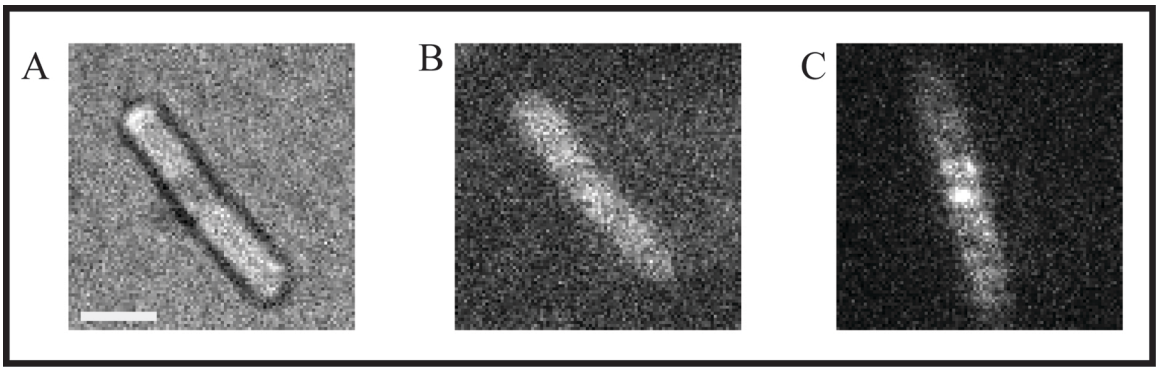

Figure 5.2: (A) DIC image of a *B. subtilis* cell. The scale bar represents 2 μm. (B) The cellular autofluorescence from a wild-type *B. subtilis* cell with no expression of YFP-UgtP. (C) A cell with YFP-UgtP expression which looks like bright diffraction limited spots inside the cell. These spots representing the YFP-UgtP show intensities above the cellular autofluorescence.

using a Nikon TE2000-S microscope in conjugation with a Nikon oil immersion 100 X objective (Numerical Aperture 1.49) and a EMCCD Andor iXon camera. All the images were taken by on a 512 $\times$ 512 pixel camera chip. Images were analyzed using the open-access NIH software ImageJ. Live cell samples were prepared for imaging as described in the Appendices section of this thesis.

5.6 Results and Discussion

The fluorescence imaging of YFP-UgtP yielded the observation and quantification of two categories of UgtP inside the *B. subtilis* cells. We observed a category of diffusing UgtP which seemed to mainly diffuse on a helical pathway along a straight line with fluctuations about the straight line yielding a 1D diffusion that appeared to be Brownian diffusion from the single particle MSD analysis. We also observed an stationary UgtP population that formed oligomers that localized as sequestered

puncta inside the carbon poor cells in a random pattern. The details of the analysis are discussed in the following subsections.

5.6.1 *In Vitro* Imaging and Life-time Analysis of Single YFP

Before quantifying the dynamics of YFP-UgtP *in vivo*, a study of the fluorescence characteristics of single YFP molecules attached to fused silica surface, including their average photon lifetime, was essential in validating the identification of YFP-UgtP proteins inside the cell. We imaged a dilute solution of YFP proteins at 1nM concentration immobilized on the oxygen plasma cleaned hydrophilic fused-silica surfaces. At our excitation intensity of 0.1 kW/cm^2, exposure time of 30 ms, and synchronized imaging frequency of 33 HZ, the mean number of collected photons before a YFP photobleached was 3863 $\pm$ 2339, as shown in Figure 5.3, which corresponds to 1.11 ± 0.41 s or about 36 frames (30 ms per frame). This is the instrumental limit to the maximum mean distance we could observe a single YFP-UgtP diffuse along the cell. No oxygen scavenging solution for lengthening the photon lifetime was used in imaging our YFP proteins. Single YFP molecules could be easily identified because according to their bleaching characteristic they exhibit a sudden disappearance in one frame rather than gradually fading out over several frames.

Also, a single immobile YFP molecule appeared to have a symmetrical intensity profile with a mean standard deviation (SD) of 110 ± 8 nm when fit to a Gaussian function, as shown in Figure 5.4. This control determines the expected fluorescence intensity of a single EYFP under our imaging setup. Since we did not use a gel

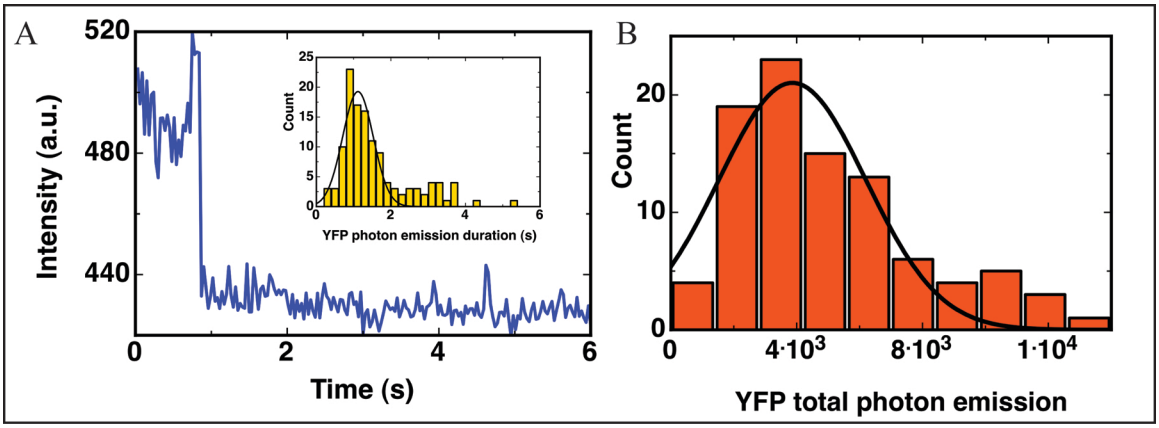

Figure 5.3: Photon lifetime properties of YFP monomers (A) The fluorescence time trace of a YFP monomer. This fluorescence time trace shows a single step photobleaching time trace, representing a monomeric time trace. The inset figure shows a mean total photon emission duration of 1.1 ± 0.4 before the monomers photobleach. (B) The distribution of 100 monomer YFPs shows a typical monomer emitted 3863 ± 2339 photons before it photobleached.

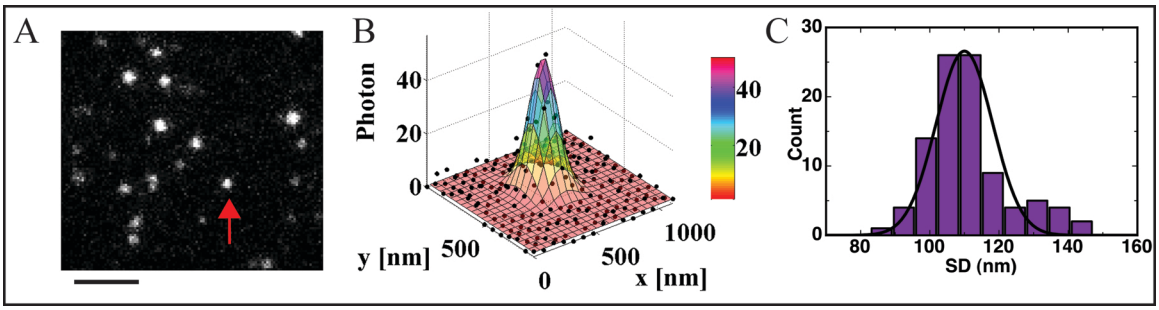

Figure 5.4: The YFP molecules' intensity profile were fit to a Gaussian function. (A) EMCCD camera image of a few immobilized YFPs on a fused-silica surface obtained by TIRF microscopy. The scale bar represents 5 μm. (B) The intensity profile (black dots) and the Gaussian fit to the intensity profile of the single YFP molecule indicated by the red arrow in (A). (C) The distribution of the standard deviation (SD) of the Gaussian profile of 100 YFP molecules, which shows a mean of 110 nm.

pad for our cell immobilization (immobilizing the cells on a hydrophobic fused-silica), our method of calibrating the fluorescence intensity of single YFP immobilized on fused-silica should give an appropriate representation of the YFP-UgtP fluorescence characteristics inside the cells.

5.6.2 Diffusing Protein Population: Tracking and Image Analysis Methods for Diffusing YFP-UgtP Molecules in Cells

In every image, each YFP-UgtP molecule was tracked in a 10 $\times$ 10 pixel box (790 $\times$ 790 nm^2 area) in order to include both the diffraction limited spot and enough background space for fitting its intensity profile to a Gaussian function . The center pixel of each molecule was recorded for each image until the molecule could no longer be tracked, either due to photobleaching, diffusing away, or going beyond our imaging depth. Most of the molecules at the vicinity of the poles of the cells ($\sim$ 790 nm away from the edges of the cell poles) were not chosen for the diffusion analysis. In most cases it was difficult to box the molecule at the poles with enough background area to permit good fits.

To study the diffusion of the molecules on short time scales we chose a 30 ms exposure time, with zero dead time between each frame, which yielded 33 MHz imaging. This frequency was the imaging rate limit of our EMCCD camera for 512 $\times$ 512 pixel imaging area. If we had chosen a smaller imaging area we could have gone to higher imaging speeds of up to 100 frames per second, but in order to detect and

image the maximum number of cells per frame we chose the 512 $\times$ 512 imaging area. At the calibrated 0.1 kW/cm^2 laser intensity, the exposure time of 30 ms per frame provided us with the minimum SNR for molecule detection without perturbing the cell environment with high laser intensity.

The *B. subtilis* cells are cylindrical, usually 5-6 μm in length and 1 μm in diameter. This means that the width of the cell is about 4 times the width of the diffraction limit ($\approx$ 250 nm). In practice, in the first few frames of a movie the YFP-UgtPs are too many and too bright (cells were induced to express the maximum number of YFP-UgtP). However, due to photobleaching of the molecules inside the cells in the next frames, the population of the emitting molecules decreased, and identification of well isolated YFP-UgtP molecules became easier. Most of the molecules in this analysis were chosen from this category, so the molecules were well isolated from each other.

For the molecules we picked for analysis, an average trajectory before disappearance was 12 frames, corresponding to 360 ms. This was well below the 1 s average for the lifetime of a single YFP. From the many trajectories that we recorded, we analyzed 15. These 15 molecules were chosen such that they had trajectories consisting of at least $N = 6$ frames, so as to provide meaningful statistics. We used these 15 trajectories to calculate the true MSD of single YFP-UgtP trajectories for time intervals of 30 ms in accordance with the single particle trajectory analysis method developed by Qian et al. [54]. A geometrical correction was considered in the analysis of the diffusion, which is explained below. For a better study, a larger number of diffusion

trajectories should be analyzed, a point addressed in the Future Directions section.

5.6.3 Geometrical Correction for the Image Analysis of diffusing YFP-UgtP on the Cell Membrane

In order to analyze the images of the diffusing molecules on the cell membrane a geometrical correction was considered. Our geometrical correction took into account the relation between the observed displacement of the molecule recorded on a 2D EMCCD camera image plane (planar displacement) and the displacement of the molecule on the cylindrical membrane of the cell (true displacement). The"planar" displacement basically refers to the diffusion of the molecules as they appear on the 2D EMCCD camera image plane, even though the"true" displacement is on the cylindrical cell membrane. To calculate the true displacement of the molecules on the cell membrane surface corresponding to the measured values on the planar surface, the *B. subtilis* cell was considered a cylinder with a radius of 500 nm, and varying length for different cells. The long axis of the cylinder lies in the image plane as shown in Figure 5.5; therefore, the actual distance moved by the molecule on the cell surface is larger than the measured displacement on the image plane. The planar positions x and y were recorded at time intervals of Δt, then converted to the positions corresponding to the curved cell surface $x\prime$, $y\prime$ and $z\prime$ as following

$$x' = x,\ y' = y,\ z' = R - \sqrt{R^2 - x^2}, \tag{5.1}$$

These $x\prime$, $y\prime$ and $z\prime$ positions on the curved cylindrical surface were then converted to the flat cell surface (expanded cylinder) with coordinates of $x\prime\prime$, $y\prime\prime$ and $z\prime\prime$ so that the calculations were still on a flat 2D surface instead of a cylindrical surface [not shown in5.5].

$$x'' = R \times \theta = R \arctan \frac{x}{\sqrt{R^2 - x^2}},\ y'' = y,\ z'' = 0 \tag{5.2}$$

After this coordinate system conversion, another aspect of the diffusion was taken into consideration. Since most of the diffusing molecules seemed to move along a rather straight line, we identified this line and picked it as the direction of the diffusion (called X in our calculations) and a perpendicular axis to X (called Y). The relationship between the ($x\prime\prime$, $y\prime\prime$) coordinate system and the (X, Y) coordinate system is described as

$$X = x\prime\prime \cos\theta + y\prime\prime \sin\theta,\ Y = -x\prime\prime \sin\theta + y\prime\prime \cos\theta, \tag{5.3}$$

Now the actual or "true" displacement comes from the (X, Y) coordinate system. The MSD calculated from this actual distance of the expanded cell wall is referred to as the "true MSD" and the calculated diffusion coefficients correspond to the "true MSD". As expected, our images verified that the molecules were the brightest when they were closer to the middle of the cell (long axis of the cell) and not as bright when farther from the middle of the cell. This is because the cell is attached to the fused-silica surface mainly from its middle and as the distance from the long axis of

Figure 5.5: This cartoon shows how the geometrical corrections are taken into consideration. The cell is considered to be a cylinder (represented by the yellow surface). When a molecule diffuses on the cell membrane surface it is actually displacing on cylinder walls. However the EMCCD camera captures this event on a 2D surface (represented by the flat gray surface). The displacements on the EMCCD image place are referred to as"planar" displacement, and they do not represent the true displacement. The"true displacements" are calculated from the displacements on the expanded cell surface (image the yellow surface laid flat to become a 2D surface).

the cell increases the molecule appears to be relatively less bright.

5.6.4 Diffusion Coefficient of YFP-UgtP Inside the Cells

An image sequence of a YFP-UgtP diffusion on the cell membrane is shown in Figure 5.6. This sequence shows the molecule from when it appeared on the cell surface to the time it disappeared, a total of 330 ms for all of the 11 images. This figure shows 1 out of the 15 diffusion trajectories that were analyzed for the net displacement study. Figure 5.6 shows the temporal average image of this diffusion.

The diffusion coefficient measurement analysis comes from the method of single particle trajectory analysis that was developed by Qian *et. al.* for the diffusion of a single Brownian particle [54]. This method calculates the $MSD_{(n,N)}$ for all available time intervals of a single diffusion trajectory

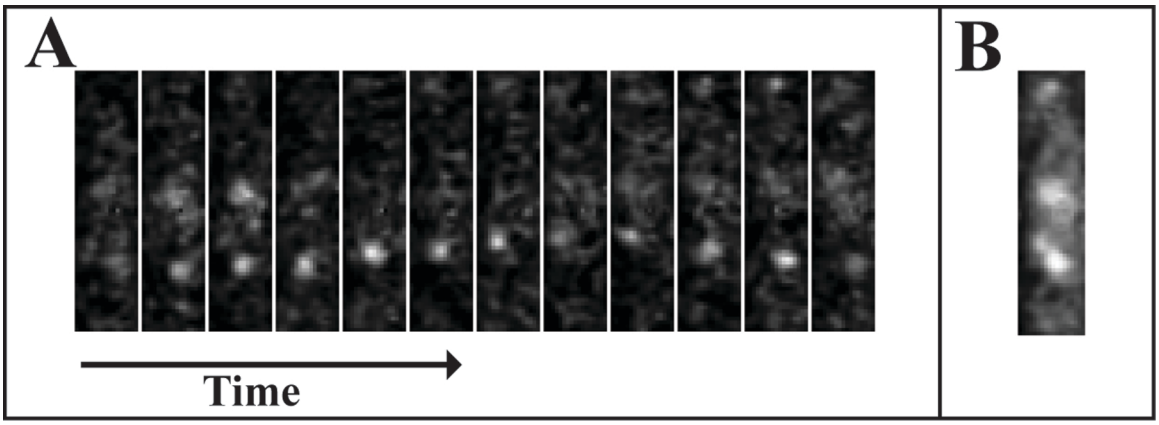

Figure 5.6: (A) A representative example of diffusing YFP-UgtP on the cell membrane. The figure shows how the molecule moves on the cell membrane as a function of time. This trajectory lasts 11 frames which is a total of 330 ms. (B)Time average of the consecutive frames in (A) which is a total of 300 ms.

$$MSD_{(n,N)} = \frac{\sum_{i=1}^{N-n}(x_{i+n} - x_i)^2}{N-n} = 2D_1 n\Delta t + 2\sigma_s^2 \tag{5.4}$$

In this equation N is the total number of measured positions, n is the measurements index going from 1 to N, Δt is the time interval between two consecutive position measurements, and σ_s is the measurement accuracy associated with each x_i. By taking the fractional $MSD_{(n,N)}$ uncertainty at different n into account, we can obtain the diffusion coefficient D of a single trajectory. This fractional uncertainty comes from $\sigma_{n,N}/2D_2 n\Delta t$ at every time interval n, where $\sigma_{n,N}^2$ is the variance in the MSD,

$$\sigma_{(n,N)}^2 = \frac{(2D_1 n\Delta t)^2(2n^2+1)}{3n(N-n+1)} \tag{5.5}$$

A trajectory that consists of N steps has $n = 1$ to $N-1$ time intervals. For example, to calculate the true MSD for time interval of $n = 3$ we used positions

belonging to frame 1 and 4, or 2 and 5, or 3 and 6, etc. As the number of time intervals increases the number of available $MSD_{n,N}$ decreases yielding an increase in the variance of $MSD_{(n,N)}$. Therefore we can define a cutoff for n called n_c, and calculate the diffusion coefficient D from fitting the $MSD_{(n,N)}$ versus $n < n_c$ only. The value of n_c is determined such that $\sigma_{n,N}/2D_2 n\Delta t$ is 50%. If a single trajectory is Brownian, then its $MSD_{(n,N)}$ below n_c is a linear function of t. In order to have an adequate number of data points for MSD to fit to n, the trajectory should be at least 10 steps long ($N > 10$), which yields $n_c = 3$ and gives a fractional variance $< 50\%$.

For a particle undergoing Brownian diffusion, the true MSD is a linear function of time lag. However, the planar MSD would show a nonlinear dependence on the time lag because the planar displacements do not represent the true displacements. For our data the true MSD, which is corrected for the 3D geometry of the cell, shows a linear relationship with Δt, within the error of our measurements as shown in Figure 5.7.

In this work no trajectory with less than 3 consecutive frames of YFP-UgtP blinking was taken into consideration. Also, the mean precision in the location measurement σ_s^2 is 17.5 nm, which corresponds to $2 \times \sigma_s^2 = 600$ nm, and these photon noise offsets were subtracted in the $MSD_{(n,N)}$ versus n curves.

Figure 5.7 shows the MSD analysis of a single trajectory of YFP-UgtP molecule inside the *B. subtilis* cell for different time intervals of this trajectory. This molecule took N = 35 steps inside the cell for a duration of 1.05 s. The molecule appears to be doing Brownian diffusion with D = 4.14 $\pm$ 2 $\times$ 10^4 nm^2/s inside the cell

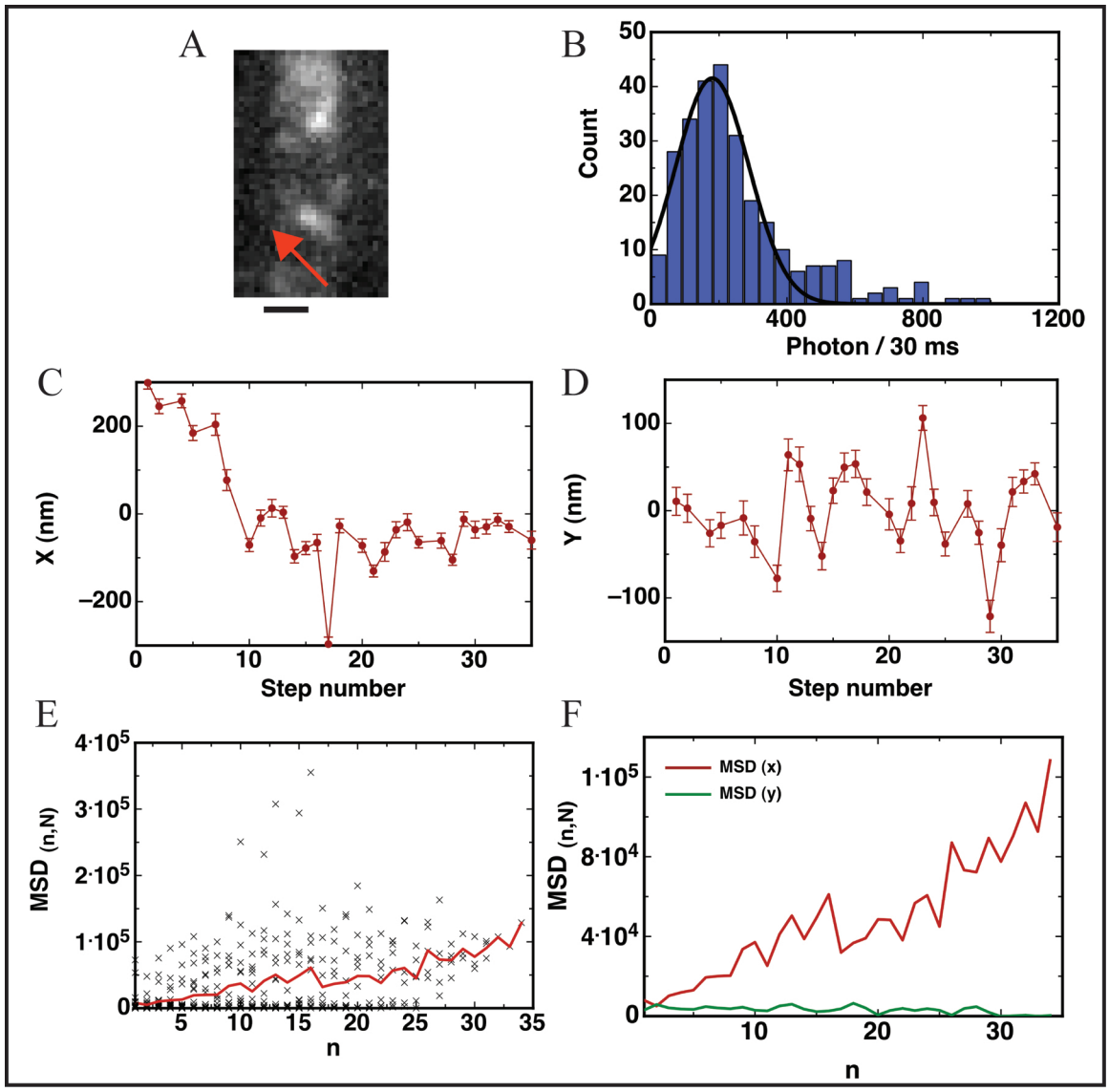

Figure 5.7: A single particle trajectory MSD analysis for a YFP-UgtP diffusing on the B.subtilis membrane. (A) A temporal average of a displacement that consists of 35 steps is shown here. The diffusion trajectory looks like a section of a helical pathway inside the cell. The scale bar represents 500 nm. (B) Distribution of the number of photons emitted from the YFP-UgtP per 30 ms image. This photon emission is used in the calculation of the precision in the mean location of the molecule in each frame. (C) The true displacement along the straight line on which the molecule diffuses (X axis). (D) The true displacement of the molecule on the axis (Y axis) perpendicular to the aforementioned straight diffusion line. (E) The single particle MSD in X is shown here where the diffusion coefficient D = 4.14 $\pm$ 2 $\times$ 10^4 nm^2/s. (F) The comparison of the MSD in X and Y.

along an angled line with respect to the long axis of the cell. Figure 5.8 shows the single particle MSD analysis of 15 trajectories. The $MSD_{(n,N)}$ of these molecules as a function of time interval in a linear scale is shown in Figure 5.8A. Figure 5.8B shows the same data in a log-log scale. The log-log plots show the linearity of the of the MSD in low time interval (n=1 corresponding to $\Delta t = 30$ ms). The intercepts at $n = 1$ are $2D\Delta t$ for each particular walk. The results show that there is a variety of D values even though all the walks are Brownian diffusion. Figure 5.9 shows that the distribution of the 15 D values ranges from 4×10^3 to 10^6 nm^2/s. Also, according to figure 5.9 the distribution of the mean diffusion length for the a molecule before its disappearance is 80 ± 54 nm for consecutive frames (meaning only for $n = 1$).

A UgtP molecule is 43 kDa, and YFP is 27 kDa. The values for the diffusion of YFP-UgtP seem to be much smaller than the D value of 5.6×10^6 nm^2/s expected for a cytoplasmic protein with mass of 70 kDa, as estimated from D for cytoplasmic GFP (27 kDa; $D = 7.7 \times 10^6$ nm^2/s) [67], thus verifying that our results are in agreement with the membrane-bound protein's range of diffusion coefficient values [62, 74].

5.6.5 Observation of a Helical Diffusion Pathway of YFP-UgtP on the Cell Membrane

The YFP-UgtP diffusion pathway inside the *B. subtilis* cells seemed to have a helical or spiral shape in many of our images. This diffusion pathway was identifiable due to the temporal resolution that was selected (millisecond range), and was not detected

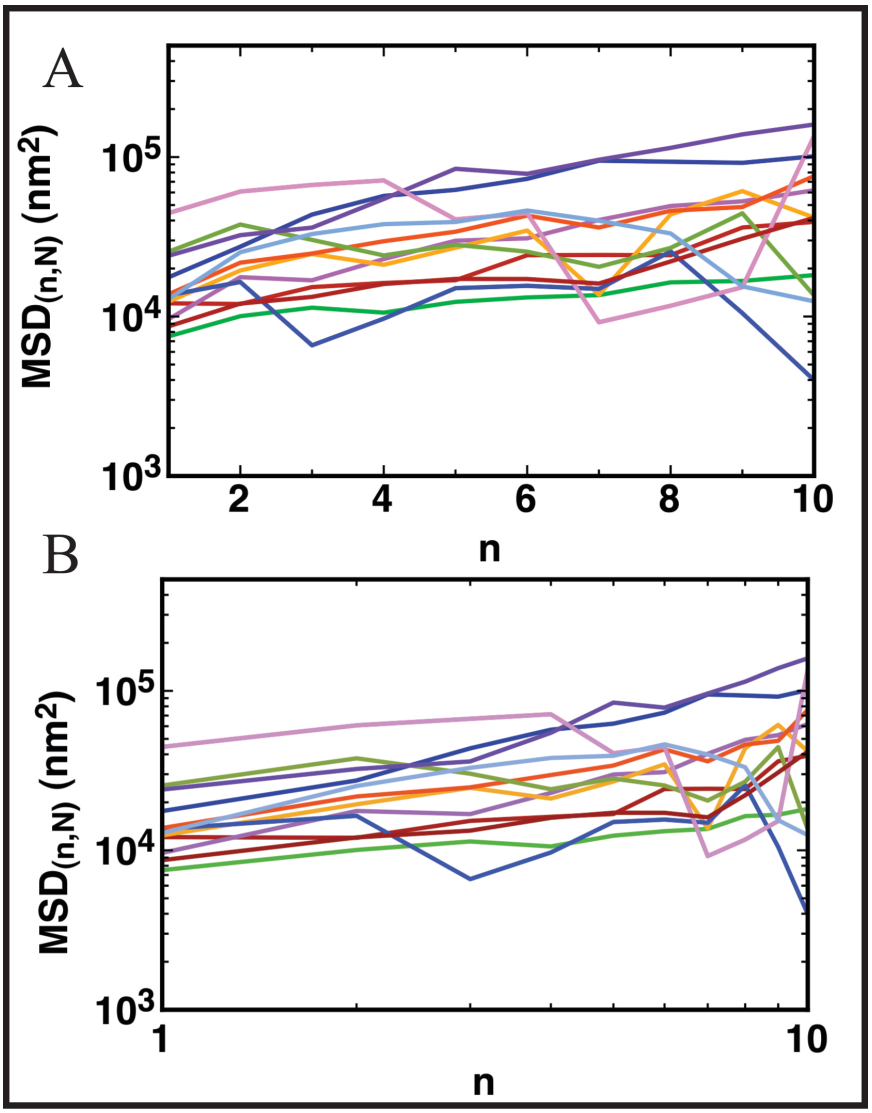

Figure 5.8: Result of the single particle MSD analysis for 15 trajectories of diffusing YFP-UgtP inside the B. subtilis cells

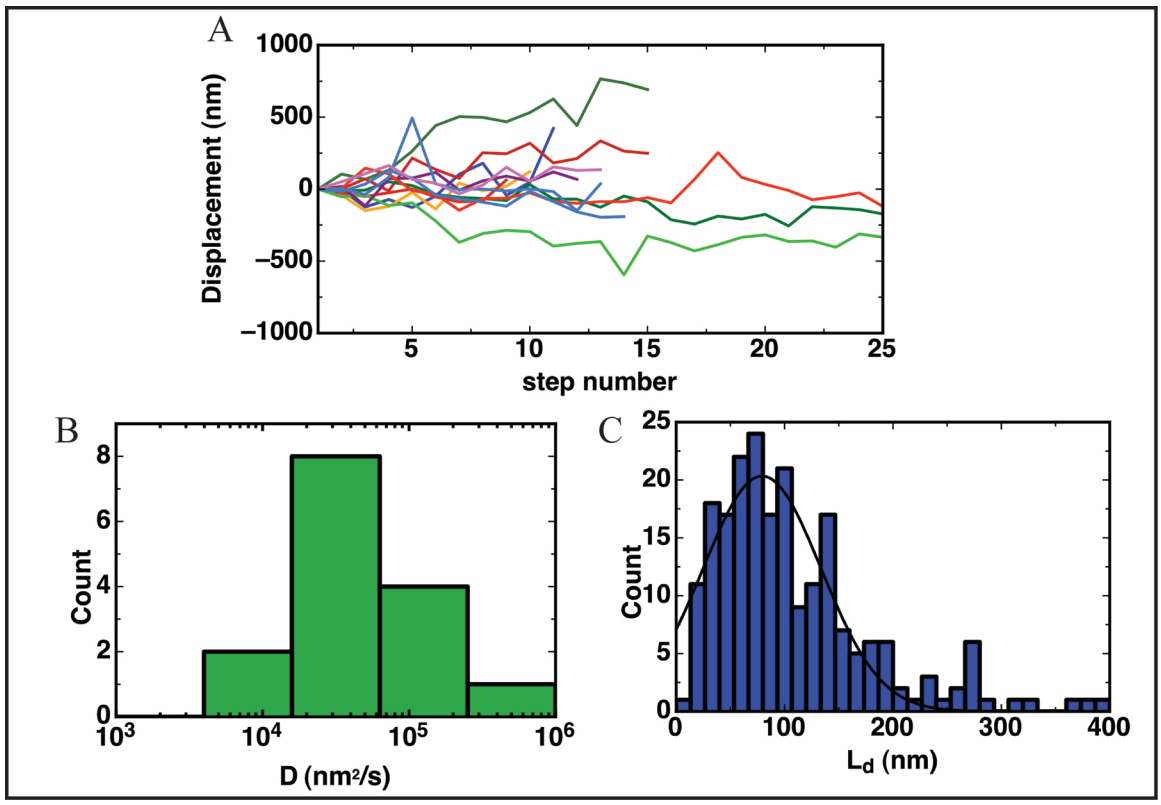

Figure 5.9: (A) Displacement trajectory of the 15 analyzed diffusing molecules. (B) The distribution of the calculated diffusion coefficients of these 15 molecules. (C) The maximum length of diffusion has a mean of 80 ± 54 nm.

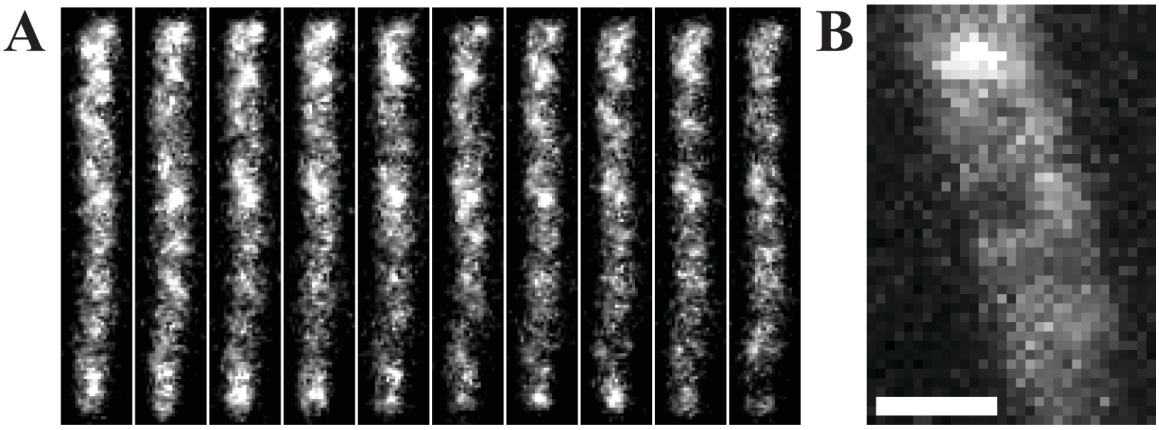

Figure 5.10: (A) 10 consecutive frames of a movie of the diffusion of YFP-UgtP inside the cells. A helical pattern is apparent in each frame. (B) A temporal average image of a diffusion where a two helical pitches are apparent.

in the previous fluorescence imaging of UgtP inside the *B. Subtili* [60]. Figure 5.10.A shows an image of helical pathways under 30 ms exposure time, and Figure 5.10B shows a 3-s time averaged image. So far, helical activity of proteins has been associated with the cytoskeletal proteins in which the cell width and length of the cell are controlled by the helical activity of the protein [65, 69]. A simple interpretation of the UgtP's helical diffusion could lie in its relationship with FtsZ proteins. The diffusion of FtsZ was found to be spatially restricted to helical-shaped regions [69], and since UgtP protein is an inhibitor of FtsZ, the UgtP proteins could be undergoing a nonspecific interaction with FtsZ filaments on the cell membrane. Also, Figure 5.10 shows the helical diffusion pattern of YFP-UgtP inside the cells as time series in A and a time average in B.

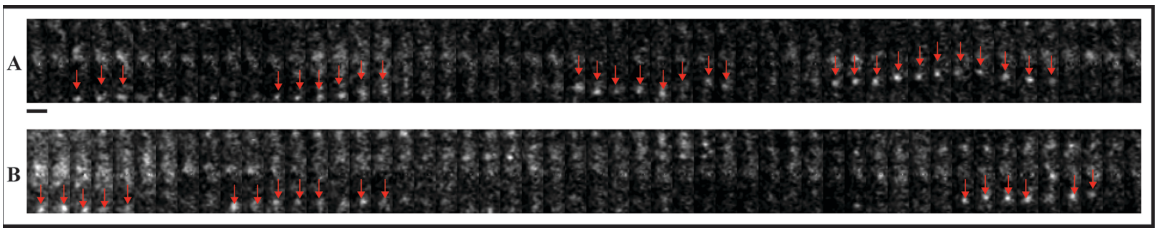

Figure 5.11: Consecutive frames of a movie of YFP-UgtP diffusion on a cell membrane. The red arrows in (A) and (B) show the image frames where the molecules seem to be apparently diffusing on the cell membrane. The molecules seem to be appearing and disappearing in a periodic pattern, with the molecule going beyond our detection and then coming back, as well as moving along the cell.

5.6.6 Stationary Proteins: Localization pattern of YFP-UgtP as a Function of Carbon Availability

The localization pattern of YFP-UgtP was investigated inside two different strains of *B. subtilis*: the 2292 strain which is defective in the pathway required for synthesis of UgtP's substrate UDP-glucose and mimics cells grown under carbon poor conditions, and the 2423 strain which represents glycolipid biosynthesis pathway intact. Also the 522 strain was used as the wild type with null background. Figure 5.12 shows the localization of YFP-UgtP inside both strains of carbon poor and carbon rich cells. Consistent with previous studies [60] we observed that in the carbon rich cells the UgtPs localize at the middle of the cell where the FtsZ forms the Z-ring for locating the division site. Also, this Figure shows that in carbon poor cells UgtP localizes in foci that consists of multiple UgtPs (oligomer). The foci were randomly distributed inside the cells.

A previous study [60] had shown that in *in vitro* conditions UgtP itself forms higher order structures in the absence of FtsZ. These structures appeared to consist

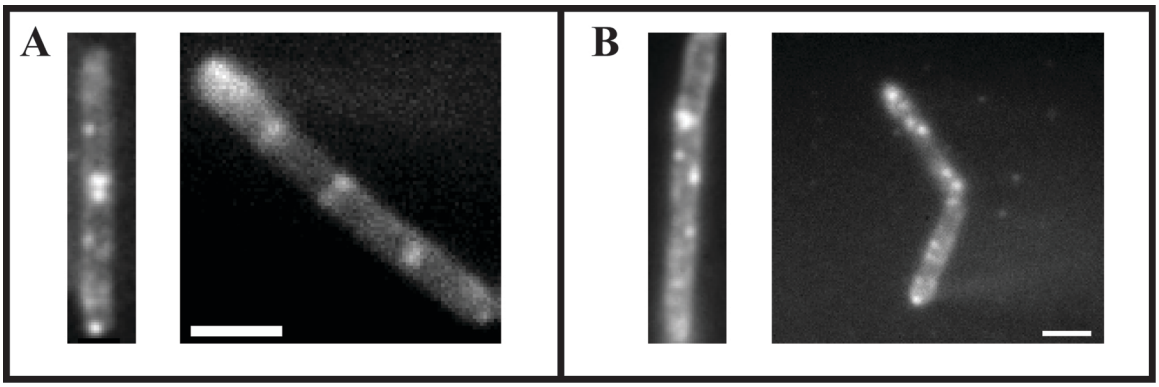

Figure 5.12: (A) Localization of stationary YFP-UgtP oligomers inside the carbon rich *B. subtilis* cells, where they localize to the mid-cell at the Z-ring for delaying cell division. (B) Localization of the stationary YFP-UgtP oligomers in the carbon poor conditions where they sequester in a randomly distributed puncta or foci. The scale bar represents 2 μm.

of closely stacked spirals of UgtP monomers (7 or 8 per turn) [Figure 5.13]. Through our *in vivo* single molecule study we determined the number of oligomers in the foci at carbon poor conditions, therefore establishing a link between the *in vitro* and *in vivo* studies of UgtP oligomerization. This is shown in Figure 5.13. According to our measurements we found that on average there are 8 ± 4 YFP-UgtP in the oligomers, consistent with the *in vitro* results of Weart et al.

5.7 Conclusion

By using fluorescent single molecule methods we observed stationary and diffusing populations of YFP-UgtP inside the *B. subtilis* cells. We tracked the motion of individual diffusing YFP-UgtP molecules for time scales ranging from 30 ms to a few seconds. Although a combination of photobleaching and diffusion of molecules in and out of the focal volume limited observations of molecular motion to 360 ms on

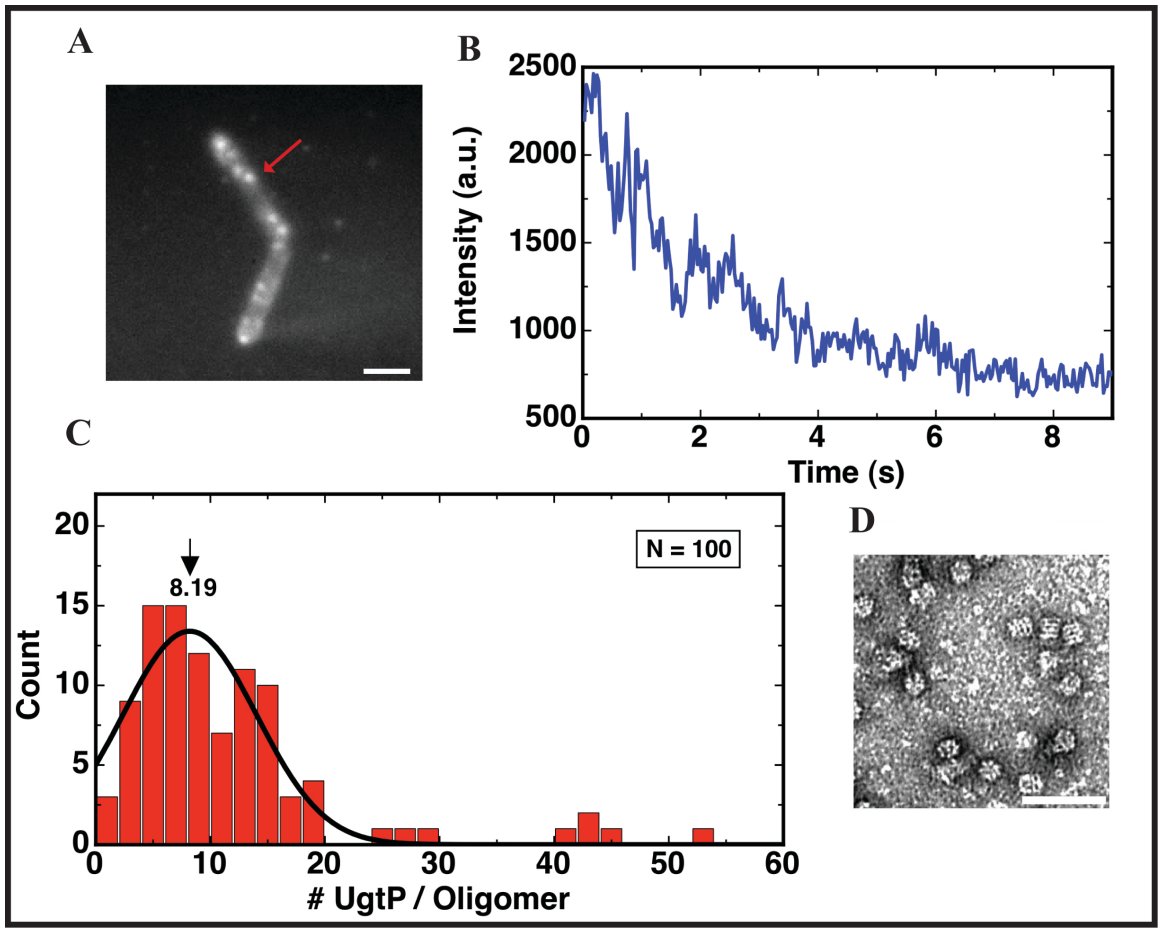

Figure 5.13: (A) stationary UgtP oligomers inside the carbon poor cells. (B) The time trace of these oligomers shows a rapid decrease of fluorescence instead of a sudden disappearance, which indicates the existence of multiple UgtP per oligomer. (C) The number of UgtP per oligomer for a distribution of 100 oligomers yielded results of 8 ± 4 UgtP per stationary oligomer. (D) Electron micrographs of UgtP in the absence of FtsZ. This image was adapted from Weart et al. publication.

average, the D value for YFP-UgtP was extracted. The true MSD of YFP-UgtP was found to be linear with time for the times scales assayed; therefore we conclude that the YFP-UgtP molecules undergo Brownian diffusion inside the *B. subtilis* cells on the timescale of 30 ms. The diffusing molecules in this study showed a 1D Brownian diffusion along a helical trajectory. We cannot exclude the possibility that YFP-UgtP molecules display non-Brownian motion for time scales of less than 30 ms or longer than 600 ms.

5.8 Future Directions

Our studies included the diffusion coefficient measurement in the 2292 strains, which mimc wild type *B. subtilis* cultured under nutrient poor conditions with regard to UgtP dynamics. To infer more information about the nature of UgtP diffusion inside the *B. subtilis* cells, a study of the YFP-UgtP diffusion coefficient distribution in the 2423 strain, which are carbon rich cells, is necessary. Also, it would be interesting to investigate the diffusion coefficient value as a function of position within the cell, for example, to determine whether it is different for molecules closer to the poles or the mid cells. Moreover, increasing the number of analyzed molecules from 15 to a much higher number would help to enhance statistical confidence in our findings.

To illuminate the interaction of UgtP and FtsZ, an experiment can be designed to grow cells that express both UgtP and FtsZ fused to two different fluorophores. In this way, simultaneous imaging of FtsZ and UgtP dynamics inside the same cell

becomes possible, enabling direct observation of the helical pathway of the FtsZ and UgtP diffusion. If these pathways lie exactly on top of each other, one would conclude that they are interacting directly with each other.

Chapter 6

Dissertation Summary and Conclusion

Single molecule imaging permits high resolution measurements of fluorescent emitters in time and space, which makes it a powerful method for studying biological events. This noninvasive, nonperturbative technique is quite useful for the study of single protein molecules in live cells, as well as in solutions. Using total internal reflection fluorescence (TIRF) microscopy, the experiments of this thesis have covered three main subjects. First, single molecule imaging of the mechanisms for protein adsorption onto hydrophobic and hydrophilic fused silica surfaces was performed, and the reversible and irreversible adsorption mechanisms onto hydrophobic fused silica surfaces were detected. Second, experiments involving single-image diffusion coefficient measurements of proteins undergoing Brownian diffusion in solution yielded a simple method for extracting the diffusion coefficient of freely diffusing proteins.

This technique enabled a 100-fold time resolution enhancement compared to current available methods without compromising the localization information of the fluorescent molecules. By measuring the standard deviation of the Gaussian fitted point spread function (PSF) of the mobile molecules, we were able to relate the spot size of the molecules to their 3D diffusion coefficients. This method can be applied to any kind of diffusion once the pathway distribution function for such kind of diffusion is mathematically characterized, therefore generalizing the applicability of this method to the imaging of membrane proteins, plasma proteins, and diffusion of a protein on a specific or nonspecific DNA. Third, by applying the techniques of single molecule imaging to YFP-tagged cell metabolism regulator protein inside a bacteria cell, a stationary population and a diffusing population of UgtP-YFP were observed inside the *Bacillus subtilis* cells. The diffusing proteins were shown to diffuse along a helical diffusion pathway on the cell membrane with diffusion coefficient of $5.5 \times 10^4\ nm^2/s$, consistent with previously measured membrane-bound proteins' diffusion coefficients. This was a particularly interesting observation for a membrane synthesis enzyme. The stationary population showed oligomerization characteristic of an average of 8 proteins per oligomer. These oligomers sequestered in random spots inside the cells.

Appendices

Appendix A

Supporting Material and Text for Chapter 4

Materials and Methods

Sample preparation and imaging

The eGFP molecules (4999-100, BioVision, Mountain View, CA) were diluted in 0.5X TBE buffer (45 mM Tris, 45 mM Boric Acid, 1 mM EDTA, pH 8.0) to 0.03 nM. For the stationary eGFP studies, manufacturer pre-cleaned fused-silica chips (6W675-575 20C, Hoya Corporation USA, San Jose, CA) were used, where isolated eGFP molecules were adsorbed to surfaces at low concentration. For the diffusing eGFP studies, the manufacturer pre-cleaned fused-silica chips were treated using oxygen plasma for three minutes, rendering it hydrophilic to prevent eGFP adsorption [58]. The hydrophilic fused-silica surface can be considered ballistic for the diffusing eGFP molecules in our experiments and simulations. For both studies, a protein solution of

5 μL was sandwiched between the fused-silica surface and an oxygen-plasma-cleaned coverslip (2.2 $\times$ 2.2 cm^2), resulting in a 10.5 μm thick water layer. The coverslip edges were then sealed with nail polish.

Single-molecule imaging was performed using a Nikon Eclipse TE2000-S inverted microscope (Nikon, Melville, NY) in combination with a Nikon 100X objective (Nikon, 1.49 *N.A.*, oil immersion). Samples were excited by prism-type total internal reflection fluorescence (TIRF) microscopy with a linearly polarized 488 nm laser line (I70C-SPECTRUM Argon/Krypton laser, Coherent Inc., Santa Clara, CA) focused on a 40 $\times$ 20 μm^2 region. The 488 nm line was filtered from the multiline laser emission using a polychromatic acousto-optic filters (48062 PCAOM model, NEOS Technologies, Melbourne, FL). The laser excitation was pulsed with illumination interval of 30 ms for the stationary eGFP molecules in 4.1 and Fig. A.3, and between 0.3 ms and 1 ms for the diffusing eGFP molecules. The excitation intensities were 2.7 and 3.2 kW/cm^2 for the respective stationary eGFP molecules, and 37.5 kW/cm^2 for the diffusing molecules. Images were captured by an iXon back-illuminated electron multiplying charge coupled device (EMCCD) camera (DV897ECS-BV, Andor Technology, Belfast, Northern Ireland). An additional 2X expansion lens was placed before the EMCCD, producing a pixel size of 79 nm. The excitation filter was 488 nm/10 nm, and the emission filter was 525 nm/50 nm.

Data acquisition and selection

Movies were obtained by synchronizing the onset of camera exposure with laser illumination for different intervals. The maximum gain level of the camera was used and

the data acquisition rate was 1 MHz pixels/sec ($\approx$ 3.3 frames/sec). Single-molecule images were checked such that there were no saturations in the intensity profiles. For the defocusing analysis of stationary eGFP molecules, 21 $\times$ 21 pixel boxes centered at the molecule were selected by hand using ImageJ (NIH, Bethesda, MD), and the intensity values were used for the 2D Gaussian fitting. For the diffusing eGFP molecule movies, all visible diffusing eGFP intensity profiles in the peak laser excitation region of 10 $\times$ 10 μm^2 were selected by hand using 39 $\times$ 39 pixel boxes centered at the molecule. The center 25 $\times$ 25 pixels of the boxes were used for 2D Gaussian fitting, and the peripheral pixels were used for experimental background analysis.

Before analysis, the camera's intensity count at each pixel in an image was converted into photon count by using the camera-to-photon count conversion factor calibrated the same day of the measurement as described in our previous article [23]. The number of detected photons in an image was obtained by subtracting the total photon count of the BG from the total photon count of the image. The eGFP intensity profiles were fit to a 2D Gaussian function in order to obtain the SD values of the molecule:

$$f(x,y) = f_0 \exp\left[-\frac{(x-x_0)^2}{2s_x^2} - \frac{(y-y_0)^2}{2s_y^2}\right] + \langle b \rangle, \tag{A.1}$$

where f_0 is the multiplication factor, s_x and s_y are SDs in the x- and y- directions, respectively, x_0 and y_0 are the centroid location of the molecule, and $\langle b \rangle$ is the mean background offset in photons.

For the defocusing eGFP analysis, we selected 17 adsorbed eGFP molecules with

a minimum photon count of 229 and signal-to-noise ratios (SNR, $I_0/\sqrt{I_0+\sigma_b^2}$) of higher than 3.75, where I_0 is the peak PSF photon count (after subtracting the mean background offset $\langle b \rangle$) and σ_b^2 is the background variance in photons. For the diffusing eGFP molecules, we used a SNR of 2.5 as a selection criterion, and PSFs with photon counts less than 50 were not used in the analysis because they would be invisible in experimental data. At each exposure time, we acquired 1600 data points from 4 movies recorded at different regions of the imaging chip; the number of diffusing eGFP data used for the experimental analysis that satisfied the SNR criteria are 419 to 1066 for the 0.3 ms to 1 ms exposure times, respectively.

Analytical expression of diffusing eGFP $D_3(s_x)$.

In this section we decompose an eGFP's 3D diffusion process into two components for s_x and D_3 calculation: a 1D diffusion along the axial direction and a 2D diffusion in the lateral directions.

It is known that as the defocusing distance between the fluorophore and the focal plane increases the PSF's SD increases as well. Consequently, calculation of the intensity profile necessitates integrating over all axial locations the molecule may have traveled during the exposure time to obtain an axial-direction-projected PSF, $f(x, y)$. As diffusion in the lateral and axial dimensions are statistically independent of each other, we choose to perform this integration prior to convolving the resulting PSF with $\text{PWDF}_{x,y}$ in the lateral dimensions to obtain the final projected 2D intensity profile of the 3D diffusing molecule on an imaging screen.

In the axial direction, the axial-direction-projected PSF is computed by numerically integrating defocused PSFs through z for all pixelated x, y values (sufficient to contain all defocused PSFs)

$$\int_0^{400} C(z) \exp\left(-\left[\frac{x^2}{2s_x(z)^2} + \frac{y^2}{2s_y(z)^2}\right]\right) \exp\left(-\left[\frac{(z-\langle z_0\rangle)^2}{2A_z \cdot 2D_3 t} + \frac{z}{d}\right]\right) dz, \qquad \text{(A.2)}$$

where $C(z)$ and $s_{x,y}(z)$ are the amplitude and SDs of our imaged, defocused eGFP Gaussian PSFs (SOM text), respectively, $\langle z_0\rangle$ and $A_z \cdot 2D_3 t$ are the mean and variance of diffusing eGFPs' Gaussian PWDF$_z$s (SOM text), $\exp(-z/d)$ describes the decaying TIRF evanescent excitation intensity, and the range for the z-integration is the imaging depth of 0 nm to 400 nm measured from the focal point at the fused-silica surface. The resulting axial-direction-projected PSF $f(x, y)$ remains Gaussian, and the SD is a function of the exposure time t as $s_0'(t) = \sqrt{111^2 + 0.0634 D_3 t}$ nm.

In the lateral directions, the intensity profile $I(x, y)$ of a diffusing eGFP's image is the convolution of the axial-direction-projected eGFP PSF $f(x, y)$ with the PWDF$_{x,y}$, $g(x, y)$ as

$$I(x, y) \propto f(x, y) * g(x, y). \qquad \text{(A.3)}$$

We numerically calculate $g(x, y)$ of a freely diffusing eGFP particle by simulations. Figure A.1A shows 9 random PWDF$_x$s at exposure time $t = 0.6$ ms. Six of the nine PWDF$_x$s have one peak (uni-peaked or unimodal) and can be fitted to a Gaussian function with $R^2 > 0.8$. Figure A.1B shows the SD distribution of PWDF$_x$s, combining the Gaussian fitted SD values for the uni-peaked PWDF$_x$s and the numerical

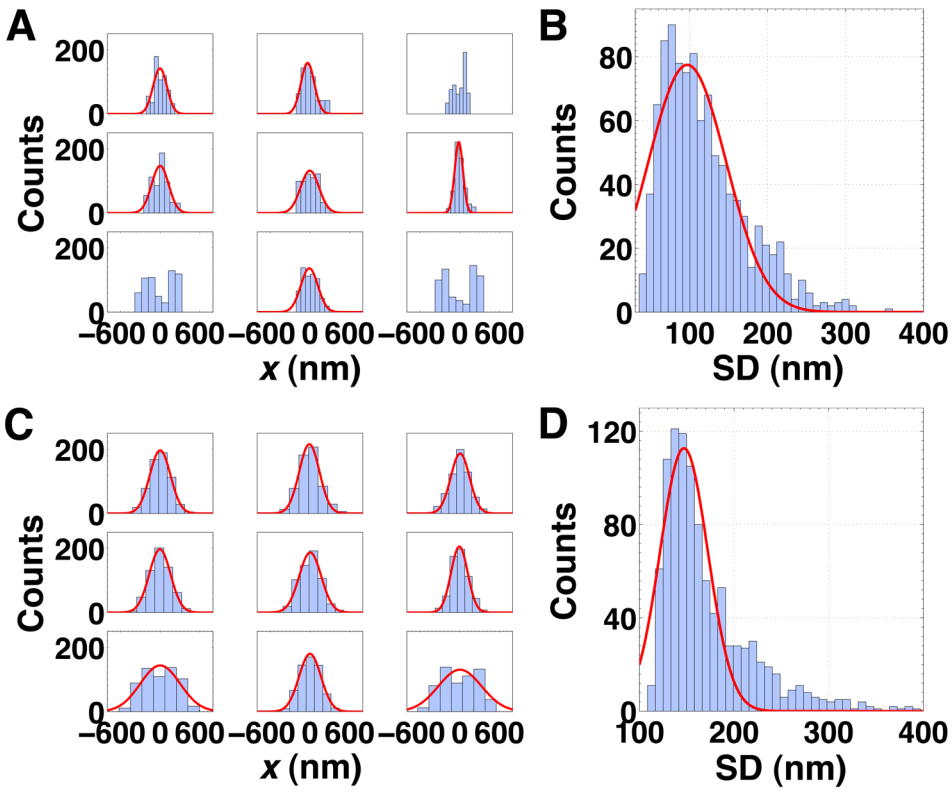

Figure A.1: Study of the eGFP lateral PWDF$_x$s and their convolution with PSFs. (A) Nine random eGFP PWDF$_x$s at 0.6 ms exposure time and Gaussian fits to the unimodal distributions with $R^2 > 0.8$. (B) The distribution of 1000 PWDF$_x$ SDs, fitted with a Gaussian. (C) The 9 PWDF$_x$s in (A) convolved with eGFP PSFs at focus with $s_0 = 108.2$ nm. (D) The SD distribution of 1000 PWDF$_x$ convolved eGFP PSFs at focus and its Gaussian fit.

particle location distribution SD values for the double-peaked PWDF$_x$s; the mean is 96.8 nm. Figure A.1C shows that when the 9 PWDF$_x$s in Fig. A.1A are convolved with single-eGFP PSFs at focus with $s_0 = 108.2$ nm, all convolved PWDF$_x$s fit well to a Gaussian function, and the mean of the SD distribution is 147.1 nm. Therefore, although not all PWDF$_x$s are uni-peaked, taken over all, we can view PWDF$_x$s as Gaussian functions with an average t-dependent SD value of $\sqrt{A_x \cdot 2D_3 t}$. For the 0.6 ms exposure time data, $A_x = 0.0882$. We found A_x to be insensitive to exposure times below 1 ms (mean A_x is 0.0926; data not shown).

Given that $f(x, y)$ (at focus and the axial-direction-projected) and $g(x, y)$s are both Gaussian functions, in the lateral directions, their convolution can be described by another Gaussian function with a variance equal to the sum of the two variances. Using the focused eGFP PSFs with $s_0 = 108.2$ nm and PWDF$_x$ at 0.6 ms, $s_{x,2D} = \sqrt{s_0^2 + A_x \cdot 2D_3 t} = \sqrt{108.2^2 + 96.8^2}$ nm $= 145.2$ nm, very close to the mean SD value of the above PSF-convolved-PWDF$_x$s of 147.1 nm.

Finally, we can calculate the intensity profiles' SDs of freely 3D diffusing molecules. Since we have observed that both the axial-direction-projected PSFs (data not shown) and the lateral PWDF$_{x,y}$s are Gaussian, the final projected intensity profiles' SD of diffusing molecules is

$$s_{x,y} = \sqrt{s_0'^2 + A_{x,y} \cdot 2D_3 t}. \tag{A.4}$$

This relation enables the determination of D_3 from the SD of a single-molecule's intensity profile and the exposure time.

Diffusing eGFP Simulations

We simulated 3D Brownian diffusion eGFP trajectories at a range of exposure times using FCS-determined eGFP $D_3 = 8.86 \times 10^7$ nm^2/s and triplet state statistics. The starting locations of the trajectories followed the distribution function described in the SOM Text. The step sizes in the x, y, and z directions were randomly selected from a Gaussian distribution with a mean of zero and SD of $\sqrt{2D_3t_0}$ with a step time $t_0 = 1$ μs. Because of the reflective fused-silica-water interface, the simulated z values were maintained above zero. The number of steps in a simulation was t/t_0. At each x, y location in a trajectory, when the molecule was not in a triplet dark state, a Poisson distributed number of photons (described in SOM text) were drawn from a Gaussian PSF spatial distribution with a mean of zero and the corresponding SD value for the axial-location (SOM text). This relative displacement of the photons is added to the simulated x, y location of the molecule, generating the actual x, y location of the emitted photons at the simulation step.

The simulated photons of each trajectory were binned into 50×50 pixels with a pixel size of 79 nm. Then the photon count of each pixel was converted into the modified camera count using Eq. 4 in Ref. [23] with the photon multiplication factor of the camera $M = 1$ in order to include the camera count variance effect. Random background photons at each pixel were generated using the corresponding experimental background distribution functions for the exposure time (described in Ref. [23]). The final intensity profiles were fit to a 2D Gaussian function to obtain the two SD values for the image. For each SD datum of diffusing eGFP molecules in

4.3, 1000 independent trajectories were simulated.

SUPPORTING TEXT

Exposure time limit determination for D_3 measurements using Eq. A.4 . In Figure 4.3, the calculated SD starts to deviate from the experimental and simulation results at 0.8 ms. This suggests the existence of an upper bound exposure time for our eGFP studies. In order to determine the appropriate exposure time, we explain the origin of this deviation at long exposure times.

The PWDF$_x$s in Fig. A.1A show both unimodal and double-peaked patterns. When convolved with PSFs, at short exposure times, both the unimodal and double-peaked PWDF$_x$s will produce unimodal intensity profiles suitable for Gaussian fitting; however, at long exposure times, the two-peaked PWDF$_x$s will yield a two-peaked intensity profile. As the exposure time increases, both the fraction of two-peaked PWDF$_x$s and the peak separations increase, while Eq. A.2 still assumes Gaussian fits for all PSF-convolved-PWDF$_x$s. As a consequence, a deviation between the analytical and the experimental s_x appears and increases with exposure time.

The threshold exposure time for the onset of the deviation is determined as follows. When two identical fluorophores are separated by more than the diffraction limit, the combined intensity profile is double-peaked [41]. However, when the concentration of fluorophores peaks in between the diffraction limit separation of the instrument, as for unimodal PWDF$_x$s, the combined intensity profile appear to be unimodal, and can be fitted to a Gaussian function. For the double-peaked PWDF$_x$s, which creates two clusters of fluorophores separated by the distance between the two peaks, this distance, which is approximately the numerical 2×SD value of the molecule's location

distribution, or $2 \cdot \sqrt{A_x \cdot 2D_3 t}$ of the PWDF$_x$s, determines the exposure time limit for when the convolved intensity profiles become two-peaked. When $2 \cdot \sqrt{A_x \cdot 2D_3 t}$ is less the the diffraction limit of 217 nm, the convolved intensity profile is unimodal and can be approximated by a Gaussian function. The threshold is crossed at the exposure time $t \approx 0.8$ ms, where the PWDF$_x$'s mean SD value is 113.6 nm.

From the above analysis, for D_3 determination using Eq. 3 in the main text, the upper bound exposure time can be determined by requiring $2 \cdot \sqrt{A_x \cdot 2D_3 t}$ to be less than the diffraction limit separation of the imaging setup's emission wavelength and $N.A.$

Choosing exposure times for a particle of unknown D_3.

For particles of unknown D_3, exposure time can be scanned until the diffusing particle images are noticeabily larger than that of stationary particles, while remaining unimodal. In this range of exposure times, we can use Eq. 3 for eGFP to calculate D_3 of this particle for the following reason: in Eq. 3, since s_0' is calculated from integration that depends on $D_3 t$ (SOM), and $A_{x,y} \cdot 2D_3 t$ varies with $D_3 t$ only, at the appropriate exposure time, although the D_3 values of the particle and eGFP are different, the $D_3 t$ values can be equivalent. At these exposure times, Eq. 3 for eGFP is restored valid for the particle and can be used to determine the unknown D_3.

FCS determination of the eGFP diffusion coefficient.

In order to independently verify our experimentally determined eGFP PSF mean SD results (Eq. 3) ; therefore also the D_3 result) by using theoretical calculations and

simulations, we performed FCS D_3 measurements of eGFP (at the Washington University Fluorescence Correlation Spectroscopy and Confocal Imaging Facility in the Department of Biochemistry and Molecular Biophysics).

In FCS measurements, fluorescence from freely diffusing eGFP molecules at 3 nM concentration in 0.5X TBE buffer (pH 8) was measured. An autocorrelation function was used to obtain the eGFP diffusion parameters [75],

$$G(t) = \frac{1}{N(1+\frac{\tau}{\tau_d})\sqrt{(1+\frac{\tau}{s^2\tau_d})}}\left(\frac{1-F+Fexp(-\frac{\tau}{\tau_k})}{1-F}\right)+1, \tag{A.5}$$

where τ is the detection time, N is the number of molecules in the detection radius w, s is the structure parameter of the excitation beam focal region (the ratio of the beam radius in z to the beam radius in x and y), $\tau_d = \frac{w^2}{4D_3}$ is the molecule's diffusion time in the imaging area, F is the fraction of molecules in triplet state, and τ_k is the triplet state lifetime.

The excitation wavelength for the FCS measurement was 488 nm, and the emission photons went through a 505 – 550 nm filter. The excitation power was 76.4 kW/cm^2, which was comparable to our excitation power of 37.5 kW/cm^2 in the diffusing eGFP studies. We used Alexa 488 with a known diffusion coefficient $D_3 = 4.35 \times 10^8$ nm^2/s [4] for calibration and obtained $w \approx 250$ nm. For Alexa 488, $\tau_d = 35.6$ μs. Figure A.2 shows the $G(t)$ vs. t plot of the eGFP system, where τ_d was 174.8 μs. Assuming a Gaussian detection volume and using a one-component fit, the best fit to Fig. A.5 yields $F = 12.7$, $\tau_k = 3$ μs, and $s = 10$. Using $\tau_d = \frac{w^2}{4D_3}$, we obtained eGFP

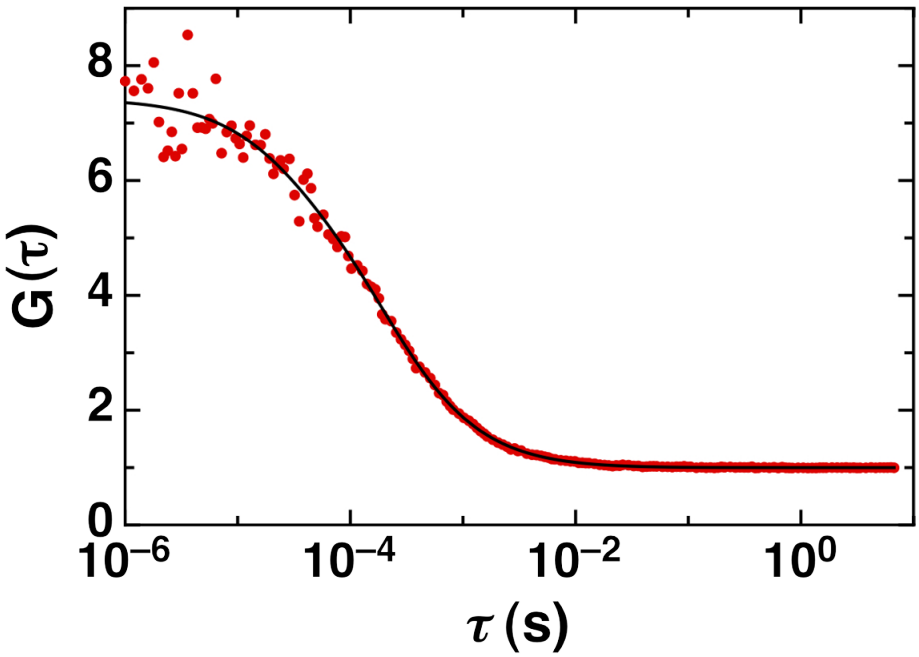

Figure A.2: Diffusing eGFP FCS autocorrelation plot. The black curve is a fit to the raw data (red dots).

$D_3 = 8.86 \times 10^7$ nm^2/s. This value of eGFP D_3 is consistent with reported values [4].

Refractive index mismatch corrections to eGFP intensity profiles.

When a fluorescent molecule in water is imaged through a glass coverslip using a high *N.A.* oil immersion objective, the refractive index mismatch between the water-based solvent and the glass coverslip changes the fluorophore's intensity profiles in two major ways [76]: (i) Due to Snell's law of refraction, the actual axial location of the molecule (measured from the glass coverslip-water interface) is deeper than the apparent axial position of the molecule (defined by the depth in water where the imaged fluorophore's PSF amplitude is maximal). (ii) Due to spherical aberrations, if the focus is at the apparent position of the molecule (we define as $z = 0$), the fluorophore's defocused

intensity profile's SD vs. z relation is asymmetric with respect to $z = 0$ [76]. Figure A.3A shows the geometry of our setup, where the direction of z is positive towards the glass coverslip, opposite to that of Ref. [77]. In our prism-type-TIRF imaging setup, the eGFP molecules were adsorbed on or diffusing near the fused-silica surface in TBE buffer 10.5 μm from the coverslip-water interface. We used fused-silica as the TIRF interface because of its low background noise and thus high SNR for the study when comparing to objective-TIRF imaging that uses glass coverslips as the TIRF interface, where the mean background noise level is at least 6 times higher than ours at comparable laser intensity and exposure times (data not shown).

In order to obtain accurate defocusing eGFP intensity profile parameters for SD and D_3 calculations, we performed calculations and measurements of eGFP adsorbed on fused-silica surfaces. In calculations, we obtained the defocused fluorophores' PSF using the diffraction integral analysis in Ref. [77], which has been used by other groups for mainly calculating the actual axial location of the imaged fluorophores [78, 44]). We assume the final PSF of a defocused fluorophore to be the average of 4 emission polarizations at 0, $\pi/4$, $\pi/2$, and $3\pi/4$, and the light intensity at the spherical wavefront of the point light emitter before reaching the objective was homogeneous. Figures A.3B and C show the SD and amplitude of the calculated fluorophore PSFs using our imaging system's parameter of $N.A. = 1.49$, water's refractive index of $n_1 = 1.34$, glass' refractive index of $n_2 = 1.515$, and an emission wavelength of 525 nm (plotted in blue).

The experimental measurements of defocused eGFP molecules were performed

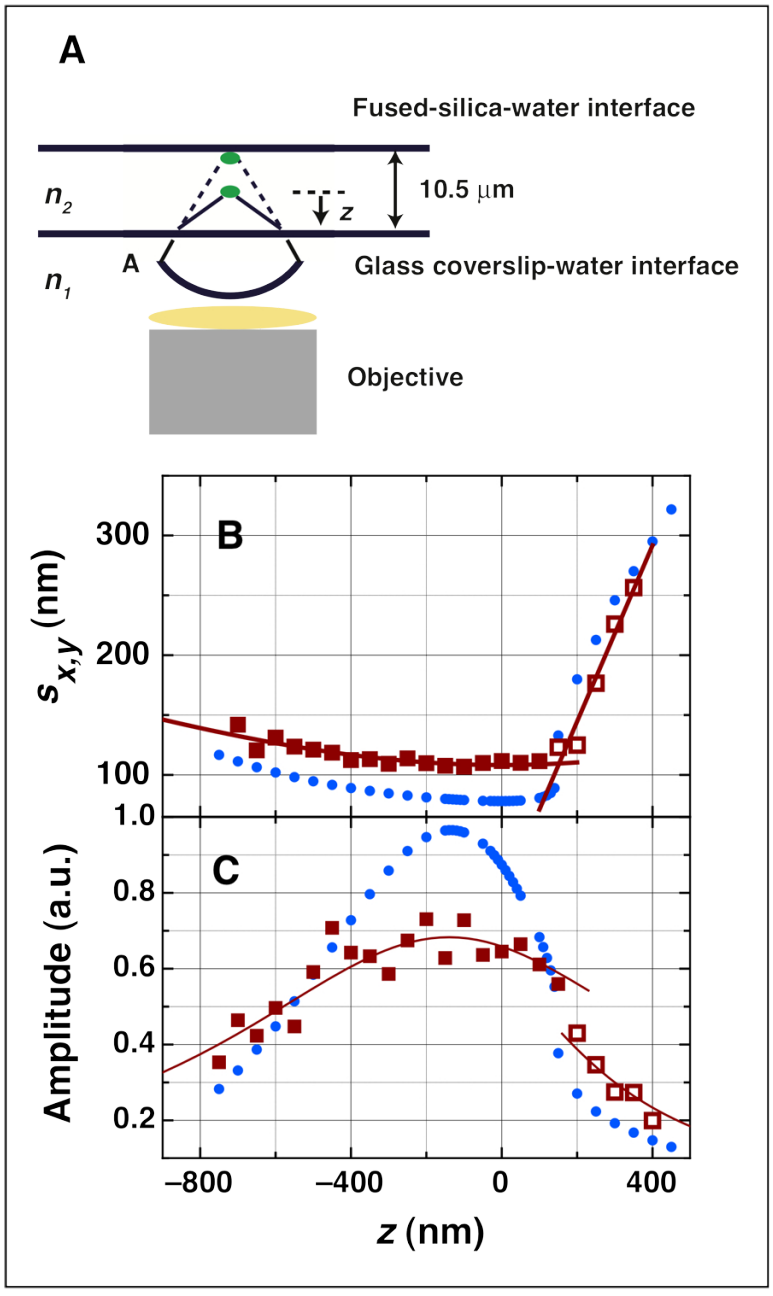

Figure A.3: (A) Our imaging setup and the schematics of emission from a fluorophore in water located at the fused-silica-water interface 10.5 μm away from the coverslip-water interface. Dashed lines trace the emission from the actual location of the fluorophore, and solid lines trace the emission from the apparent location of the fluorophore. The letter "W" labels the wavefront of the emission before reaching the objective. (B) Calculated (blue) and experimental (red) eGFP PSF SDs and (C) amplitude vs the defocusing distance z plots. Lines are fits to the experimental measurements. The focal point is at the minimum of the eGFP s_x vs z curve (same for s_y).

with the molecules adsorbed on fused silica surfaces and a focus-drive (H122, Prior Scientific Inc., Rockland, MA) moving one-way in 100 nm increments through the focal point. The average SD and normalized amplitude of eGFP intensity profiles are plotted in Figs. A.3B and A.3C (in red). We used two fitting protocols for these results. For SD, below $z = 100$ nm, $s_{x,y} = s_0\sqrt{1 + (z/990.3)^2}$ where $s_0 = 108.2$ nm is the minimum in the eGFP $s_{x,y}$ vs z curve that defines the focus; above $z = 100$ nm, a linear fit yields a slope of 0.73. The shape of the experimental defocusing eGFP $s_{x,y}$ vs z curve is consistent with that of the theoretical results, but the values are 30 nm higher. These higher experimental SD values are consistent with the reported values in recent publications using similar imaging setups to ours [40, 23, 6, 79], and it is due to a combination of the pixelation effect of the camera, finite bandwidth of the emission filter, inhomogeneity of the molecule's emission polarization, and the imperfection of the current single-molecule imaging systems. Because of this increase in the experimental eGFP SD values, the corresponding experimental eGFP PSF amplitudes are lower than the theoretical values. Below $z = 150$ nm, $C(z) = \frac{1}{1+(\frac{z+140}{726.7})^2}$; above $z = 150$ nm, $C(z) = \frac{1}{1+(\frac{z+140}{389.4})^2}$. The peak of $C(z)$ does not coincide with the SD minimum at $z = 0$; rather it is shifted to -140 nm. The experimental eGFP functions were used for theoretical and simulation diffusing eGFP SD studies in this article.

Mean emitted photon counts at each simulation step.

The number of photons emitted at each simulation step is a random number drawn from a Poisson distribution with a mean value being $Aexp(-z/d)C(z)s(z)^2$, where

$exp(-z/d)$ describes the exponentially decaying evanescent light intensity and $d \approx$ 117 nm is the penetration depth calculated according to our incident angle of 70° [15], $\frac{C(z)}{2\pi}$ is the amplitude of the refractive-index-mismatch affected eGFP PSF, $2\pi s(z)^2$ corrects for the amplitude ($\frac{1}{2\pi s(z)^2}$)of a simulated Gaussian PSF with SD $s(z)$, and A is a scaling factor that accounts for the quantum efficiency of eGFP molecules. Below we obtain $C(z)$ and A.

We first describe how $C(z)$ is used. When we simulate a PSF by distributing N photons following a 2D Gaussian spatial distribution with SD $s(z)$, the amplitude of the PSF will be $\frac{N}{2\pi s(z)^2}$, where $\frac{1}{2\pi s(z)^2}$ is the amplitude of a normalized Gaussian function with SD $s(z)$ for one photon. However, the Gaussian PSFs with N photons in the refractive-index-mismatch case have the same SD $s(z)$ but a different amplitude, $\frac{C(z)N}{2\pi}$. Thus, when simulating the refractive-index-mismatch affected PSFs by spatially distributing photons using a 2D Gaussian distribution with SD $s(z)$, each photon count should be corrected by factor $C(z)s(z)^2$, where $s(z)^2$ cancels the amplitude of the simulated normalized PSF.

To determine A, a random value was picked to simulate PSF photon distributions at a finite exposure time. After the photon to camera count conversion (with a conversion factor $M = 1$ which introduces additional variance to the emission photon distributions [23]), the modified emission photon count distributions were compared to the experimental distributions at the same exposure times. A was obtained when a good match between the two distributions was achieved. FigureA.4 compares the 0.6 ms experimental and simulated photon emission distributions; A was 0.80 and

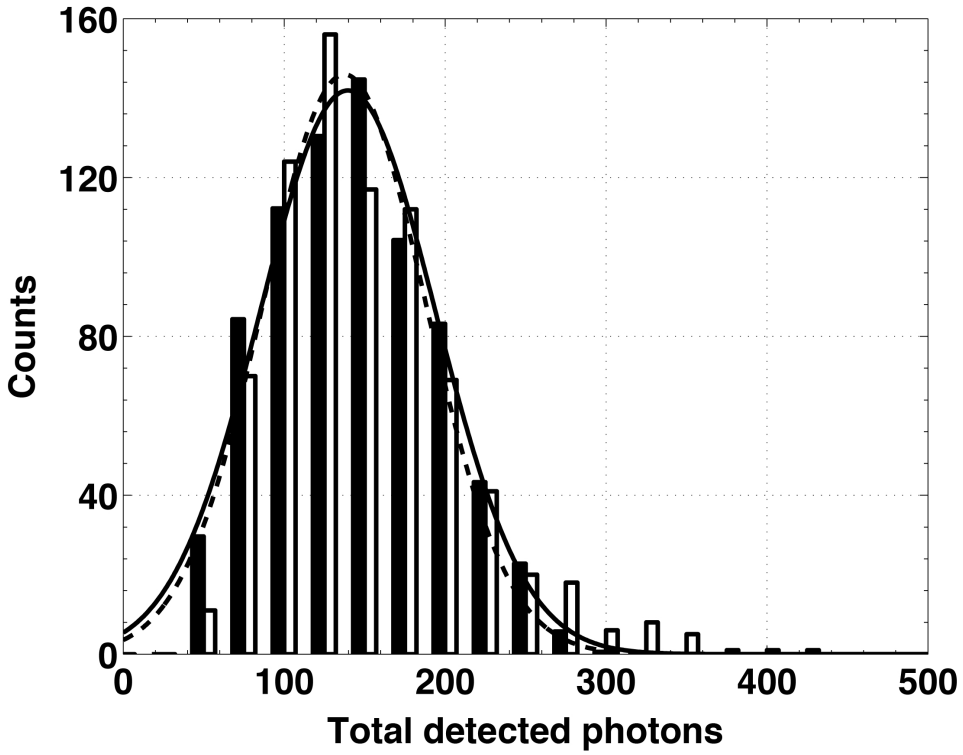

Figure A.4: Comparing the experimental (black) and simulated (empty) photon emission distributions at 0.6 ms. Their respective Gaussian fits in solid and dashed lines are in good agreement.

remains approximately constant for all exposure times (the mean A value for the 0.3 ms to 1 ms exposure times is 0.86; data not shown).

In the theoretical s_x calculations using Eq. SA.2, A was not included since it does not affect the final calculated PSF s_x results.

Starting locations of the imaged diffusing eGFP molecules.

In order to correctly simulate diffusing eGFP molecules near fused-silica surfaces, the axial starting positions are needed. We obtained the eGFP diffusion starting position probability distributions at different exposure times by simulating a fluorophore's emitted photon distributions for a range of starting positions.

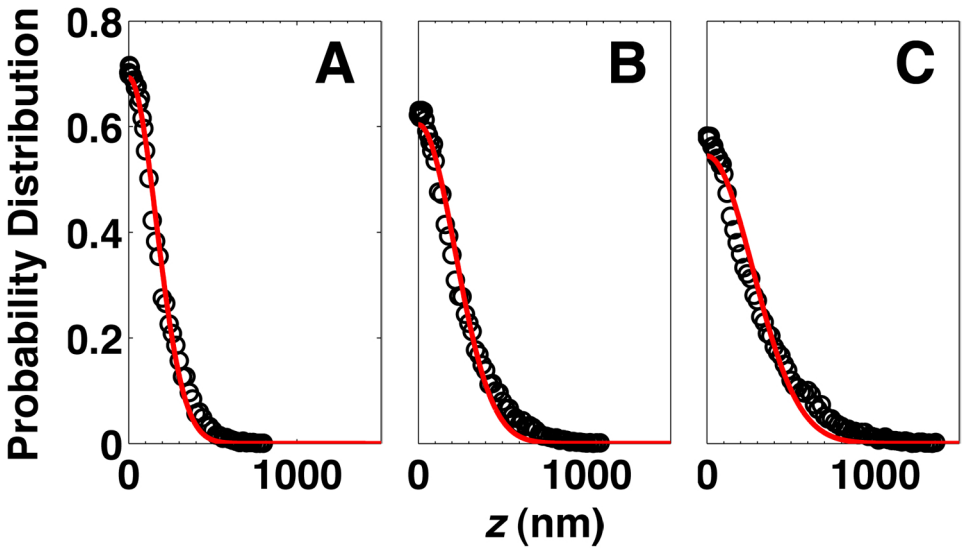

Figure A.5: Simulation results for the diffusing eGFPs' starting-location distribution near the fused-silica-water interface at exposure times of 0.3, 0.7, and 1ms (A, B, and C) and their corresponding fits.

At each exposure time, we simulated 1000 axial-direction diffusion trajectories starting from the fused-silica-water interface to an extended distance in water for the exposure time ($z = 0$ nm to $117 + 3\sqrt{2D_3t}$ nm measuring from the fused-silica surface at focus). A reflective fused-silica surface at $z = 0$ was used. The simulations included the triplet state effect, and the number of photons emitted at each step is described above with the difference of using the mean of the Poisson emission photon count distribution at each step, rather than drawing a random number from the Poisson distribution. At each starting position, we obtained the ratio of the number of photons emitted within the penetration depth ($d = 117$ nm) to all emitted photons for a simulated trajectory, and then the mean ratio for all simulated 1000 trajectories was obtained and plotted in Fig. A.5. The exposure times shown are 0.3, 0.7, and 1 ms, and half-Gaussian functions are fit to the distributions. The fitted SD

values of the starting position distribution functions increase with the exposure time as $SD(t) = 1.538 \times 10^5 t + 122.4$ nm. For $t = 0.3$ ms, Fig. A.5A shows that most molecules we observed experimentally should start within 200 nm of the surface.

Axial-direction PWDF$_z$.

In order to obtain the eGFP PWDF in the axial direction, we performed axial-direction diffusion simulations for all exposure times using the starting position distributions described above and a reflective fused-silica surface at $z = 0$. Figure A.6A shows 9 representative simulated PWDF$_z$s for the 0.6 ms exposure time. Since 84.5% of the data can be fit by a Gaussian function with $R^2 > 0.7$, we use Gaussian function to approximate PWDF$_z$s in Eq. SA.2. Figure A.6B shows the SD distribution of the fitted PWDF$_z$s and the Gaussian fit to the distribution; the mean SD $= \sqrt{A_z \cdot 2D_3 t}$ is 75.8 nm, yielding $A_z = 0.054$. A_z remains constant for other exposure times with a mean value of 0.052. Figure A.6C shows the mean value (z_0) distribution of the fitted PWDF$_z$s and the Gaussian fit to the distribution; the mean z_0 is 142.7 nm. The inset in Fig. A.6C shows that $\langle z_0 \rangle$ increases with t as $\langle z_0 \rangle = \sqrt{0.27 D_3 t} + 25.5$ nm. For each exposure time, 1000 trajectories were simulated to obtain the results.

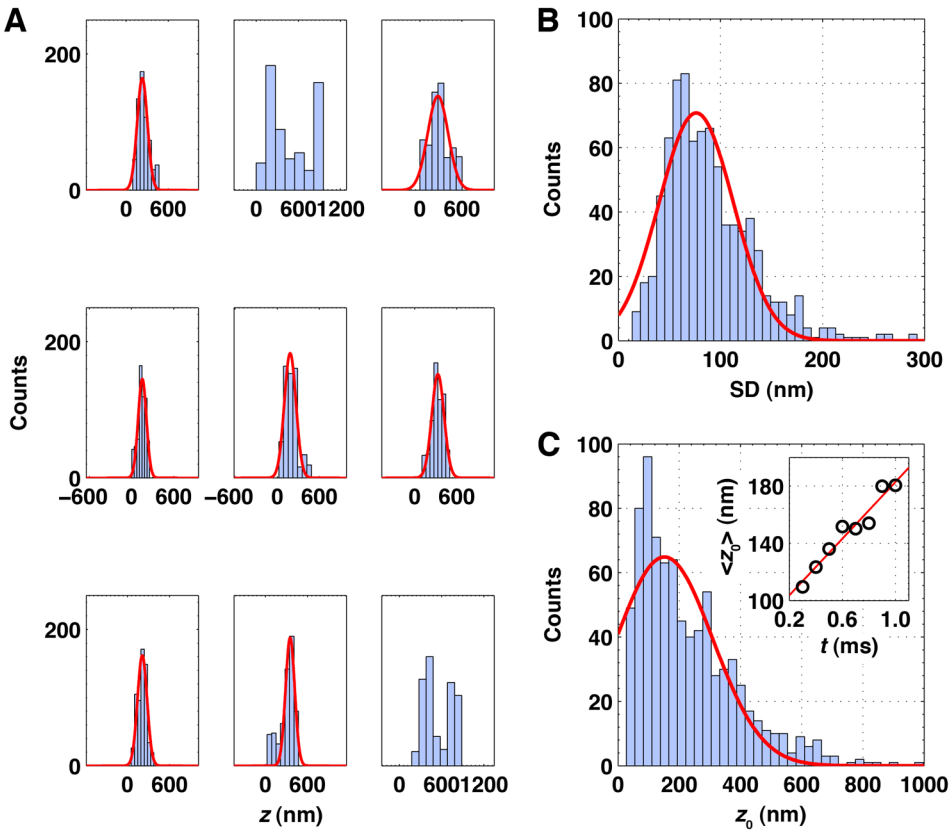

Figure A.6: Study of the axial-direction PWDF parameters. (A) Nine randomly selected PWDF$_z$s at $t = 0.6$ ms. (B) Fitted-PWDF$_z$s' SD distribution and its Gaussian fit. The mean is 75.8 nm. (C) Fitted-PWDF$_z$s' mean (z_0) distribution and the Gaussian fit. Inset, $\langle z_0 \rangle$ increases with $D_3 t$.

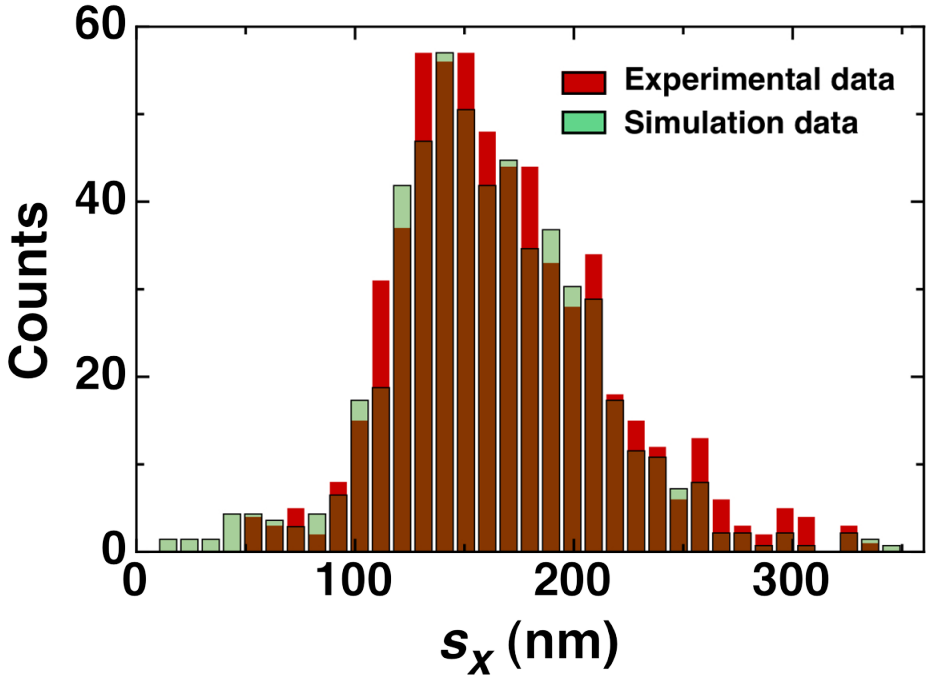

Figure A.7: Comparing the experimental (green) and simulated (red) diffusing eGFP SD distributions.

Appendix B

Background Review: Coordinating Cell Cize with Nutrient Availability

Adaptation to fluctuations in nutrient availability is a fact of life for single celled organisms in the wild. It is of great importance to gain an appropriate knowledge about the potential mechanisms by which nutrient availability and metabolic status are coordinated with cell growth, and cell devision. Generally, devision must be coupled to growth to ensure that average cell size is maintained under a given growth condition. Cells that divided before they doubled in mass would, after several generations, become unsustainably small. Conversely, a population of cells that routinely divided a substantial time after they had doubled in mass would ultimately grow into filaments that are no longer viable.

Carbon availability is the primary determinant of cell size for rapidly growing bacteria. Cells that divided before they doubled in mass would become unsustainably small after several generations. This means that coupling the devision with the growth rate via sensing the nutrient availability is an important determinant of the cell's life. In B. subtilis cells information about carbon availability is transmitted directly to the devision apparatus by accumulation of the UDP-glucose. UDP-glucose inhibits devision through its interaction with UgtP. Under conditions in which UDP-glucose is high, such as during growth in carbon-rich medium, UgtP inhibits FtsZ assembly and delays maturation of the devision ring until cells have reached the appropriate length. Under these conditions UgtP is distributed uniformly throughout the cytoplasm and localizes to the devision ring (also known as Z-ring) in an FtsZ dependent manner, consistent with its role as a devision inhibitor. Conversely, under conditions in which UDP-glucose levels are low, such as during growth in carbon-poor medium, the intracellular concentration of UgtP drops and the remaining protein is sequestered away from mid-cell in small, randomly positioned foci or puncta. UgtP inhibits FtsZ assembly in vitro, indicating it interacts directly with FtsZ to inhibit devision [60]. The in vivo interaction of UgtP with FtsZ was verified in the work of this thesis . Figure 5.1 shows a cartoon of the UgtP function inside the cell.

Appendix C

Prism-type TIRF microscopy components in our Lab

Table C.1: Prism-type TIRF microscopy components in our lab

Microsope	Nikon	TE2000-S
Objectives		
100X (1.49 NA)	Nikon	PlanApo 100x 1.49 NA, ∞/0.17
60X (1.49 NA)	Nikon	PlanApo 60x 1.49 NA, ∞/0.17
EMCCD camera	Andor	iXonEM ()
Laser	Coherent	Innova 70C spectrum, 8 Watts max Visible laser Argone and Krypton mixed gas Multiline output
Flat mirrors	Thorlabs	BB2-E02
Concave mirrors	Thorlabs	CM254-050-P01, f= 50 mm
	Edmund	nt43-548, f = 300 mm
Flip mirror	Thorlabs	BB1-E02
Kinetic mirror	Thorlabs	BB1-E02
Focusing lens	Edmund	nt45-216, f = 400 mm
Optical table	Newport	RS2000, Sealed hole tabletop
Wavelength selector	NEOS	48062-2.5-.55, Polychromatic acousto-optic modulator
Immersion oil	FF	$n = 1.46$
	DF	$n = 1.53$
Filter cubes		
Ex 488 nm / 10 nm EM 525 nm / 50 nm	Chroma	49002, ET GFP, C99696
EX 532 nm / 10 nm EM 580 nm / 60 nm	Chroma	Z 532 BP, Laser, C120571
EX 568 nm / 20 nm EM 605 nm / 50 nm	Chroma	Custom, Z 568, C92426
EX 488 nm / 10 nm EM 525 nm / 50 nm	Chroma	Z 488/568, Dual laser, C1003369
EX 568 nm / 20 nm EM 580 nm up		
EX 500 nm / 20 nm EM 535 nm / 30 nm	Chroma	49003, ET YFP, C138885

Appendix D

Methods and Protocols

D.1 Growing Cells

The cell strains used in our experiments are listed in next section. The evening before a planned microscope experiment, the cell was streaked out from a -80^o stock on agar plate, and was grown overnight for 16 hours in an incubator at 37^o.

The next morning a colony of interest from the agar plate was inoculated into 2 ml of LB buffer and incubated in a shaking incubator at 200 rpm and 30 degree C. When the optical density of the culture reached between 0.3 and 0.5, the culture was back-diluted in the following manner: 20 μL of the culture was added to 2 ml of LB, and 50 μL of Xylose (final concentration of 0.5%) was subsequently added. This culture was grown in the shaker to reach 0.6 OD, and was taken away at this OD for imaging.

Cell Strains Used in Our Experiments

Table D.1: Bacteria Strains

PAL2292	Original name	*bw503*
	Species	*B. subtilis*
	DNA used	*BW484*
	Genotype	*yhxb::tn10; amyE::Pxyl-gfp-ugtP*
PAL2423	Original name	*al198*
	Species	*B. subtilis*
	DNA used	*pYFP-UgtP (AHL192)*
	Genotype	*pgcA::cm::spc;amyE::Pxyl-yfp-ugtP*
PAL522	Original name	
	Species	*B. subtilis*
	Genotype	*trpC2pheA1*

D.2 Cleaning the Slides

By Using Oxygen Plasma Cleaner

A plasma cleaner is an effective way for removing contamination from the surface of fused silica and glass slides. Oxygen plasma is effective in breaking organic bonds on contamination on the surface. The plasma is created in a safe chamber by using a high frequency voltage to ionize the O_2 molecules.

Materials:

Oxygen gas, nitrogen gas, glass cover slip and fused silica slides, plasma chamber cleaner, chemical hood, tweezer

Methods:

1) Before using the plasma chamber the slides are air-cleaned by blowing Nitrogen gas on them. This is done by carefully holding each slide with tweezers and then

blowing Nitrogen gas onto the both surfaces to remove the debris and dust from the air.

2) After air-cleaning, the slides are carefully placed in the plasma chamber by the use of the tweezer.

3) Turn on the plasma chamber.

4) Turn on the vacuum system. Wait until the chamber seems to be pulled in tight and the pressure gauge shows a drop in the pressure of the chamber.

5) Turn on the oxygen flow into the chamber. Wait until the pressure rises to the right amount.

6) Choose the number of minutes needed to run the sample. Usually something between 2 to 5 minutes was used.

By Using the Sonicator

Materials:

Acetone (Fisher), methanol, MilliQ, KOH (1N), Acconox solution (10%), slide holder, sonicator (Branson)

Methods:

1) Placedthe slides in the slide holder as shown in the figure

2) Sonicated for 10 mins with 10% Acconox.

3) Use tweezer to remove the slides and rinse with MilliQ 3 times.

4) Sonicate with 100 percent Acetone for 15 mins. Repeat step 3.

5) Sonicate with 1N KOH for 20 mins. Repeat step 3.

6) Sonicate with 100 percent Methanol. Repeat step 3.

* NOTE: The slides can be stored in Methanol overnight if needed, or just air cleaned and stored in a large tube.

D.3 Preparing the Sample Slide

Materials:

Ethanol, glass coverslip (corning, no.1), fused silica cut to a the appropriate size (2 cm X 2 cm), nail polish, prism, objective, immersion oil, quartz oil, dust-free tissue paper

Methods:

1) The prism is cleaned with ethanol-wetted tissue paper. 2) A small droplet of prism immersion oil is placed on the middle of the prism. 3) The fused silica slide is carefully placed on the droplet.

D.4 Preparing Oxygen Scavenging Buffer

Removing the oxygen from the sample will make the fluorophore more photostable. A typical imaging buffer should be mixed in the sample right before the imaging because a by-product of oxygen system is an acid that gradually reduces the PH of the sample.

The imaging buffer consists of: 96 μL trolox (glucose is already dissolved in this), 2 μL Tris (1M stock), 1 μL NaCl (5M stock) and 1 μL gloxy.

Preparing Gloxy

1) Weigh out 10 mg of yellow gloxy powder (glucose oxidase) from the -20 freezer.

2) Add 80 μL TE buffer PH 8.

3) Add 20 μL of catalase from the refrigerator and mix it well (no vortex). This bottle should be gently swirled before pipetting from it.

4) Spin the mixture down for 2 min at 10,000 g. After spinning you can see a blackish pellet can be seen at the bottom and a clear bright yellow liquid on top. Pipette off the yellow liquid and put it in a 600 μL eppendorf labeled gloxy with the date on it. Gloxy has to be remade at least once a month.

Preparing Trolox

1) Deposit 7-10 mg trolox powder in a 10 mL tube.

2) Add 10 mL milliQ to the tube.

3) The PH drops as the powder dissolves. Compensate for the drop by adding 10 μL

of 5 M NaOH.

4) Shake or vortex for half an hour until the white powder dissolves.

5) Attach a syringe to a 0.2 μm filter. Remove the syringe plunger first. Fill the syringe with the trolox solution and put the plunger back. Let the first ml of the liquid drip into the sink to effectively clean the filter.

6) Wrap the tube in aluminum foil to avoid light exposure and keep at 4C in the fridge. This is good for a month or so.

D.5 Dying the DNA

Materials:

Lambda DNA, BOBO dye, TBE 0.5X

Methods:

1) Dilute the DNA 10 times from 500 $\mu g/ml$ to 50 $\mu g/ml$.

2) After thawing the BOBO dye, pipette out 1 μL and mix it with 400 μL of TBE. This brings the concentration of BOBO to 0.25 μM.

3) Mix 20 μ L of TBE with 0.4 μ L of the DNA from step 1 and 15 μL of the dye from step 3. The final concentration of Dyed DNA is 1.8 pM

Appendix E

Experiment Troubleshooting

E.1 Troubleshooting the Cell Experiments

Problem: The cell exhibits high autofluorescence.

Solution: The cell's autofluorescent background originates from flavin proteins (Harms et al. 2001). Many experiments use a M9 minimal medium for lowering the autofluorescence. In our experiment we did not use M9 since previous studies showed that our proteins would not be stable in M9; moreover, when cells are in the stationary growth phase or under stress the autofluorescence increases.

E.2 Troubleshooting the Single Molecule Experiments

Problem: Checking for contamination. The contamination usually appears as fluorescent molecules at the time of imaging. The data from these molecules could give false information about our real molecule of interest. For example the SD analysis of a 100 data points from GFP could easily be falsified by interference from these single molecules. *NOTE: One property of the contamination fluorescent molecules is that they do not bleach out easily even with high intensity laser light. They appear to blink, but do not photobleach easily, specially those from the fused silica or glass cover slip.

Solution:

1) There may be significant contamination in the objective oil. In general, immersion oil exhibits autofluorescence. To check for this, a sample slide was imaged using epi-fluorescence microscopy. First, the lower surface of the slide (glass coverslip) was brought into focus, and then the volume underneath this surface gradually imaged via tuning with the fine-focusing knob. The amount of fluorescent contamination was observed as it would diffuse in the focus place. For this amount to be kept to a minimum, the immersion oil has to be kept as clean as possible.

2) Contamination can be noticed on the surface of a fused silica or glass slide if the slide is in the presence of air for more than a couple days. To check for the contamination from the fused silica or glass cover slip, these elements were imaged

via epifluorescence or TIRF microscopy with a plain buffer or water under low laser intensity (10A). Slides having less than about 10 fluorescent molecules or so were considered clean, otherwise they were considered contaminated and were cleaned by following the cleaning procedure explained in this chapter. After cutting fused silica chips, they were kept in large tubes with closed lids to prevent from contamination from air.

3) The buffer could sometimes be the contaminated, give rise to fluorescent molecules at the time of imaging. These contaminant molecules can dangerously be counted in as real data, so their elimination or suppression is very important. To minimize contamination from the buffer, small quantities of buffer (20ml) were prepared and used at a time. The buffer was always filtered with 0.2 μm filter.

E.3 Troubleshooting Oxygen Plasma Chamber

Problem: creation of a spark inside the microwave chamber.

Solution: Make sure the oxygen tank is on open. Appearance of a spark inside the chamber means that the oxygen has not been turned on or there is some problem with the oxygen connection.

E.4 Troubleshooting TIRF Imaging

Problem: TIRF is not achieved, although every parameter seems to be correct.

Solution: Check for air bubble in the immersion oil between the prism and the fused silica, or in the objective immersion oil. Such bubbles can be avoided but blowing some air on the oil when depositing it. Another possibility could be that some TBE has leaked from the sample to the objective. This can change the index of refraction and impede the camera's photon collecting ability. Still another possibility is that due to the raising and lowering of the focus, the glass coverslip surface is no linger level. This is not easily detected by naked eye, but is a common reason for failure to achieve TIRF.

E.5 Troubleshooting Drastic Image Drift while Imaging

Problem: The image seems to be drifting drastically.

Solution: Sometimes dropping too large of an oil droplet on the prism makes the fused silica slide onto the prism in microscopic scales. The whole screen would appear to be moving with a velocity of a few hundred nanometers per second. In addition, moving the electronics cables seem to affect the drift. The reason for this was never uncovered.

Appendix F

Instrument Design

F.1 Microscope Stage Design

We custom designed a sample holder stage for our Nikon TE2000-S microscope as one of the first steps toward building our microscopy lab in 2007. The stage holder was designed in AutoCAD software and given this design to the physics department machine shop for manufacturing.

F.2 Beam Scanner Control Box Design

In the epifluorescence imaging setup, we obtained a laser beam that covers all the imaging area of $42\mu m$ X $40\mu m$ with a homogenous excitation intensity by coupling the camera output with a double-mirror scanner. The scanner used was a Model 67XXY Servo-Driver (Cambridge Technology). The control box electrical connection schematics was designed as shown in figure F.4.

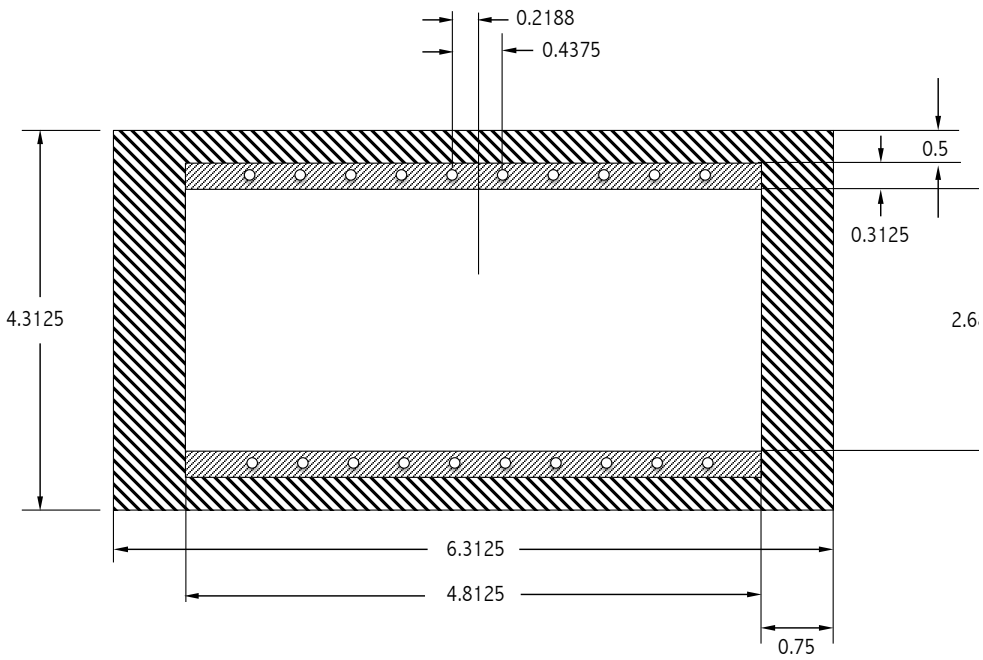

Figure F.1: Top view of the microscope stage, designed in AutoCAD.

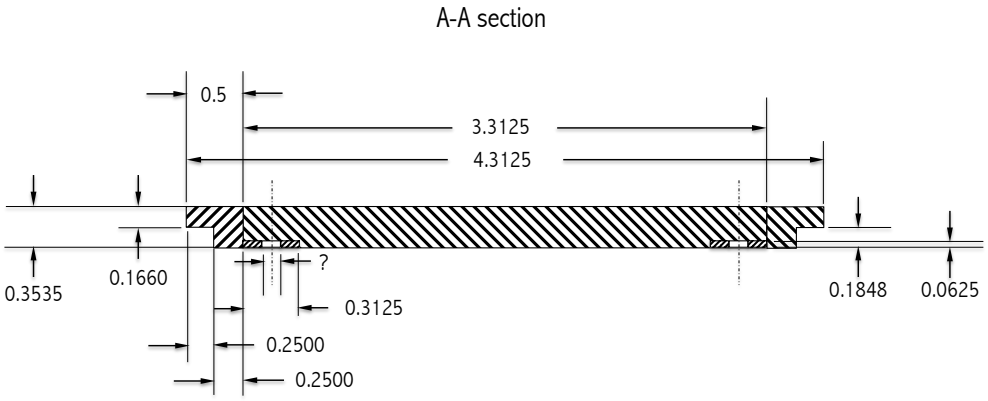

Figure F.2: Front view of the microscope stage, designed in AutoCAD.

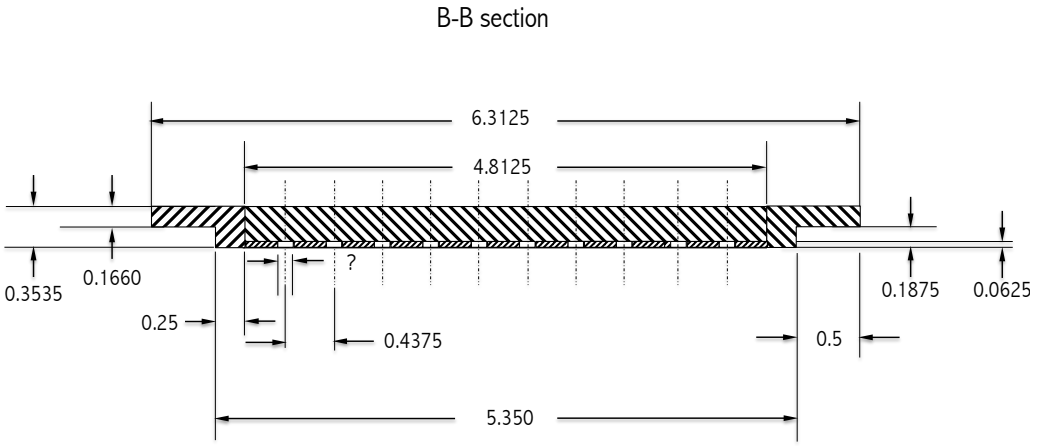

Figure F.3: Side view of the microscope stage, designed in AutoCAD.

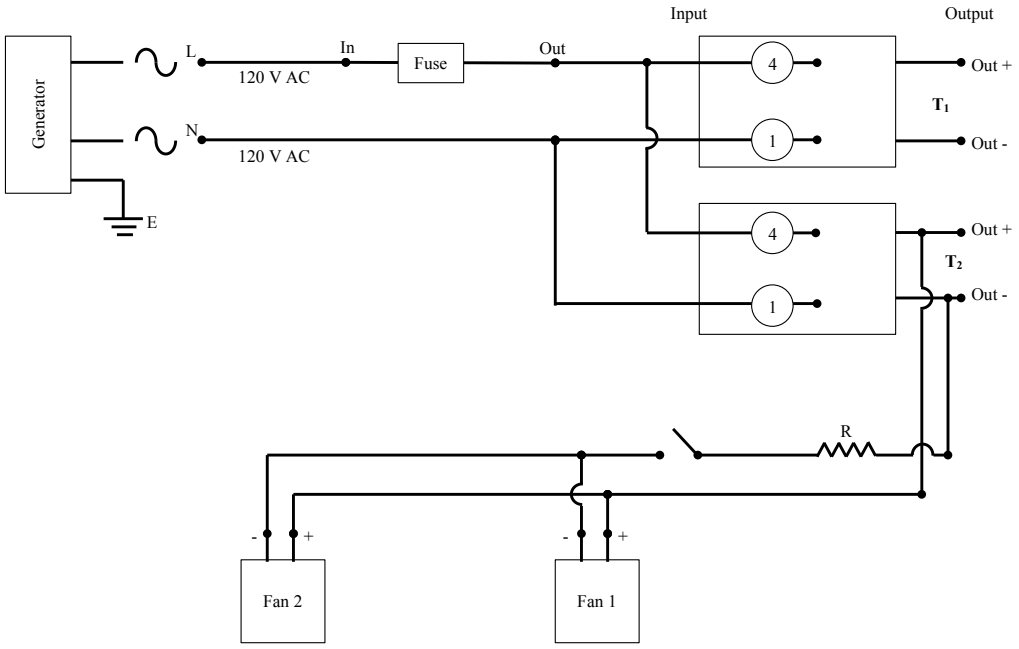

Figure F.4: The electronic circuit of the scanner controller box.

Appendix G

Matlab Codes

This code is written by Shannon Zareh in May 2011 for analyzing the results gotten from running the YMWangDataFittingEvenPixel1109-10 code on the original XY coordinates acquired by ImageJ from the main cell images. This code is written for single trajectory MSD analysis of a single UgtP molecule inside the cells.

```
%Shannon 05-17-2011, written for use with
YMWangDataFittingEvenPixel1109_10 code

clear all

mode=input('run in batch (b) or single file (s) mode
(default is single file)? b/s ','s');
if mode=='b'
    %dirname=uigetdir(('C:\Users\Mike
DeSantis\Desktop\Research Movies\Shawn Movie and Figures\5-
13-09\'),'select folder'); %full path that leads to the
designated folder containing all the text files to be
fitted
    dirname=uigetdir((cd),'select folder');
    if (dirname==0 | isempty(dirname))
        return;
    end
    dircontents=dir(dirname);
    dircontents(1:2)=[];
else
    %[fname1,dirname]=uigetfile('*.txt','select xy
coordinates text file',('C:\Users\Mike
DeSantis\Desktop\Research Movies\Shawn Movie and
Figures\'));
    [fname1,dirname]=uigetfile('*.txt','select xy
coordinates text file',(cd));
    if (fname1==0 | isempty(fname1))
        return;
    end
    dircontents(1,1)=struct('name',fname1);
end

for n=1:length(dircontents)

    fname1=dircontents(n).name

f=[find(isletter(fname1),3,'first'),find(fname1(1:end)=='-
',1,'first')];
    coords(n,2)=str2num(fname1(f(1)+1:f(2)-1));
    coords(n,3)=str2num(fname1(f(2)+1:f(3)-1));
    coords(n,1)=str2num(fname1(f(3)+1:f(4)-1));
    coords=sortrows(coords);

end
```

Figure G.1:

```
infile=uigetfile('*.mat','select which file'); %locates
desired text file
load(infile); %loads/imports data from text file into
matlab usually as a structure array or matrix

% infile2=uigetfile('*.mat','select which file'); %locates
desired text file
% load(infile); %loads/imports data from text file into
matlab usually as a structure array or matrix

cell_width=18*79; % the 02-27-2011 cell (3_1) was cropped
out to have width 18 pixels and length 86 pixels
R=cell_width/2;
cell_length=86*79;
B=10*79; %Box size
sigma_bg=12; % bg sigma (check with yan mei, kinda too
high)
conversion_factor=0.015;
sigma_bg_photon=sigma_bg*conversion_factor;
a=79; %pixel size



Gx=coords(:,2)*79-cell_width/2; %converting the top left
cornoer in the ImageJ cooridinate system to the cell system
where the origin is at the center of the cell
Gy=cell_length-coords(:,3)*79;

x=L(:,5); %importing x and y values from YMW
y=L(:,4);
sx=L(:,3);
sy=L(:,2);

X_cell=Gx+(B/2)+x; %in cell coordinate (origin is at the
center of the cell)
Y_cell=Gy-(B/2)+y;

for i=1:size(coords(:,1),1) %making the first step at 0
    if i<=size(coords(:,1),1)-1
        X0_cell(1,1)=0;
        Y0_cell(1,1)=0;
        X0_cell(i+1,1)=X_cell(i+1,1)-X_cell(1,1);
         Y0_cell(i+1,1)=Y_cell(i+1,1)-Y_cell(1,1);

    end
end
```

Figure G.2:

```
 % figure(1)
% subplot(2,2,1)
% plot(X_cell,Y_cell,'-
o','MarkerFaceColor','k','MarkerSize',3)
% xlabel('X
cell','fontsize',20,'fontweight','b','fontname','Times New
Roman');
% ylabel('Y
cell','fontsize',20,'fontweight','b','fontname','Times New
Roman');
%
set(gca,'fontsize',15,'fontweight','b','LineWidth',2,'fontn
ame','Times New Roman');
%
% subplot(2,2,3)
% plot(X0_cell,Y0_cell,'-
o','MarkerFaceColor','k','MarkerSize',3)
% xlabel('X0
cell','fontsize',20,'fontweight','b','fontname','Times New
Roman');
% ylabel('Y0
cell','fontsize',20,'fontweight','b','fontname','Times New
Roman');
%
set(gca,'fontsize',15,'fontweight','b','LineWidth',2,'fontn
ame','Times New Roman');


z=R-sqrt(R^2-X_cell.^2);

for i=0:30;
    t(i+1,1)=i*30;
    Time=t/1000;
end

x_final=R*atan(X_cell./sqrt(R.^2-X_cell.^2)); % in the
expanded-cylinder coordinate
y_final=Y_cell;

for i=1:size(coords(:,1),1) %making the first step at 0
    if i<=size(coords(:,1),1)-1
        x0_final(1,1)=0;
        y0_final(1,1)=0;
        x0_final(i+1,1)=x_final(i+1,1)-x_final(1,1);
         y0_final(i+1,1)=y_final(i+1,1)-y_final(1,1);

    end
end
```

Figure G.3:

```
% subplot(2,2,2)
% plot(x_final,y_final,'-
o','MarkerFaceColor','k','MarkerSize',3)
% xlabel('x
final','fontsize',20,'fontweight','b','fontname','Times New
Roman');
% ylabel('y
final','fontsize',20,'fontweight','b','fontname','Times New
Roman');
%
set(gca,'fontsize',15,'fontweight','b','LineWidth',2,'fontn
ame','Times
% New Roman');
%
% subplot(2,2,4)
% plot(x0_final,y0_final,'-
o','MarkerFaceColor','k','MarkerSize',3)
% xlabel('x0
final','fontsize',20,'fontweight','b','fontname','Times New
Roman');
% ylabel('y0
final','fontsize',20,'fontweight','b','fontname','Times New
Roman');
%
set(gca,'fontsize',15,'fontweight','b','LineWidth',2,'fontn
ame','Times New Roman');


%calculate theta
[slope]=polyfit(x_final,y_final,1);
theta=atan(slope(1,1));

[slope_0]=polyfit(x0_final,y0_final,1);
theta_0=atan(slope(1,1));

y_final_corrected=y_final-slope(1,2);
y0_final_corrected=y0_final-slope_0(1,2);


u=x_final*cos(theta)+y_final_corrected*sin(theta);% change
coordinate system such that the mol is moving on a straight
line.
v=-x_final*sin(theta)+y_final_corrected*cos(theta);

for i=1:size(coords(:,1),1) %making the first step at 0
    if i<=size(coords(:,1),1)-1
```

Figure G.4:

```
u0(1,1)=0;
        v0(1,1)=0;
        u0(i+1,1)=u(i+1,1)-u(1,1);
         v0(i+1,1)=v(i+1,1)-v(1,1);

    end
end


%estimating errors
dx=sqrt((2*(sx.^2)./L(:,7))+(8*pi*((sx.^2).^(3/2)).*((sy.^2
).^(1/2)*(sigma_bg_photon)^2)./((a^2)*(L(:,7).^2))).*(1.42)
); %error to the mean (in the EMCCD frame)
dy=sqrt((2*(sy.^2)./L(:,7))+(8*pi*((sy.^2).^(3/2)).*((sx.^2
).^(1/2)*(sigma_bg_photon)^2)./((a^2)*(L(:,7).^2))).*(1.42)
);

dx_final=(R./sqrt(R^2-X_cell.^2)).*dx;  %error to the mean
(in the expanded-cell frame)
dy_final=dy;

du=sqrt((cos(theta)*dx_final).^2+(sin(theta)*dy_final).^2);
dv=sqrt((-
sin(theta)*dx_final).^2+(cos(theta)*dy_final).^2);

frames=(max(coords(:,1))-min(coords(:,1)))+1;
N=length(coords(:,1));%total number of positions measured
nc=((3*N+3)+sqrt((3*N+3)^2-4*11*4))/22;

%
% figure(2)
% subplot(2,1,1)
% errorbar(u,v,du,'-
o','MarkerFaceColor','k','MarkerSize',3)
%
xlabel('u','fontsize',20,'fontweight','b','fontname','Times
New Roman');
%
ylabel('v','fontsize',20,'fontweight','b','fontname','Times
New Roman');
%
set(gca,'fontsize',15,'fontweight','b','LineWidth',2,'fontn
ame','Times New Roman');
%
% subplot(2,1,2)
% errorbar(u0,v0,dy_final,'-
o','MarkerFaceColor','k','MarkerSize',3)
```

Figure G.5:

```
xlabel('u0','fontsize',20,'fontweight','b','fontname','Time
s New Roman');
%
ylabel('v0','fontsize',20,'fontweight','b','fontname','Time
s New Roman');
%
set(gca,'fontsize',15,'fontweight','b','LineWidth',2,'fontn
ame','Times New Roman');



for i=1:size(coords,1)
    if i<=size(coords,1)-1
        frame(1,1)=1;
        frame(i+1,1)=coords(i+1,1)-coords(1,1)+1;

    end
end



for i=1:max(find(u(:,1))) %making a matrix where the colums
are equal to the chop distance. For chop distances where
the displacement doesn't exist we get NaN

    for p=1:max(find(u(:,1)))

        if (i+p)<=max(find(u(:,1)))
            n=frame(i+p,1)-frame(p,1);
            displacement_u(p+i,n)=u(p+i,1)-u(p,1);
            displacement_u_sq(p+i,n)=
displacement_u(p+i,n)^2;
        else
            displacement_u(p+i,n)=NaN;
            displacement_u_sq(p+i,n)=NaN;
        end


    end
    for k=1:size(displacement_u,1)
        for j=1:size(displacement_u,2)
          if(displacement_u(k,j))==0
              displacement_u(k,j)=NaN;


          end
          if displacement_u_sq(k,j)==0;
```

Figure G.6:

```
            displacement_u_sq(k,j)=NaN;
          end


        end
    end

end



figure(3)
subplot(2,2,1)

for n=1:size(displacement_u_sq,2)  %making the plot of the
displacement as a function of chop distance (n)
    for i=1:size(displacement_u_sq,1)


        plot(n,displacement_u_sq(i,n),'kx')
        hold on



    end
end

hold on figure

 for n=1:size(displacement_u_sq,2) %calculatin the freaking
MSD.  Apparently Matlab doesn't know how to mean a vector
if there are NaN elements, so I had to write my own.

MSD_u(1,n)=mean(displacement_u_sq(find(displacement_u_sq(:,
n)>0),n));

 end



plot(MSD_u,'r','MarkerFaceColor','k','MarkerSize',3)
xlabel('n','fontsize',20,'fontweight','b','fontname','Times
New Roman');
ylabel('MSD_u
(nm^2)','fontsize',20,'fontweight','b','fontname','Times
New Roman');
set(gca,'fontsize',15,'fontweight','b','LineWidth',2,'fontn
ame','Times New Roman');
```

Figure G.7:

```
for i=1:size(u(:,1),1) %calculating the real displacement
with respect to the first spot.
    if i<size(u(:,1),1)
        Real_displacement_u(1,1)=0;
        Real_displacement_u(i+1,1)=u(i+1,1)-u(1,1);

    end
end



msd_u=MSD_u';
msd_u_noise=msd_u-(2*(mean(du)^2));
t=frame*0.030;
tt=2*t;
[Diff_coef_u]=polyfit(tt(1:round(nc)),msd_u_noise(1:round(n
c)),1);
D1_u=Diff_coef_u(1,1);  % this D is in nm^2/s
dD1_u=D1_u*sqrt((2*(nc)^2+1)/((3*nc)*(N-nc+1)));
%dD1=sqrt(2*D1*t)^2*((2*frame.^2)+1)/(3*frame.*(frames-
frame+1));


subplot(2,2,2)
errorbar(frame,Real_displacement_u,du,'r','MarkerFaceColor'
,'k','MarkerSize',3)
xlabel('step
number','fontsize',20,'fontweight','b','fontname','Times
New Roman');
ylabel('u
(nm)','fontsize',20,'fontweight','b','fontname','Times New
Roman');
set(gca,'fontsize',15,'fontweight','b','LineWidth',2,'fontn
ame','Times New Roman');


% from here below, do the same exact thing for diffusion in
v:

for i=1:max(find(v(:,1))) %making a matrix where the colums
are equal to the chop distance. For chop distances where
the displacement doesn't exist we get NaN

    for p=1:max(find(v(:,1)))
```

Figure G.8:

```
if (i+p)<=max(find(v(:,1)))
            n=frame(i+p,1)-frame(p,1);
            displacement_v(p+i,n)=v(p+i,1)-v(p,1);

displacement_v_sq(p+i,n)=displacement_v(p+i,n)^2;
        else
            displacement_v(p+i,n)=NaN;
            displacement_v_sq(p+i,n)=NaN;
        end


    end
    for k=1:size(displacement_v,1)
        for j=1:size(displacement_v,2)
          if(displacement_v(k,j))==0
              displacement_v(k,j)=NaN;


          end
          if displacement_v_sq(k,j)==0;
              displacement_v_sq(k,j)=NaN;
          end


        end
    end

end



subplot(2,2,3)

for n=1:size(displacement_v_sq,2)  %making the plot of the
displacement as a function of chop distance (n)
    for i=1:size(displacement_v_sq,1)


        plot(n,displacement_v_sq(i,n),'kx')
        hold on



    end
end

hold on figure
```

Figure G.9:

```
for n=1:size(displacement_v_sq,2) %calculatin the freaking
MSD.  Apparently Matlab doesn't know how to mean a vector
if there are NaN elements, so I had to write my own.

MSD_v(1,n)=mean(displacement_v_sq(find(displacement_v_sq(:,
n)>0),n));

 end



plot(MSD_v,'r','MarkerFaceColor','k','MarkerSize',3)
xlabel('n','fontsize',20,'fontweight','b','fontname','Times
New Roman');
ylabel('MSD_v
(nm^2)','fontsize',20,'fontweight','b','fontname','Times
New Roman');
set(gca,'fontsize',15,'fontweight','b','LineWidth',2,'fontn
ame','Times New Roman');



for i=1:size(v(:,1),1) %calculating the real displacement
with respect to the first spot.
    if i<size(v(:,1),1)
        Real_displacement_v(1,1)=0;
        Real_displacement_v(i+1,1)=v(i+1,1)-v(1,1);

    end
end


msd_v=MSD_v';
msd_v_noise=msd_v-(2*(mean(dv)^2));
t=frame*0.030;
tt=2*t;
[Diff_coef_v]=polyfit(tt(1:round(nc)),msd_v_noise(1:round(n
c)),1);
D1_v=Diff_coef_v(1,1);  % this D is in nm^2/s
dD1_v=D1_v*sqrt((2*(nc)^2+1)/((3*nc)*(N-nc+1)));
%dD1=sqrt(2*D1*t)^2*((2*frame.^2)+1)/(3*frame.*(frames-
frame+1));


subplot(2,2,4)
errorbar(frame,Real_displacement_v,dv,'r','MarkerFaceColor'
,'k','MarkerSize',3)
```

Figure G.10:

```
xlabel('step
number','fontsize',20,'fontweight','b','fontname','Times
New Roman');
ylabel('v
(nm)','fontsize',20,'fontweight','b','fontname','Times New
Roman');
set(gca,'fontsize',15,'fontweight','b','LineWidth',2,'fontn
ame','Times New Roman');


% figure
% plot3(X_cell,Y_cell,frame);
% xlabel('X_(EMCCD)
nm','fontsize',20,'fontweight','b','fontname','Times New
Roman');
% ylabel('Y_(EMCCD)
nm','fontsize',20,'fontweight','b','fontname','Times New
Roman');
%
ylabel('Frame','fontsize',20,'fontweight','b','fontname','T
imes New Roman');
%
set(gca,'fontsize',15,'fontweight','b','LineWidth',2,'fontn
ame','Times New Roman');
% grind on



results_spMSD(:,1)=x;
results_spMSD(:,2)=y;
results_spMSD(:,3)=X_cell;
results_spMSD(:,4)=Y_cell;
results_spMSD(:,5)=X0_cell;
results_spMSD(:,6)=Y0_cell;
results_spMSD(:,7)=x_final;
results_spMSD(:,8)=y_final;
results_spMSD(:,9)=x0_final;
results_spMSD(:,10)=y0_final;
results_spMSD(:,11)=y_final_corrected;
results_spMSD(:,12)=y0_final_corrected;
results_spMSD(:,13)=u;
results_spMSD(:,14)=v;
results_spMSD(:,15)=u0;
results_spMSD(:,16)=v0;
results_spMSD(:,17)=Real_displacement_u;
results_spMSD(:,18)=Real_displacement_v;
results_spMSD(:,19)=Gx;
results_spMSD(:,20)=Gy;
```

Figure G.11:

```
results_spMSD(:,21)=coords(:,1); %frame
results_spMSD(:,22)=coords(:,2); %pixel number (x)
results_spMSD(:,23)=coords(:,3);  %pixel number (y)
results_spMSD(:,24)=dx; %error in measuring mean
results_spMSD(:,25)=dy;
results_spMSD(:,26)=dx_final;
results_spMSD(:,27)=dy_final;
results_spMSD(:,28)=du;
results_spMSD(:,29)=dv;
results_spMSD(:,30)=frame;

ext='_spMSD_noiseuv.mat';
    file=[infile,ext];

save(file,'displacement_u','displacement_u_sq','displacemen
t_v','displacement_v_sq','n','i','MSD_u','Time','z','R','re
sults_spMSD','nc','N','coords','u','D1_u','D1_v','frame','f
rames','Real_displacement_u','Real_displacement_v','Diff_co
ef_u','Diff_coef_v','dD1_u','dD1_v')
```

Figure G.12:

Bibliography

[1] T. Funatsu, Y. Harada, M. Tokunaga, K. Saito, T. Yanagida, *Nature* **374**, 555 (1995).

[2] D. Magde, E. Elson, W. W. Webb, *Physical Review Letters* **29**, 705 (1972).

[3] A. Schenk, S. Ivanchenko, C. Röcker, J. Wiedenmann, G. U. Nienhaus, *Biophysical Journal* **86**, 384 (2004).

[4] Z. Petrášek, P. Schwille, *Biophysical Journal* **94**, 1437 (2008).

[5] J. M. Fernandez, H. Li, *Science* **303**, 1674 (2004).

[6] A. Yildiz, *et al.*, *Science* **300**, 2061 (2003).

[7] T. Ha, *et al.*, *Proceedings of the National Academy of Sciences* **93**, 6264 (1996).

[8] T. Ha, T. A. Laurence, D. S. Chemla, S. Weiss, *The Journal of Physical Chemistry B* **103**, 6839 (1999).

[9] W. E. Moerner, L. Kador, *Phys. Rev. Lett.* **62**, 2535 (1989).

[10] M. Orrit, J. Bernard, *Phys. Rev. Lett.* **65**, 2716 (1990).

[11] E. Betzig, R. J. Chichester, *Science* **262**, 1422 (1993).

[12] T. Kues, R. Peters, U. Kubitscheck, *Biophysical journal* **80**, 2954 (2001).

[13] W. E. Moerner, *Proceedings of the National Academy of Sciences of the United States of America* **104**, 12596 (2007).

[14] J. Lichtman, J. Conchello, *Nature Methods* **2**, 910 (2005).

[15] D. Axelrod, *Methods in Cell Biology* **30**, 245 (1989).

[16] R. H. Webb, *Reports on Progress in Physics* **59**, 427 (1996).

[17] T. Ha, *Methods* **25**, 78 (2001).

[18] M. K. Cheezum, W. F. Walker, W. H. Guilford, *Biophysical journal* **81**, 2378 (2001).

[19] R. Y. Tsien, *Annual review of biochemistry* **67**, 509 (1998).

[20] N. Bobroff pp. 1152–1157 (1986).

[21] G. J. Schütz, H. Schindler, T. Schmidt, *Biophysical journal* **73**, 1073 (1997).

[22] R. E. Thompson, D. R. Larson, W. W. Webb, *Biophysical journal* **82**, 2775 (2002).

[23] M. C. DeSantis, S. H. DeCenzo, J.-L. Li, Y. M. Wang, *Optics express* **18**, 6563 (2010).

[24] C. Joo, H. Balci, Y. Ishitsuka, C. Buranachai, T. Ha, *Annual review of biochemistry* **77**, 51 (2008).

[25] J. Widengren, *et al.*, *Analytical chemistry* **78**, 2039 (2006).

[26] M. P. Gordon, T. Ha, P. R. Selvin, *DNA Sequence* **101**, 6462 (2004).

[27] A. L. Zydney, C.-C. Ho, *Biotechnology and Bioengineering* **83**, 537 (2003).

[28] J. J. Gray, *Current opinion in structural biology* **14**, 110 (2004).

[29] R. A. Latour, *Biomaterials: Protein-Surface Interactions* (Taylor & Francis, New York, 2005), pp. 1–15.

[30] Y. F. Yano, *et al.*, *Langmuir* **25**, 32 (2009).

[31] H. H. J. de Jongh, *et al.*, *Biopolymers* **74**, 131 (2004).

[32] Y. Deng, Y. Y. Zhu, T. Kienlen, A. Guo, *Journal of the American Chemical Society Communications* **128**, 2768 (2006).

[33] Y. F. Yano, *et al.*, *Langmuir* **25**, 32 (2009).

[34] T. M. Squires, R. J. Messinger, S. R. Manalis, *Nature Biotechnology* **26**, 417 (2008).

[35] E. N. Vasina, E. Paszek, D. V. Nicolau, D. V. Nicolau, *Lab on a Chip* **9**, 891 (2009).

[36] K. E. Sapsford, F. S. Ligler, *Biosensors and Bioelectronics* **19**, 1045 (2004).

[37] T. S. Tsapikouni, Y. F. Missirlis, *Materials Science and Engineering B* **152**, 2 (2008).

[38] J. N. Israelachvili, *Intermolecular and surface forces* (Academic Press, 1992), second edn.

[39] Y. M. Wang, *et al.*, *Proceedings of the National Academy of Sciences of the United States of America* **102**, 9796 (2005).

[40] Y. M. Wang, R. H. Austin, E. C. Cox, *Physical Review Letters* **97**, 048302 (2006).

[41] S. H. DeCenzo, M. C. DeSantis, Y. M. Wang, *Optics Express* **18**, 16628 (2010).

[42] C. VANOSS, *et al.*, *Colloids and Surfaces B-biointerfaces* **30**, 25 (2003).

[43] J. Gorman, E. C. Greene, *Nature Structural and Molecular Biology* **15**, 768 (2008).

[44] M. A. Thompson, M. D. Lew, M. Badieirostami, W. E. Moerner, *Nano Letters* **10**, 211 (2010).

[45] M. Auer, *et al.*, *Drug Discoveries and Therapeutics* **3**, 457 (1998).

[46] A. Ganser, *et al.*, *Analytical Chemistry* **81**, 5233 (2009).

[47] L. He, B. Niemeyer, *Biotechnology progress* **19**, 544 (2003).

[48] G. A. Webb, *Nuclear magnetic resonance*, vol. 34 (The Royal Society of Chemistry, Thomas Graham House, Science Park, Milton Road, Cambridge CB40WF, UK, 2005).

[49] B. Berne, R. Pecora, *Dynamic Light Scattering: With application to Chemistry, Biology and Physics.* (General Publishing Company, Ltd, 30 Lesmill Road, Don Mills, Toronto, Ontario, 2000).

[50] E. O. Potma, W. P. de Boeij, L. Bosgraaf, J. Roelofs, P. J. M. van Haastert nd Douwe A Wiersma, *Biophysical Journal* **81**, 2010 (2001).

[51] P. C. Blainey, A. M. van Oijent, A. Banerjee, G. L. Verdine, X. S. Xie, *Proceedings of the National Academy of Sciences of the United States of America* **103**, 5752 (2006).

[52] M. V. Nanchury, E. S. Seeley, H. Jin, *Annual Review of Cell and Developmental Biology* **26**, 59 (2010).

[53] K. Ritchie, J. Spector, *Biopolymers* **87**, 95 (2007).

[54] H. Qian, M. P. Sheetz, E. L. Elson, *Biophysical journal* **60**, 910 (1991).

[55] V. Levi, Q. Ruan, E.Gratton, *Biophysical Journal* **88**, 2919 (2005).

[56] S. Semrau, A. Pezzarossa, T. Schmidt, *Biophysical Journal* **100**, L19 (2011).

[57] J. Schuster, F. Cichos, C. von Borczyskowski, *The Journal of Physical Chemistry A* **106**, 5403 (2002).

[58] S. K. G. Zareh, Y. M. Wang, *Microscropy Research and Technique* **In press** (2011).

[59] R. Swaminathan, C. P. Hoang, A. S. Verkman, *Biophysical Journal* **72**, 1900 (1997).

[60] R. B. Weart, *et al.*, *Cell* **130**, 335 (2007).

[61] M. B. Elowitz, M. G. Surette, P. E. Wolf, J. B. Stock, S. Leibler, *Journal of bacteriology* **181**, 197 (1999).

[62] P. H. M. Lommerse, B. E. Snaar-Jagalska, H. P. Spaink, T. Schmidt, *Journal of cell science* **118**, 1799 (2005).

[63] A. Nishibori, J. Kusaka, H. Hara, M. Umeda, K. Matsumoto, *Society* **187**, 2163 (2005).

[64] Y.-L. Shih, L. Rothfield, *Microbiology and molecular biology reviews : MMBR* **70**, 729 (2006).

[65] L. J. Jones, R. Carballido-López, J. Errington, *Cell* **104**, 913 (2001).

[66] E. C. Garner, *et al.*, *Science* (2011).

[67] S. Y. Kim, Z. Gitai, A. Kinkhabwala, L. Shapiro, W. E. Moerner, *Proceedings of the National Academy of Sciences of the United States of America* **103**, 10929 (2006).

[68] H. J. Defeu Soufo, P. L. Graumann, *EMBO reports* **5**, 789 (2004).

[69] L. Niu, J. Yu, *Biophysical journal* **95**, 2009 (2008).

[70] S. Ben-Yehuda, R. Losick, *Cell* **109**, 257 (2002).

[71] K. A. Michie, L. G. Monahan, P. L. Beech, E. J. Harry, *Society* **188**, 1680 (2007).

[72] Z. Gitai, L. Shapiro, *Proceedings of the National Academy of Sciences of the United States of America* **100**, 7423 (2003).

[73] W. E. Moerner, *The Journal of Chemical Physics* **117**, 10925 (2002).

[74] J. Lippincott-Schwartz, E. Snapp, a. Kenworthy, *Nature reviews. Molecular cell biology* **2**, 444 (2001).

[75] K. Weisshart, V. Jüngel, S. J. Briddon, *Current Pharmaceutical Biotechnology* **5**, 135 (2004).

[76] K. I. Willig, *et al.*, *Nature Methods* **3**, 721 (2006).

[77] A. Egner, S. W. Hell, *Journal of Microscopy* **193**, 244 (1999).

[78] B. Huang, W. Wang, M. Bates, X. Zhuang, *Science* **319**, 810 (2008).

[79] A. Yildiz, M. Tomishige, R. D. Vale, P. R. Selvin, *Science* **303**, 676 (2004).